UNIVERSITY OF CALIFORNIA SAN DIEGO

**Nanoscale Studies of Strongly Correlated Electron Materials with Coherent X-Rays**

A dissertation submitted in partial satisfaction of the
requirements for the degree
Doctor of Philosophy

in

Physics

by

Nelson Hua

Committee in charge:

Professor Oleg G. Shpyrko, Chair
Professor Richard D. Averitt
Professor Eric E. Fullerton
Professor Jérémie Palacci
Professor Tenio Popmintchev

2020

The dissertation of Nelson Hua is approved, and it is acceptable in quality and form for publication on microfilm and electronically:

_____

_____

_____

_____

_____

Chair

University of California San Diego

2020

DEDICATION

To my parents and friends who have always supported my academic

endeavors.

EPIGRAPH

*Nobody ever figures out what life is all about, and it doesn't matter. Explore the world.*

*Nearly everything is really interesting if you go into it deeply enough.*

—Richard Feynman

TABLE OF CONTENTS

## LIST OF FIGURES

# ACKNOWLEDGEMENTS

Chapter 6, in full, is unpublished material of Nanoscale Resolution of Strain Fields in Highly Spin Polarized LSMO Nanoislands, Nelson Hua, Rajesh Chopdekar, Anatoly Shabalin, Stjepan Hrkac, Devin Cela, Martin V. Holt, Yayoi Takamura, Oleg G. Shpyrko. The dissertation author was the primary investigator of this work. Use of the Center for Nanoscale Materials and Advanced Photon Source, both Office of Science user facilities, was supported by the U.S. Department of Energy, Office of Science, Office of Basic Energy Sciences, under Contract No. DE-AC02-06CH11357.

Chapter 7, in full, is a publication of the material Extracting Contrast in an X-Ray Speckle Visibility Spectroscopy Experiment under Imperfect Conditions for the Journal of Synchrotron Radiation, Nelson Hua, Ivan A. Zaluzhnyy, Stjepan B. Hrkac, Anatoly G. Shabalin, and Oleg G. Shpyrko. The dissertation author was the primary investigator and the author of this paper.

## VITA

| 2013 | B.S. in Engineering Physics *summa cum laude*, University of Pittsburgh |
|------|------|
| 2013 | B.A. in Physics and Astronomy *summa cum laude*, University of Pittsburgh |
| 2017 | M.S. in Physics, University of California San Diego |
| 2020 | Ph.D. in Physics, University of California San Diego |

## PUBLICATIONS

**N. Hua**, S.S.K. Patel, R. Medapalli, A.G. Shabalin, S.B. Hrkac, J. Wingert, D. Cela, J. Ruby, J. Glownia, D. Zhu, M. Chollet, A. Singer, E.E. Fullerton, O.G. Shpyrko. "Measuring Electron-Phonon Coupling Timescales in Chromium by Photoexcitation." (*In Preparation*)

**N. Hua**, S. Matzen, T. Maroutian, G. Agnus, A.G. Shabalin, S.B. Hrkac, D. Cela, I.A. Zaluzhnyy, R. Chopdekar, M. Holt, P. Lecoeur, D. Ravelosona, O.G. Shpyrko. "Electrically-Tuned Strain Propagation in a Ferroelectric/Ferromagnetic (PZT/LSMO) Heterostructure." (*In Preparation*)

**N. Hua**, I.A. Zaluzhnyy, S.B. Hrkac, A.G. Shabalin, O.G. Shpyrko. "Extracting Contrast in an X-ray Speckle Visibility Spectroscopy Experiment Under Imperfect Conditions" *Journal Of Synchrotron Radiation* 27, (2020)

**N. Hua**, J. Li, S.B. Hrkac, A. Barbour, W. Hu, C. Mazzoli, S. Wilkins, R. Kukreja, E.E. Fullerton, O.G. Shpyrko. "Resolving Orbital Fluctuations in Magnetite using Resonant X-Ray Photon Correlation Spectroscopy." (*Under review for Phys. Rev. Lett. September 2020*)

A.G. Shabalin, J. del Valle, **N. Hua**, M. Cherukara, M.V. Holt, I.K. Schuller, O.G. Shpyrko. "Nanoscale imaging and control of volatile and non-volatile states in $VO_2$" *Small* 2005439, (2020)

A.G. Shabalin, E. Anouchi, **N. Hua**, Y.A. Wu, M.V. Holt, A. Sharoni, O.G. Shpyrko. "Twinned nanostructure of $VO_2$ thin films grown on r-cut sapphire" *Physical Review B* 102, 134106 (2020)

D. Zusin, E. Iacocca, L. Le Guyader, A.H. Reid, W.F. Schlotter, T-M. Liu, D.J. Higley, G. Coslovich, S.F. Wandel, P.M. Tengdin, S.K.K. Patel, A.G. Shabalin, **N. Hua**, S.B. Hrkac, H.T. Nembach, J.M. Shaw, S.A. Montoya, A. Blonsky, C. Gentry, M.A. Hoefer, M.M. Murnane, H.C. Kapteyn, E.E. Fullerton, O.G. Shpyrko, H.A. Durr, T.J. Silva. "Ultrafast domain rearrangement induced by optical pumping in ferromagnetic CoFe/Ni multilayers" (*Under review for Nature Communications July 2020*)

O.Yu. Gorobtsov, L. Ponet, S.K.K. Patel, **N. Hua**, A.G. Shabalin, S.B. Hrkac, J. Wingert, D. Cela, J.M. Glownia, D. Zhu, R. Medapalli, M. Chollet, E.E. Fullerton, S. Artyukhin, O.G. Shpyrko, A. Singer. "Ultrafast control of a vibrational state near the spin density wave critical point" (*Under review for Nature Communications October 2020*)

A.G. Shabalin, J. del Valle, A. Charnukha, **N. Hua**, M.V. Holt, D. Basov, I.K. Schuller, O.G. Shpyrko. "Nanoimaging of electrical failure in $VO_2$ resistive switching nanodevices" *ACS Applied Electronic Materials* 2, (2020)

H.T. Zhang, T.J. Park, I.A. Zaluzhnyy, Q. Wang, S.N. Wadekar, S. Manna, R. Andrawis, P.O. Sprau, Y. Sun, Z. Zhang, C. Huang, H. Zhou, Z. Zhang, B. Narayanan, G. Srinivasan, **N. Hua**, E. Nazaretski, X. Huang, H. Yan, M. Ge, Y.S. Chu, M.J. Cherukara, M.V. Holt, M. Krishnamurthy, O.G. Shpyrko, S. Sankaranarayanan, A. Frano, K. Roy, S. Ramanathan. "Perovskite neural trees" *Nature Communications* 11, (May 2020)

R. Kukreja, **N. Hua**, J. Ruby, A. Barbour, W. Hu, C. Mazzoli, S. Wilkins, E.F. Fullerton, and O.G. Shpyrko. "Orbital Domain Dynamics in Magnetite below the Verwey Transition." *Phys. Rev. Lett.* 121, 177601, (2018)

A. Singer, M. Zhang, S. Hy, D. Cela, C. Fang, T.A. Wynn, B. Qiu, Y. Xia, Z. Liu, A. Ulvestad, **N. Hua**, J. Wingert, H. Liu, M. Sprung, A.Z. Zozulya, E. Maxey, R. Harder, Y.S. Meng, and O.G. Shpyrko. "Nucleation of dislocations and their dynamics in layered oxide cathode materials during battery charging." *Nature Energy* 3, (2018)

A. Singer, J.G. Ramirez, I. Valmianski, D. Cela, **N. Hua**, R. Kukreja, J. Wingert, O. Kovalchuk, J.M. Glownia, M. Sikorski, M. Chollet, M.Holt, I.K. Schuller, and O.G. Shpyrko. "Nonequilibrium phase precursors during a photoexcited insulator-to-metal transition in $V_2O_3$." *Phys. Rev. Lett.* 120, 207601, (2018)

ABSTRACT OF THE DISSERTATION

**Nanoscale Studies of Strongly Correlated Electron Materials with Coherent X-Rays**

by

Nelson Hua

Doctor of Philosophy in Physics

University of California San Diego, 2020

Professor Oleg G. Shpyrko, Chair

Emergent behaviors arising from strongly correlated electron materials continue to puzzle physicists as there are still no clear explanations behind the underpinning mechanisms. The key hides in the collective behavior originating from the interactions among the electronic degrees of freedom, and the objective is to use various experimental probes to investigate the spin, charge, orbital and lattice contributions and their correlated behavior. This dissertation presents a study into how several advanced coherent x-ray techniques can be used to investigate the nanoscale landscape, both spatially and temporally, of strongly correlated electron materials to understand both the underlying physics and

how to incorporate these materials into technological devices. In particular, resonant elastic x-ray scattering and x-ray photon correlation spectroscopy are used to study the charge and orbital order tied to the metal-insulator transition in magnetite ($Fe_3O_4$), first observed by Verwey back in 1939. The results presented in Chapter 3 suggest that trimeron fluctuations due to thermal electron hopping among Fe 3d orbital sites play a vital role in the metal-insulator transition. Chapter 4 is an investigation into electron-phonon coupling times in elemental chromium using ultrafast x-ray pump-probe. Chapters 5 and 6 focus on the use of x-ray nanodiffraction to spatially resolve the strain in square LSMO nanoislands and the electrical-induced strain propagation in a ferroelectric/ferromagnetic (PZT/LSMO) heterostructure. Understanding the spatial extent of the correlation between strain to both the electric polarization and magnetic domains in these materials is essential for designs in sensory and computing architectures. Finally, Chapter 7 presents a simulation of a double probe x-ray speckle visibility spectroscopy experiment, a technique that relies on the change of contrast on an area detector to resolve dynamic timescales in the femto- to nanosecond range. Based on the simulated results, an analysis method that relies on selective binning of the detector image pixels is proposed to overcome the obstacles presented by experimental imperfections such as an angular misalignment between the two probes.

# Chapter 1

# Introduction

Emergent phenomena in strongly correlated electron materials such as superconductivity and colossal magnetoresistance has dominated condensed matter research in the past few decades. Their prevalence in research is not surprising considering the potential for a vast range of technological applications, including ultrafast switching in computing architectures and low power dissipations in energy storage devices [1, 2]. From a physics point of view, strongly correlated electron materials are ideally suited to investigate fundamental quantum effects and collective behavior arising from competing electronic and structural ground states. In the regime where strong correlations are at play, the physics governing the individual constituents can no longer accurately capture the collective behavior by way of a reductionist theory. Instead, a focus on the correlations is essential, and the physics community has responded by developing an expansive repertoire of techniques ranging from electron microscopy to terahertz probes. In this dissertation, the focus will be on the use of x-ray techniques, specifically coherent x-rays, as a probe into strongly correlated electron materials. The advantage of x-rays resides in its range of wavelengths on the order of interatomic distances in condensed matter systems that allows us to directly study the atomic structure. Since their discovery in 1895 by Röntgen, x-rays have revolutionized the

scientific field from determining the crystal structure of salt, and subsequently launching the field of crystallography, to resolving the helical structure of DNA [3, 4, 5]. In recent years, the x-rays produced by fourth generation synchrotrons and newly built x-ray free electron lasers have a remarkably high degree of coherent flux. The coherence properties, along with the ability to tune x-rays in both energy and polarization, makes it possible to further study the spin, orbital, and charge degrees of freedom coming from the electronic structure.

## 1.1 Strongly Correlated Electron Materials

Resolving the mesoscale link between the nanoscopic electron correlations in material systems to the macroscopic emergent behaviors is an active area of research with potentially far-reaching technological impacts [2, 6, 7]. For example, unconventional superconductivity where the electron pairing mechanism does not adhere to the standard Bardeen-Cooper-Schrieffer (BCS) theory has led to a variety of materials exhibiting higher superconducting temperatures [8, 9, 10]. The holy grail of understanding the mechanisms of electron interactions can lead to room temperature superconductivity, eliminating problems with power dissipation and consequently, overheating in various technological devices. Among the complex oxides, the nature of metal-insulator transitions are heavily studied to employ these materials in a neuromorphic computing architecture to mimic neuron and synapse behaviors [11]. In general, slight variations to parameters such as doping, strain, and temperature to name a few, can drastically alter both the nanoscale and macroscopic properties of these materials.

So the key from a physics point of view is to probe the electronic properties, both spatially and temporally, of the spin, charge, and orbital contributions in order to understand how they induce the emergent behaviors we see. Once we understand this, we

can optimize certain macroscopic properties or functionalities by tuning composition, size, or strain leading to potentially multifunctioning materials. For example, this has led to the field of spintronics where there is potential to exploit the electron spin as a means for both storing information and controlling fast switching for memory and computing devices [12, 13]. However, the electronic orders are often interwined in a way that is diffcult to unravel; in most cases, several complementary techniques must be employed to reconstruct the electronic configuration. Fig. 1.1 shows an example of a manganite exhibiting simultaneous spin, charge, and orbital order with each having a different unit cell revealed by several x-ray and neutron scattering techniques. The cooperative and competing phases in manganites have been suspected to induce the colossal magnetoresistance (CMR) phenomenon where slight changes in the magnetic field can cause the electrical resistance of the material to change by several orders of magnitude [6].
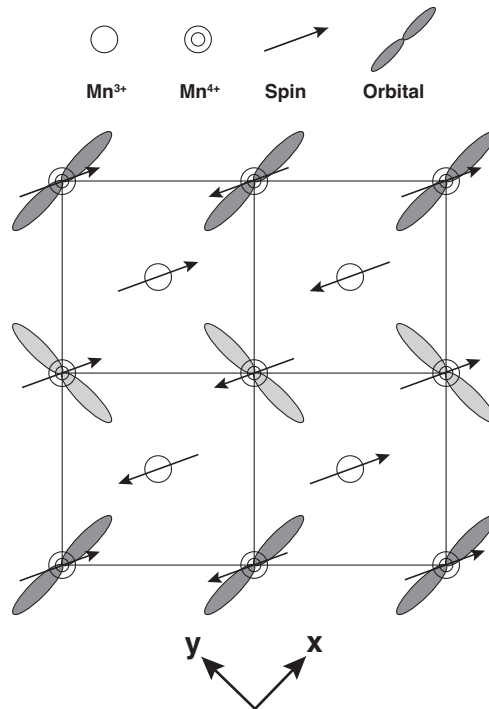


**Figure 1.1**: Simultaneous existence of charge, spin, and orbital orders in the $MnO_2$ planes of $La_{0.5}Sr_{1.5}MnO_4$ with each having a different unit cell. *This figure was adapted from [14].*

3
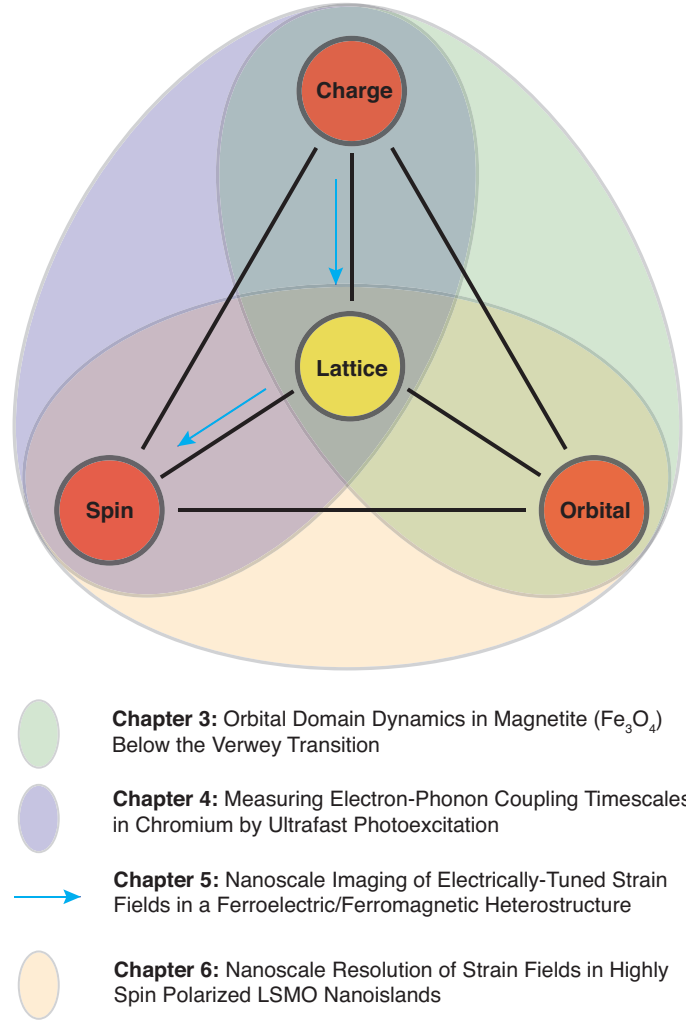
**Figure 1.2**: The spin, charge, and orbital electronic degrees of freedom along with the lattice structure are highly correlated in material systems of interest in this dissertation. This schematic highlights the focus of each topic in this dissertation in terms of the relevant correlations and degrees of freedom at play.

## 1.2   Interaction of X-Rays with Matter

The theory behind the interaction of an electromagnetic wave with matter encompasses volumes of standard textbooks in electromagnetism and quantum theory, most of which is outside the scope of topics in this dissertation. Here the range of electromagnetic radiation is constrained to the x-ray regime where the energy of an x-ray is related to the wavelength by $\lambda[\mathring{A}] = \dfrac{hc}{E} = \dfrac{12.398}{E[keV]}$. The typical wavelengths of soft (usually between

500 eV to 2 keV) and hard (2 -100 keV) x-rays are on the order of Angstroms, and follow-ing Rayleigh's criterion that the minimum resolution needed to distinguish two objects is determined by the wavelength of the electromagnetic wave, x-rays are ideal probes for investigating solid state systems where the typical atomic spacing is on the order of Angstroms. Broadly speaking, x-ray probes into material systems can be divided into elastic and inelastic techniques. In elastic probes, the energy ($\hbar\omega$) and magnitude of momentum ($\hbar|\mathbf{k}|$) is conserved and can be described based on classical electromagnetic theory where the photon interacts with the electric field of the system of interest. In inelastic techniques, significant absorption processes affect the scattering process where the energy and outgoing wave vector of the scattered signal is no longer conserved. In this case, we have to resort to quantum mechanics to accurately capture the physical processes. The techniques applied in this dissertation are all elastic, and therefore the following will summarize the theory behind elastic scattering [15, 16].

When an x-ray scatters off an electron, the oscillating electric field of the x-ray interacts with the charge of the electron, forcing the electron to oscillate about its mean position. Whenever a charged particle is accelerating, electromagnetic radiation is emitted, and this is the scattered x-ray signal that has the same energy and magnitude of momentum as the incident x-ray signal. We can define the incident and exit signals as wavevectors, $\mathbf{k_{in}}$ and $\mathbf{k_{out}}$, with units of inverse Angstroms corresponding to the frequency of the x-ray radiation. This elastic scattering process off the electron charge is known as Thomson scattering in which the differential cross section from scattering off a single electron is given in Eq. 1.1 where $r_o = \dfrac{e}{m_o c^2} = 2.82$ fm is the classical electron radius and $P(\theta)$ describes the polarization dependence of the incident radiation field. The total cross section for Thomson scattering is calculated by integrating over the solid angle, $\Omega$, which turns out to be $\dfrac{8\pi r_o^2}{3}$. In both cases, the classical cross section for scattering is independent of the photon energy.

$$\frac{d\sigma}{d\Omega} = r_o^2 \cdot P(\theta) \tag{1.1}$$

For the case of an atom with Z electrons, the electron density is specified by $\rho(\mathbf{r})$ where the spatial coordinates of each electron relative to the origin is given by the vector $\mathbf{r}$. $\mathbf{Q}$ is the momentum transfer (also known as the scattering vector) defined in Eq. 1.2 and its geometric relation is shown schematically in Fig. 1.3.

$$\mathbf{Q} = \mathbf{k_{out}} - \mathbf{k_{in}} \tag{1.2}$$

Since there are multiple electrons the x-rays can scatter off of, there are constructive and destructive interference effects depending on the relative phases of the scattered intensity. For example, we can consider the total scattering from two incident waves traveling in the same direction, one scattering at the origin and one scattering off the electron density located $\mathbf{r}$ away, as depicted in Fig. 1.3. The relative phase difference of the entire scattering process is simply the ratio of the path length difference of the two trajectories to one wavelength of the x-ray, which turns out to be $\mathbf{k_{out}} \cdot \mathbf{r} - \mathbf{k_{in}} \cdot \mathbf{r}$. This conveniently reduces to $\mathbf{Q} \cdot \mathbf{r}$, and since $|\mathbf{k}| = \dfrac{2\pi}{\lambda}$, the magntiude of the scattering vector in terms of the wavelength and incident angle can also be written as $|\mathbf{Q}(\lambda, \theta)| = 2|\mathbf{k}|sin(\theta) = \dfrac{4\pi sin(\theta)}{\lambda}$.

The total scattering cross section or scattering length in this case is just a superposition of the Z electrons described by Eq. 1.3 where $f^o(\mathbf{Q})$ is known as the atomic form factor. In the limit of $\mathbf{Q} \to 0$, the atomic form factor reduces to $f^o(\mathbf{Q}) = $ Z where there is complete constructive intereference. However, as $\mathbf{Q}$ changes as a function of $\lambda$ and $\theta$, the electron density at each point defined by $-r_o\rho(\mathbf{r})d\mathbf{r}$ will make a different contribution to the total scattering intensity based on its phase of $e^{i\mathbf{Q}\cdot\mathbf{r}}$. Recognizing that the right side of Eq. 1.3 is just a Fourier transform, we can thinking of the scattered intensity in the far-field as simply a Fourier transform of the distribution of electron density.

$$-r_o f^o(\mathbf{Q}) = -r_o \int \rho(\mathbf{r}) e^{i\mathbf{Q}\cdot\mathbf{r}} d\mathbf{r} \qquad (1.3)$$
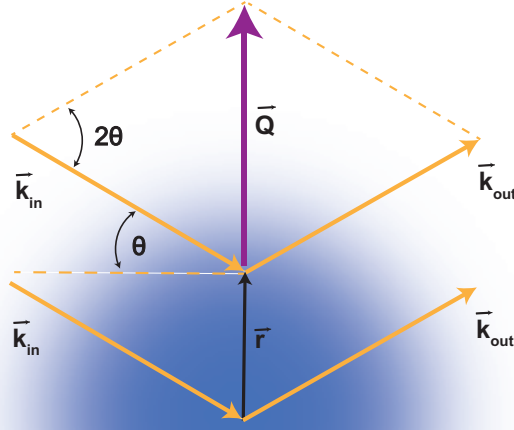


**Figure 1.3**: The elastic scattering process of an x-ray signal off the electron density determined by the number of electrons, Z, surrounding an atom.

Extending the scattering process to a unit cell of a crystal structure consisting of multiple atoms, the scattering is just a sum of the atomic form factors of each atom located at $\mathbf{r_n}$ from the origin given by Eq. 1.4. Finally, extrapolating to a periodic lattice defined by a unit cell and translational symmetry as seen in Fig. 1.4, the equivalent scattering length is given in Eq. 1.5. The contributions from the scattering centers, either atoms defined by the atomic form factor $f_n$ or a unit cell defined by $F_{unit}$, are located $\mathbf{R_n}$ from the origin where $\mathbf{R_n} = n_1\mathbf{x}_1 + n_2\mathbf{x}_2 + n_3\mathbf{x}_3$: $n_i$ are integers while $\mathbf{x}_i$ are the basis vectors describing the translational symmetry of the crystal structure. In this case, the scattering term, $F_{crystal}$, is known as the structure factor and it is a critical parameter used to determine the scattering process in crystal diffraction. The total scattered intensity in the case of an atom

with Z electrons and a periodic lattice is proportional to $|f_n|^2$ and $|F|^2_{crystal}$, respectively.
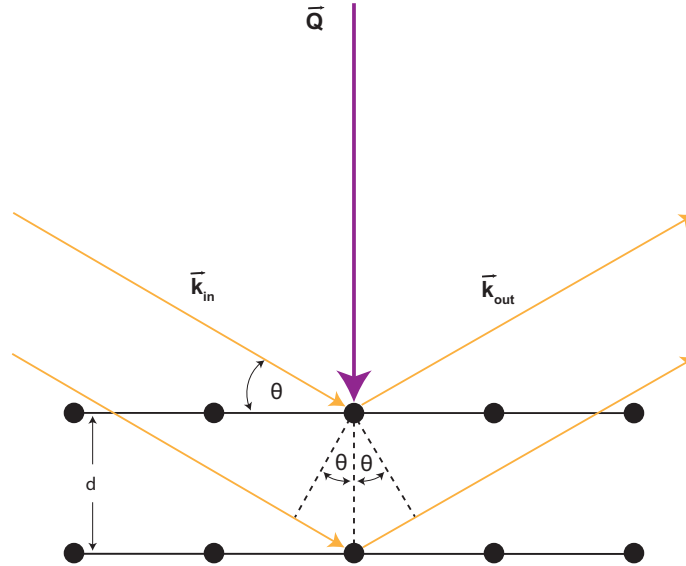


**Figure 1.4**: The elastic scattering process of an x-ray signal off a periodic lattice where each point can be considered an atom or a unit cell.

$$F_{unit}(\mathbf{Q}) = \sum_n f_n(\mathbf{Q})e^{i\mathbf{Q}\cdot\mathbf{r_n}} \tag{1.4}$$

$$F_{crystal}(\mathbf{Q}) = F_{unit}(\mathbf{Q})\sum_i e^{i\mathbf{Q}\cdot\mathbf{R_n}} \tag{1.5}$$

The condition for crystal diffraction where an intense scattering peak is seen in the far-field from the interaction of x-rays with the material structure is given by Eq. 1.6, also known as Bragg's law. Here we can consider x-rays scattering off of lattice planes separated by a distance, d, as shown in Fig. 1.4 where d is unknown. Given the wavelength of the x-rays and the scattering angle, we can determine the difference in path lengths between successive lattice planes. This path length difference calculated from simple trigonometry is $2d\sin(\theta)$, and setting this equal to $n\lambda$ where $n$ is an integer, we establish the condition where the scattered x-rays are all in phase, resulting in complete constructive interference. The crystal structure of materials are characterized by varying the incident angle at a

known x-ray energy. Intense scattering peaks on a detector, known as Bragg peaks, will show up at various angles that contains information about the lattice spacing.

$$n\lambda = 2d\sin(\theta) \tag{1.6}$$

Since the far field diffraction pattern is just a Fourier transform of the electron density, we can also establish the conditions for crystal diffraction in Fourier space (also known as reciprocal space). Given $\mathbf{R_n}$ that describes the real space translational symmetry of the lattice, we can introduce a recipocal lattice where the reciprocal basis vectors, $\mathbf{x}_i^*$, are given by Eq. 1.7. The $ijk$ notation follows a cyclic permutation.

$$\mathbf{x}_i^* = 2\pi \frac{\mathbf{x}_j \times \mathbf{x}_k}{\mathbf{x}_i \cdot (\mathbf{x}_j \times \mathbf{x}_k)} \tag{1.7}$$

The distance in reciprocal space is then described by $\mathbf{G} = h\mathbf{x}_1^* + k\mathbf{x}_2^* + l\mathbf{x}_3^*$ where $h, k, l$ are integers analogous to $n_i$ to describe the translational symmetry in reciprocal space. In terms of $\mathbf{G}$, the diffraction condition is met when $\mathbf{Q} = \mathbf{G}$.

## 1.3   Incoherent vs. Coherent X-Rays

Analogous to how the visible light from the Sun is considered an incoherent source whereas a laser pointer produces coherent radiation, x-rays can also be produced as coherent or incoherent signals. The electromagnetic radiation from the Sun is considered incoherent because the radiation is propagating in all directions and span a range of wavelengths. In other words, there are various degrees of constructive and destructive interference effects. With a laser pointer, all photons are confined to a specific wavelength, hence why they are monochromatic, and the waves propagate in one direction. This type of radiation results in complete constructive interference and are thus *coherent.*

The original production of x-rays in the early twentieth century was incoherent. The earlier gas and filament tubes contained three key elements to generate x-rays: (i) a source of electrons, (ii) high voltages, and (iii) a metal target [16]. A filament tube consisted of an anode and cathode where a high voltage is applied to accelerate the electrons from the cathode to the anode target, usually a water-cooled metal. Since the acceleration of a charged particle emits electromagnetic radiation, the rapid deceleration of the electron when it hits the metal target produces electromagnetic radiation, known as *Bremsstrahlung* radiation (German for 'braking radiation'). The voltages used to generate those electrons were high enough to produce radiation in the x-ray regime, though at the time this radiation was unknown and therefore why $x$ was assigned. However, since the electrons spanned a range of energies, the x-rays produced also resulted in a range of energies propagating in all directions. This incoherent radiation is sufficient to determine the average structure of materials or completely homogenous materials. However, most materials contain inhomogeneities, meaning local disorder such as grain boundaries, dislocations, and defects. In order to resolve the nanoscale inhomogeneities, coherent x-rays are needed. With both incoherent and coherent x-ray probes, the recorded intensity is proportional to $|F|^2$ where the phase information dependent on both the electron density and phase of the x-ray probe is lost. In the case of coherent x-rays, the phase of the probe is known, resolving one of the unknown variables. This leads to diffraction patterns with resolvable features that are a direct manifestation of local inhomogenities, and some techniques like coherent diffractive imaging (CDI) and x-ray photon correlation spectroscopy (XPCS) make it possible to extract local structural and electronic information that would otherwise be averaged out with an incoherent probe.

The availability of coherent x-rays with sufficient flux to investigate nanomaterials are currently only available at synchrotron and x-ray free electron (XFEL) sources, but the degree of coherence can vary. We quantify the degree of coherence in terms of the

coherent volume: the axis along the direction of propagation is defined as the temporal coherence length, set by the wavelength, whereas the other two axes orthogonal to the propagation direction are referred to as the spatial coherence length, set by the divergence of the propagating direction. Specifically, the temporal (or longitudinal) coherence length, $\xi_T$, is determined by the distance two waves become completely out of phase as depicted in Fig. 1.5(a). Setting $N\lambda = (N + \frac{1}{2})\lambda^*$ where $\Delta\lambda = \lambda - \lambda^*$ results in $N = \frac{\lambda - \Delta\lambda}{\Delta\lambda} \approx \frac{\lambda}{\Delta\lambda}$. Substituting N in terms of the wavelength leads to a temporal correlation length defined in Eq. 1.8. The spatial (or transverse) coherence length can be calculated by assuming the wavelength of two waves are the same, but the propagating directions are slightly different. As shown in Fig. 1.5(b), if two wave fronts start out from two sources separated by a distance $d$, after traveling a distance $R$, the two waves will be out of phase. Since the angle of the two triangles are the same, the proportionality of the two sides should be the same: $\frac{d}{R} = \frac{(\lambda/2)}{\xi_T}$. This leads to the spatial coherence length defined by Eq. 1.9 that is valid for a spherically symmetric x-ray probe (in a real experiment, the two spatial directions orthogonal to the propagating direction can have different correlation lengths depending on how the x-ray beam is focused).

$$\xi_L = \frac{1}{2}\frac{\lambda^2}{\Delta\lambda} \tag{1.8}$$

$$\xi_T = \frac{\lambda}{2}\left(\frac{R}{d}\right) \tag{1.9}$$

Finally, if we refer back to the differential cross section of scattering in Eq. 1.1, the polarization factor is different for coherent and incoherent radiation. For incoherent radiation, the electric field vectors of the x-rays are randomly distributed about the radial direction, averaging to $\frac{1}{2}\left[1 + \cos^2(\theta)\right]$. On the other hand, if the x-rays are fully coherent, the electric field vectors are the same and can be aligned so that x-rays impinge on the

11
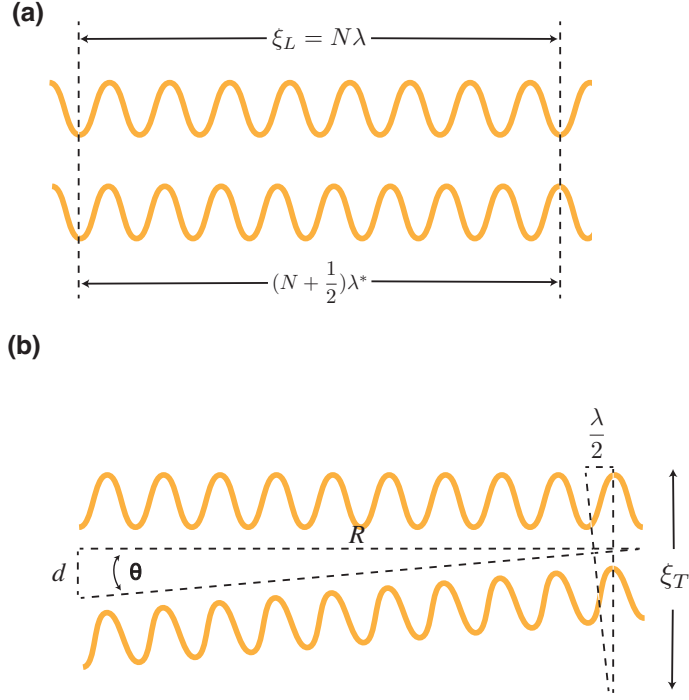
**Figure 1.5**: **(a)** The temporal coherence length, $\xi_L$, is defined as the distance where two waves with different wavelengths become completely out of phase. **(b)** The spatial correlation length, $\xi_T$, is defined as the distance for two waves with the same wavelength but slightly different propagating directions to become out of phase.

material with the electric field vector aligned to either the vertical or horizontal scattering plane. The resultant polarization factors for these three cases are given in Eq. 1.10.

$$
P(\theta) = \begin{cases} 1 & \text{Linear polarized (vertical scattering plane)} \\ \cos^2(\theta) & \text{Linear polarized (horizontal scattering plane)} \\ \frac{1}{2}\left[1+\cos^2(\theta)\right] & \text{Unpolarized} \end{cases} \tag{1.10}
$$

12

# Chapter 2

# Coherent X-Rays

## 2.1   Overview of Synchrotrons and Free Electron Lasers

As we discover more quantum materials where effects are confined to spatial extents smaller than ~40 nm, such as strain-controlled magnetic domain wall motion in CoFeB films [17], and important electron dynamics are on the sub-picosecond timescales, standard x-ray tube sources that can be found in university labs no longer provide sufficient intensity to generate the necessary scattered intensity. Furthermore, if we want to probe the electronic structure of materials where a high energy resolution is required, we will need an intense coherent probe. These studies can be carried out at large-scale facilities such as third-generation synchrotrons, x-ray free electron lasers, and most recently, diffraction limited storage rings (DSLR) that have a high degree of brilliance, a parameter that is used to quantify the quality of the x-rays produced by these sources. The brilliance is mathematically given by Eq. 2.1 where the features that we want to maximize, mainly the intensity in photons per second, is in the numerator, and the features that we want to minimize are given in the denominator. Ideally, we want a highly collimated beam and a small source size in order to focus the x-ray probe to a small spot size with spatial

coherence. The collimation, in both the horizontal and vertical directions, is typically reported in milliradians whereas the source size is given as mm². Finally, the relative energy bandwidth is fixed at 0.1% that takes into account the degree of temporal coherence. Fig. 2.1 shows how the brilliance of various synchrotron and XFEL sources have increased over the past few decades with a rate that exceeds Moore's law for computational power.

$$\text{Brilliance} = \frac{\text{Photons/second}}{(\text{mrad})^2(\text{mm}^2 \text{ source area})(0.1\% \text{ BW})} \tag{2.1}$$
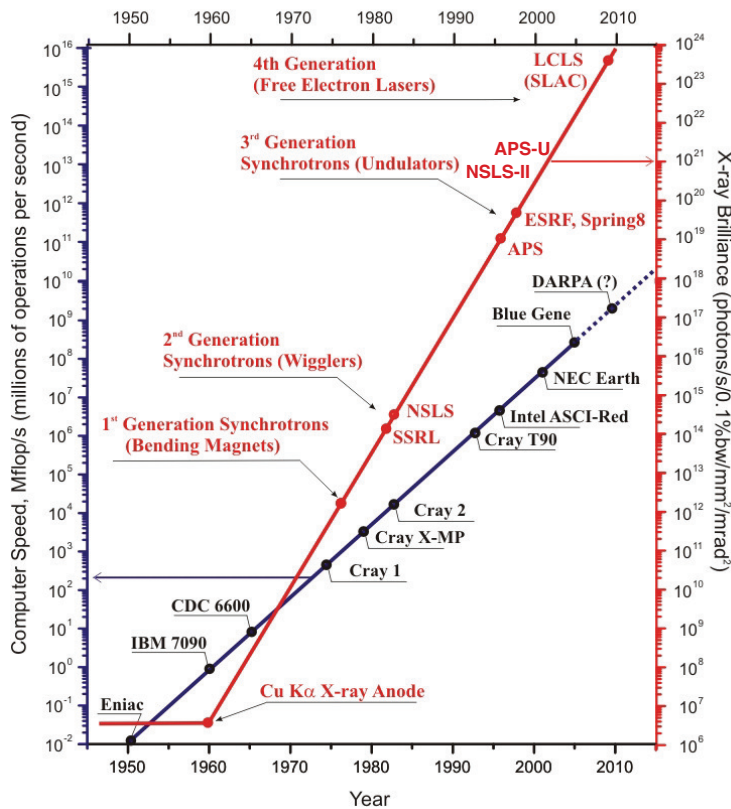


**Figure 2.1**: The increase in brilliance of various synchrotron and x-ray free electron laser sources follows a rate that is higher than Moore's law for computational power in the past few decades. *This figure was adapted from Oleg Shpyrko.*

The overarching principle of these sources is based on the acceleration of light charged particles, either electrons or positions, at relativistic speeds that consequently emit

electromagnetic radiation in the x-ray regime. A simplified schematic of a synchrotron and its main components are shown in Fig. 2.2. An electron gun, usually a cathode tube with RF cavities, produce the electron bunches that are accelerated to GeV energies by the booster synchrotron. The electrons are subsequently injected into the storage ring where a series of bending magnets keep the electrons in a circular orbit via the Lorentz force. Given an orbiting relativistic electron in a synchrotron with radius $\rho$, the condition $\gamma mc = \rho e B$ is met where B is the magnitude of the magnetic field produced by the bending magnets and $\gamma$ is the Lorentz factor. Therefore, the radius of the electron orbit is given as

$$\rho[m] = 3.3 \frac{\mathcal{E}_e[GeV]}{B[T]},$$

(2.2)

where the energy of the electron is on the order of GeV. RF cavities throughout the main storage ring maintain constant electron energies on the order of hours to a few days, which means the booster synchrotron is only needed for the initial injection. A series of straight segments in the main storage ring contain insertion devices, usually wigglers or undulators, to further focus the x-rays. For most third-generation synchrotrons, undulators consisting of alternating dipole magnets are used to drive the electrons along a sinusoidal path as seen at the top of Fig. 2.2. At each crest/trough where the acceleration is maximized, the electrons emit radiation along the direction of the undulator, producing an x-ray radiation cone with an opening angle of $\frac{1}{\sqrt{N}\gamma}$ where N is the number of periods the electron undergoes in the undulator. For reference, the opening angle of the radiation cone from the storage ring before entering the undulator has a natural opening angle of $1/\gamma$. So the undulator is able to further collimate the x-ray beam by a factor of $\sqrt{N}$. At the end of each of these straight sections is an experimental endstation (referred to as a beamline) that uses various optics and instruments to tailor the x-rays for specific techniques or fields of study such as materials systems or biological samples. Depending on the size of the synchrotron, the number of beamlines can range somewhere between 20-40.
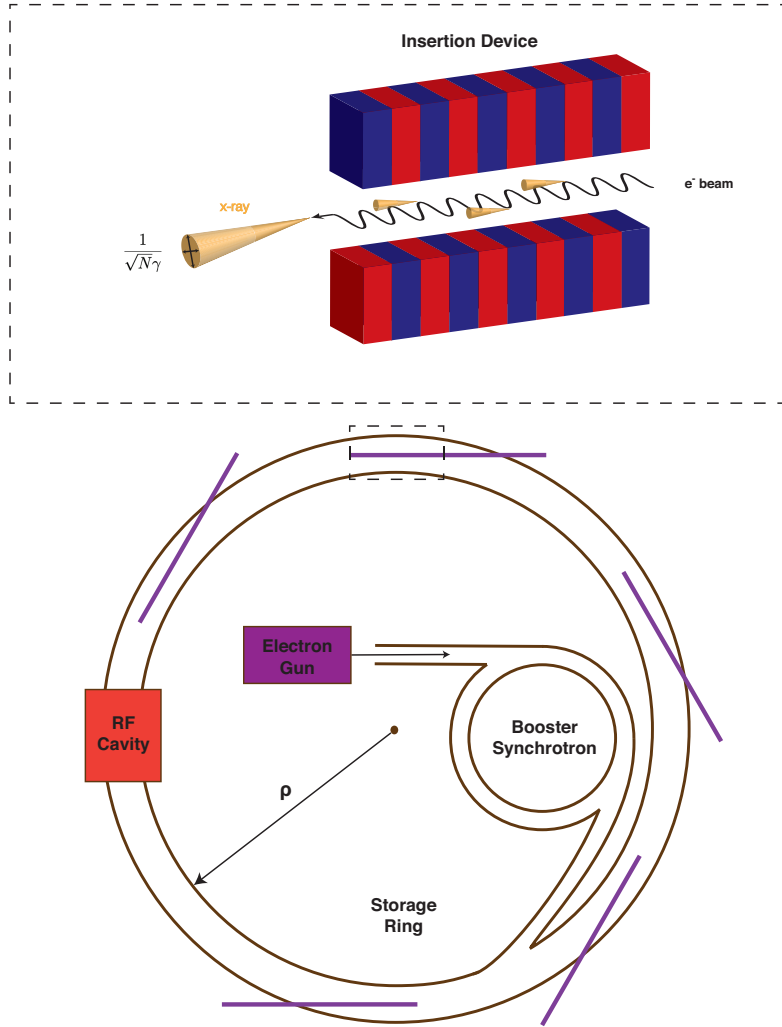
**Figure 2.2**: Simplified schematic of the main components of a synchrotron. An electron gun, usually a cathode tube with RF cavities, is the source of electron bunches that are accelerated to GeV energies in the booster synchrotron. RF cavities in the storage ring maintain the electron bunch energies and x-rays are emitted tangential to the circular orbit. A series of straight sections where insertion devices (usually wigglers or undulators) focus the x-rays to experimental endstations.

An XFEL, on the other hand, relies on a linear accelerator with similar working features as a synchrotron, but the main difference is a phenomenon known as self-amplified spontaneous emission (SASE). A low-emittance electron source produces bunches of electrons that are accelerated through a LINAC, a series of RF cavities with alternating electric fields. Once up to speed, a bunch compressor, which is typically a series of specifically

configured bending magnets known as a chicane, is used to further squeeze the bunch into a higher density along the axis of propagation. To put it simply, the chicane acts more strongly on the slower electrons at the back of the bunch more strongly than the ones at the front. This compressed electron bunch with a current in the kA range may go through another LINAC before entering an undulator that is typically several hundres of meters in length compared to an undulator that is normally a few meters at a synchrotron. This length is required for the electrons to enter a resonant condition that allows for SASE. As shown in Fig. 2.3, the electron bunch in the beginning of the undulator emits incoherent radiation, but as the bunch trasverses along the undulator, the electrons experience unequal electric and magnetic forces that create a modulated electron bunch consisting of microbunches of electrons that are all in phase. The microbunches have a width of a few femtoseconds and are separated by the wavelength of the emitted x-ray radiation. This allows the intensity of coherent flux to scale quadratically with the number of electrons in the bunch compared to a synchrotron where the intensity scales linearly with the number of electron emitters. Furthermore, the pulse duration of from an XFEL source is on the order of femtoseconds compared to the picosecond timescale typical of synchrotrons, opening up the potential to study sub-picosecond dynamics in material systems.

## 2.2 Techniques

### 2.2.1 X-Ray Photon Correlation Spectroscopy (XPCS)

X-ray Photon Correlation Spectroscopy (XPCS) is a powerful coherent x-ray technique capable of probing the temporal evolution in disordered and partially ordered systems. This is a technique that is extended from dynamic light scattering (DLS) [18], the analogous technique in the visible regime that can be carried out with a hand-held laser pointer. The scattered intensity in the far-field from a coherent light source off of random scatterers will

**X-ray Free Electron Laser (XFEL)**

**Undulator**

Incoherent bunch

Micro-bunches

**Self-Amplified Spontaneous Emission (SASE)**
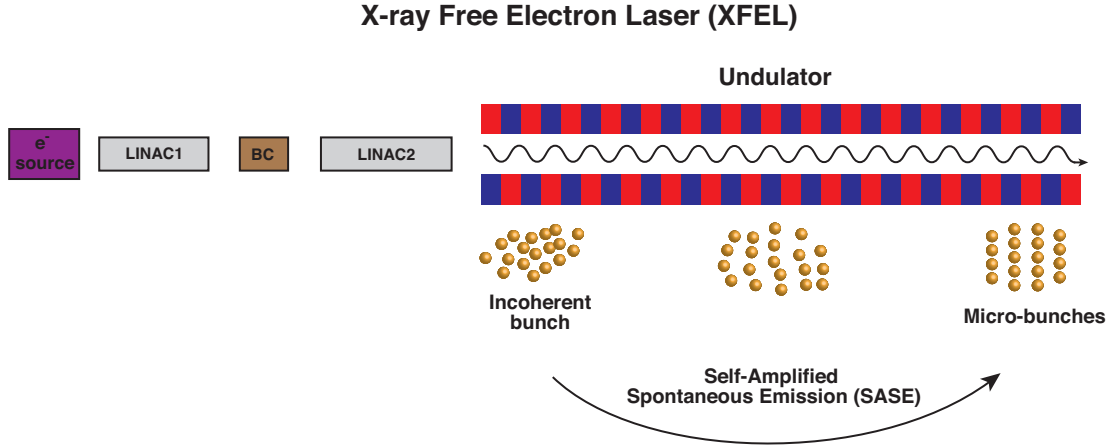
**Figure 2.3**: Schematic of an x-ray free electron laser. A low-emittance electron source generates electron bunches that are accelerated through a LINAC. A bunch compressor, typically composed of a series of bending magnets known as chicanes, spatially compresses the bunch into a higher density along the axis where a second accelerator introduces the electron bunches into an undulator that is on the order of hundreds of meters in length. The initial bunch undergoes SASE, resulting in modulated microbunches that emit highly coherent x-rays.

produce a 'speckle' pattern consisting of regions of bright and dim intensities. For the visible regime, dynamic light scattering can probe dynamics of particles on the micron lengthscales set by the wavelength of the laser. For example, shining a laser through a glass of water with dirt particles will produce a speckle pattern, and the motion of the dirt particles will manifest as a fluctuating speckle pattern. This is exactly how microparticles undergoing Brownian motion was measured [19]. In the x-ray regime where the lengthscales are on the order of nanometers, XPCS has the capability of coupling to the structural order parameter such as a Bragg peak to detect fluctuations of the lattice structure. For example, Fig. 2.4(a) shows a simulation of what a Bragg peak of a material with homogenous mosaicity looks like when probed with a coherent vs. incoherent source. A better visualization of the contrast can be seen if a line cut is through the central speckle pattern is taken as shown in Fig. 2.4(b). An additional advantage from the polarization and energy-tuning abilities of coherent x-ray sources is the ability to couple to the electronic structure where fluctuations of the charge, orbital, and spin order parameters are also possible.
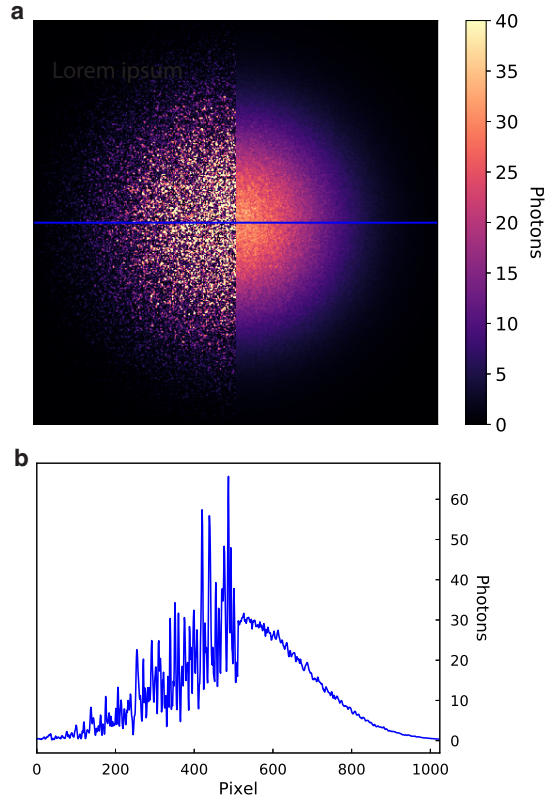
**Figure 2.4**: **(a)** A simulation of what a detector image of a Bragg peak may look like with a coherent (left side) and an incoherent (right side) probe. Any dynamics of the structural domains will cause the speckles to fluctuate with the coherent signal, but can not be resolved with the incoheret source. **(b)** A line cut through the central peak shows the degree of contrast between the coherent and incoherent sources.

Information about the dynamics of the order parameter can be extracted from performing intensity-intensity autocorrelations between successive 2D detector images separated by a characteristic time. Based on this method, the time resolution is limited by the detector readout time, which is typically on the millisecond timescale with the fastest detectors reading out on the microsecond timescale. Dynamics faster than the detector readout time can be resolved using a modified technique known as x-ray speckle visibility spectroscopy (XSVS) that is presented and discussed in Chapter 7 of this dissertation. All the information is encoded in the two-time autocorrelation function known as the two-time $g_2$ function that is mathematically defined in Eq. 2.3. The pixel-by-pixel intensity

correlation between every combination of the speckle pattern during the measurement is calculated and plotted as shown in Fig. 2.5(a,b). The $t_1=t_2$ line will always be fully correlated as that is the same speckle pattern correlated with itself, but lines orthogonal to the $t_1=t_2$ line show how the correlation decays with increasing time delays. Fig. 2.5(a) shows an example of equilibrium dynamics where the dynamics are homogenous throughout the measurement, but Fig. 2.5(b) is a characteristic pattern of non-equilibrium dynamics where there are sections of slow and fast dynamics. For non-equilibrium dynamics where the system can suddenly unbuckle or freeze, it is important to see at which points those occur and the frequency of these events that can be visually determined from the two-time autocorrelation plots.

$$g_2(\mathbf{Q}, t_1, t_2) = \frac{\langle I(\mathbf{Q}, t_1) I(\mathbf{Q}, t_2) \rangle}{\langle I(\mathbf{Q}, t_1) \rangle \langle I(\mathbf{Q}, t_2) \rangle} \tag{2.3}$$

If a system exhibits equilibrium dynamics, the one-time autocorrelation function can be used to quantify the type of dynamics and the characteristic decay time. In other words, if we average all the lines orthogonal to the $t_1=t_2$ in a two-time autocorrelation plot, we obtain the one-time $g_2$ function. The latter part of Eq. 2.4 shows that the correlation at a given delay time, t, is the average of the autocorrelation function between every possible combination of detector images that are separated by that delay time. For ergodic systems, this results in a decaying stretched exponential function that is related to the intermediate scattering function by $|F(\mathbf{q}, t)| = \exp\left(\frac{-t}{\tau}\right)^{\beta}$. $\tau$ is the characteristic decay time whereas $\beta$ is the stretched or compressed exponential function that describes the nature of the dynamics: $\beta > 1$ shows a system with jammed dynamics, $\beta < 1$ shows a system with glassy or liquid-like dynamics, and $\beta = 1$ reduces the equation to Brownian motion. Fig. 2.5(c) shows a system that exhibits two characteristic decay times that originates from two separate fast and slow dynamics of the spin-density wave (SDW) in chromium. Fig. 2.5(d) is an example of a system that shows a transition temperature between two types of

20

dynamics demonstrated by the change in $\beta$ as a function of temperature.

$$g_2(\mathbf{Q},t) = 1 + A|F(\mathbf{q},t)|^2 = \frac{\langle I(\mathbf{Q},\tau)I(\mathbf{Q},\tau+t)\rangle}{\langle I(\mathbf{Q},\tau)\rangle_\tau^2} \tag{2.4}$$
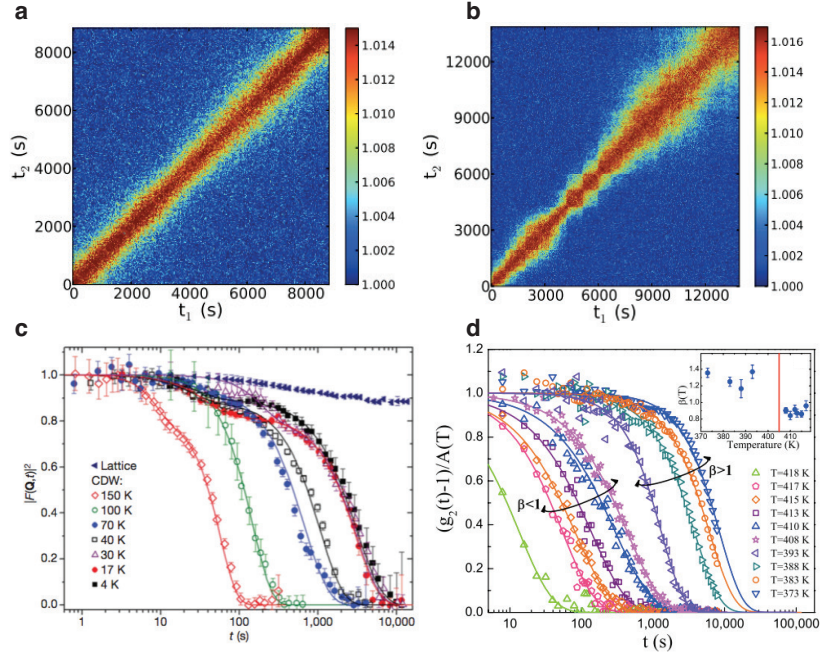


**Figure 2.5**: The dynamics of a system is fully encoded in the two-time autocorrelation function where examples of equilibrium **(a)** and non-equilibrium **(b)** dynamics are shown. [20]. **(c)** An example of a one-time autocorrelation function where the dynamics from spin-density fluctuations in Cr exhibit two characteristic timescales [21]. **(d)** An example of a system with a transition between glassy and jammed dynamics determined by a continuous transition in the $\beta$ value [22].

## 2.2.2    Resonant Elastic X-ray Scattering (REXS)

Resonant elastic x-ray scattering (REXS) is a unique coherent x-ray probe that combines the structural sensitivity of x-ray diffraction (XRD) with element specificity of x-ray absorption spectroscopy (XAS) into a single experiment [23]. The atomic form factor described by Eq. 1.3 is more accurately expressed as Eq. 2.5 in units of $r_o$.

$$f(\mathbf{Q}, \omega) = f^0(\mathbf{Q}) + f^{'}(\omega) + i f^{''}(\omega) \tag{2.5}$$

The first term is the atomic form factor due to the classical Thomson scattering while the $f^{'}(\omega) + i f^{''}(\omega)$ portion is known as the dispersion corrections that is a function of the photon energy and incoming polarization [23]. Typically, the last two terms can be ignored, but they become significant near absorption edges, also known as the resonant edges. This allows us to probe the spatial modulation of the lattice and the electronic order parameter at the valence bands. The mechanism behind the resonant scattering process is shown in Fig. 2.6 where a photon is absorbed by a core electron and consequently induces a virtual transition of the electron from the core level to an unoccupied state in the valence band. The electron subsequently falls back to the core level leading to an emission of a photon with the same energy.

This technique is particularly important in the soft x-ray regime where access to the transition-metal L-edges and the oxygen K-edge is possible to probe the charge, spin, and orbital orders. For example, intertwined orbital and spin density waves were recently seen in the unconventional superconductor, MnP, using REXS with the x-ray energy tuned to the Mn $L_2$ and $L_3$ edges [24]. In the hard x-ray regime, REXS can be used to probe the electronic structure of rare earth metals from virtual transitions from core levels to the 4f/5d valence band. For example, x-rays tuned to the Ho $L_3$ edge was used to reveal a spiral spin density wave of ferromagnetically aligned layers in elemental holmium [25]. In some materials, there are Bragg-forbidden reflections where distortions of the crystal structure lead to structure factors that sum to zero, i.e. no intensity can be seen at that Bragg condition. However, these 'forbidden' peaks can sometimes be seen at resonant energies, indicating the existence of some kind of electronic order depending on the energy and polarization states. In other words, the first term in Eq. 2.5 is zero, but the last two terms are large at a given $\omega$. An example of a Bragg-forbidden reflection that can be

probed with REXS due to a a charge-orbitally ordered state in magnetite is demonstrated in Chapter 3 of this dissertation.
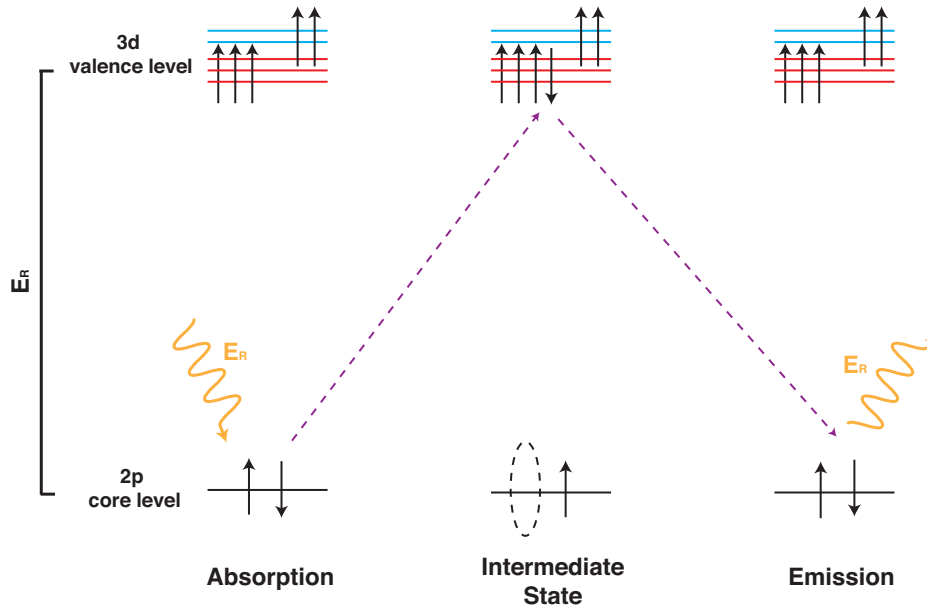


**Figure 2.6**: X-ray scattering where the energy is tuned to absorption edges leads to resonant elastic x-ray scattering where electronic valence states contribute to the signal. For example, when the energy is tuned to transition metal $L$ edges, the incoming photons are virutally excited from the core 2p orbitals to the 3d orbital states before reemitting. With the addition of polarization capabilites, this technique leads to enhanced diffraction signals coming from the electronic anisotropies associated with charge, orbital and spin orders.

### 2.2.3 Nanodiffraction

Standard x-ray diffraction setups that can be found in university labs, such as a Bruker or Rigaku system, relies on copper targets to produce Cu K$\alpha$ radiation (approximately 8 keV) to characterize the structure of materials. The position and intensity of diffraction peaks reveal the *average* material properties, but can not resolve spatial heterogeneities that is inherent in many materials and functional devices. For example, a voltage-induced metal-insulator transition in VO$_2$ can create local grains and filaments of metallic domains in a sea of insulating domains [27] that has potential to serve as the
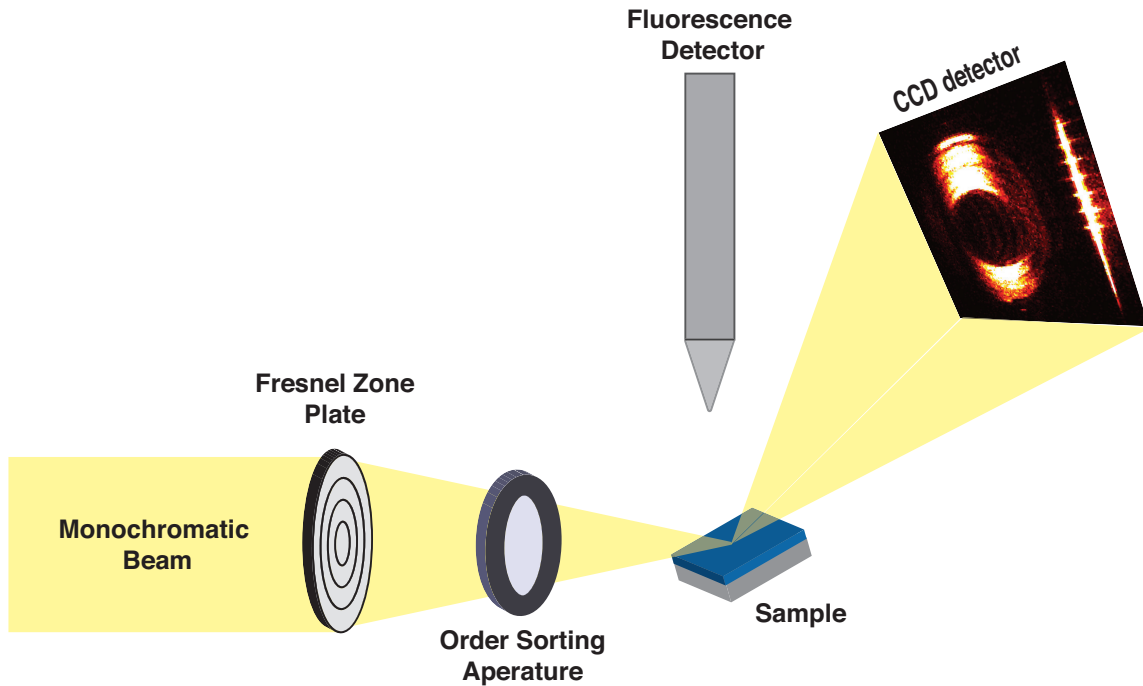
**Figure 2.7**: A schematic of a standard hard x-ray nanoprobe setup that uses diffractive optics to focus the beam. The Fresnel zone plate (FZP) focuses the beam that is filtered with an order sorting aperature (OSA) before impinging the sample. With a 2D area detector and slight divergence of known incoming wavevectors, it is possible to resolve the local strain and rotation based on the diffraction pattern overlaid on the imprint of the FZP. A simulatneous fluorescence detector can be used to follow element specific features of the sample as well. This is the scanning Bragg diffraction microscopy setup that can be found at the Hard X-ray Nanoprobe of the Center of Nanoscale Materials (CNM) at Argonne National Laboratory (APS) [26].

resistive switching mechanism in neuromorphic computing architectures. Local structural and electronic characterizations that can be achieved through microscopy with nanometer resolution is therefore necessary to investigate the materials with local heterogeneities. A scanning probe microscopy technique that uses a nanoscale x-ray beam has thus been developed to directly investigate the local properties across a thin-film sample. This technique can only be found at bright x-ray sources such as third-generation synchrotrons, and due to the penetration of depth of x-rays, can probe the structure beyond the surface properties that is a principal limitation for electron microscopy.

While coherence is not essential for nanodiffraction, the spatial coherence length

obtained from focusing the beam spot to tens of nanometers is advantageous, especially for materials in thin-film geometry. Since the illuminated volume is already quite small with a nanoprobe, the scattered intensity is typically much weaker compared to other probes at these large-scale facilities. Having all incoming wavevectors satisfying the Bragg condition therefore optimizes the scattered signal for data collection. A standard nanoprobe setup that relies on diffractive optics such as the one at the Center of Nanoscale Materials is shown in Fig. 2.7 [26, 28, 29]. A Fresnel zone plate (FZP) focuses the x-rays where the focal length is dependent on the photon energy by the relation

$$f = \frac{D dr_n}{\lambda}, \tag{2.6}$$

where $f$ is the focal length, $D$ is the outside diameter of the FZP, and $dr_n$ is the width of the outermost zones of the FZP, and $\lambda$ is the photon energy. For a standard hard x-ray experiment at 10 keV, this corresponds to a focal length of about 26 mm from the zone plate [28]. An order sorting aperature (OSA) follows the FZP to filter out higher diffraction orders before the nanoprobe impinges the sample. By tuning to a particular structural peak and performing raster scans across the sample, it is possible to resolve the strain, the degree of mosaic spread, and fraction of phases (metallic and insulating phases near a transition temperature for example) that is distributed across the sample. For a high quality film, the diffraction pattern is overlaid on an imprint of the FZP (as seen in Fig. 2.7) and it is possible to resolve the strain and rotation of lattice planes through proper analytical techniques [26]. Chapter 6 details how the rotation and strain of LSMO nanoislands is resolved in this manner. Otherwise, the strain can be resolved using a series of 2D maps about the Bragg peak of interest — the strain propagation across a PZT/LSMO heterostructure is determined with this method and explained in Chapter 5.

# Chapter 3

# Orbital Domain Dynamics in Magnetite ($\text{Fe}_3\text{O}_4$) Below the Verwey Transition

## 3.1 Abstract

Despite countless experimental probes into magnetite's electronic structure across the Verwey transition $\text{Fe}_3\text{O}_4$, the exact origin of this archetypical metal-insulator transition remains a puzzle. Advanced x-ray diffraction techniques have mostly resolved the monoclinic structure of the insulating phase, including interatomic bond lengths, but the complexity of the charge-orbitally ordered state is difficult to disentangle. We combined resonant elastic x-ray scattering and x-ray photon correlation spectroscopy to probe orbital fluctuations in the insulating state of magnetite. By accessing the Bragg forbidden $(00\frac{1}{2})$ peak at the Fe $L_3$ and O $K$ edges, we reveal the dynamics of the Fe 3d and O 2p orbital domains. Our results show that the orbital domain fluctuations in the low-temperature state is due to the long-suspected electron hopping at the Fe $\text{t}_{2g}$ orbital sites of trimeron chains whereas the O

2p orbital network is static, indicating a suppression of double exchange and superexchange interactions.

## 3.2    Introduction

Macroscopic phenomena in quantum materials such as superconductivity, colossal magnetoresistance, and metal-insulator transitions are manifestations of the correlations between the electronic and lattice structures at the atomic scale [30, 6, 31]. Resolving competing order parameters originating from the electron spin, charge, and orbital states as well as mesoscale effects such as domain wall evolution is key to understanding how to tailor these materials for electronic applications. In magnetite ($Fe_3O_4$), the mechanism behind its metal-insulator transition, famously known as the Verwey transition, continues to confound physicists. In the high-temperature metallic state, magnetite has a cubic inverse spinel structure consisting of two sublattice sites. The A sites are characterized by $O^{2-}$ and $Fe^{3+}$ ions that are tetrahedrally coordinated while B sites are octahedrally coordinated consisting of $O^{2-}$ ions and [$Fe^{2+}$, $Fe^{3+}$] ions in equal proportion [32, 33]. The iron atoms of the A and B sites are also antiferromagnetically coupled through hybridization with the oxygen 2p orbitals. When magnetite is cooled below the transition temperature $T_v \approx 120$ K, a structural phase transition occurs where the cubic structure (a=b=c=8.387 Å) distorts to monoclinic one (a=b=11.88 Å, c = 16.775 Å and $\beta = 90.236$º) and is simultaneously accompanied by a drop in electrical conductivity by two to three orders of magnitude [34, 35]. Verwey postulated that this insulating state arises from the freezing of a *B*-site conduction electron into a charge-ordered state of alternating $Fe^{2+}$ and $Fe^{3+}$ on the octahedral sublattice [35]. Although experiments have since disproven Verwey's original theory, the presence of a significantly more complex charge and orbitally-ordered insulating state has been shown below the transition temperature.

## 3.3 Probing Orbital Order with Resonant X-Rays

In the monoclinic phase, cooperative Jahn-Teller (JT) distortions shorten interatomic bond lengths of $B$-site Fe cations into linear three-site chains known as trimerons, the quasiparticle that has been proposed as the order parameter describing the charge-orbitally ordered insulating state [36, 37]. In particular, a trimeron consists of $B$-site iron atoms that are charge ordered in $Fe^{3+}$- $Fe^{2+}$- $Fe^{3+}$ chains where the electron occupation of the degenerate Fe $t_{2g}$ orbitals give rise to the orbitally ordered structure as seen in Fig. 3.1(a). In transition-metal oxides, Kugel and Khomskii have shown that orbital ordering arises from either JT coupling of electrons to the lattice or hopping of transition metal electrons into specific orbital states [38, 39, 40]. In the case of magnetite, the orbital order manifests as a Bragg forbidden $(00\frac{1}{2})$ peak that can only be accessed at Fe and O resonant energies [41, 42, 43]. The stability of this orbital structure depends on the strength of orbital hybridization and changes in orbital occupation on both the iron and oxygen sites that can occur in two ways: (i) direct 3d electron hopping between iron sites referred to as direct d-d electron hopping. (ii) indirect electron hopping between iron sites through the oxygen atoms by superexchange and double exchange processes [36, 44].

We combined resonant elastic x-ray scattering (REXS) and x-ray photon correlation spectroscopy (XPCS) to investigate the electron exchange interactions that give rise to these orbital fluctuations. By accessing the $(00\frac{1}{2})$ peak in scattering geometry at the Fe $L_3$-edge and the O $K$-edge, we probe the Fe 3d and O 2p orbital occupancies via excitations from core to unoccupied valence states at the Fe $2p_{3/2} \rightarrow$ 3d and O 1s $\rightarrow$ 2p transitions [42, 43]. Specifically, the Fe $L_3$-edge resonant signal directly probes the Fe $t_{2g}$ orbital structure of octahedral sites while the O $K$-edge is sensitive to the O 2p states that are hybridized to the Fe 3d orbitals present on both the octahedral and tetrahedral sites as seen in Fig. 3.1(a) and Fig. 3.1(b), respectively [42, 43, 45, 46, 47]. Our results show that in the low-temperature monoclinic phase, the network of oxygen 2p orbital structures is

extremely stable while the Fe $t_{2g}$ orbital ordering is still thermally active due to continuous d-d electron hopping between adjacent $B$-site Fe cations within trimeron chains.
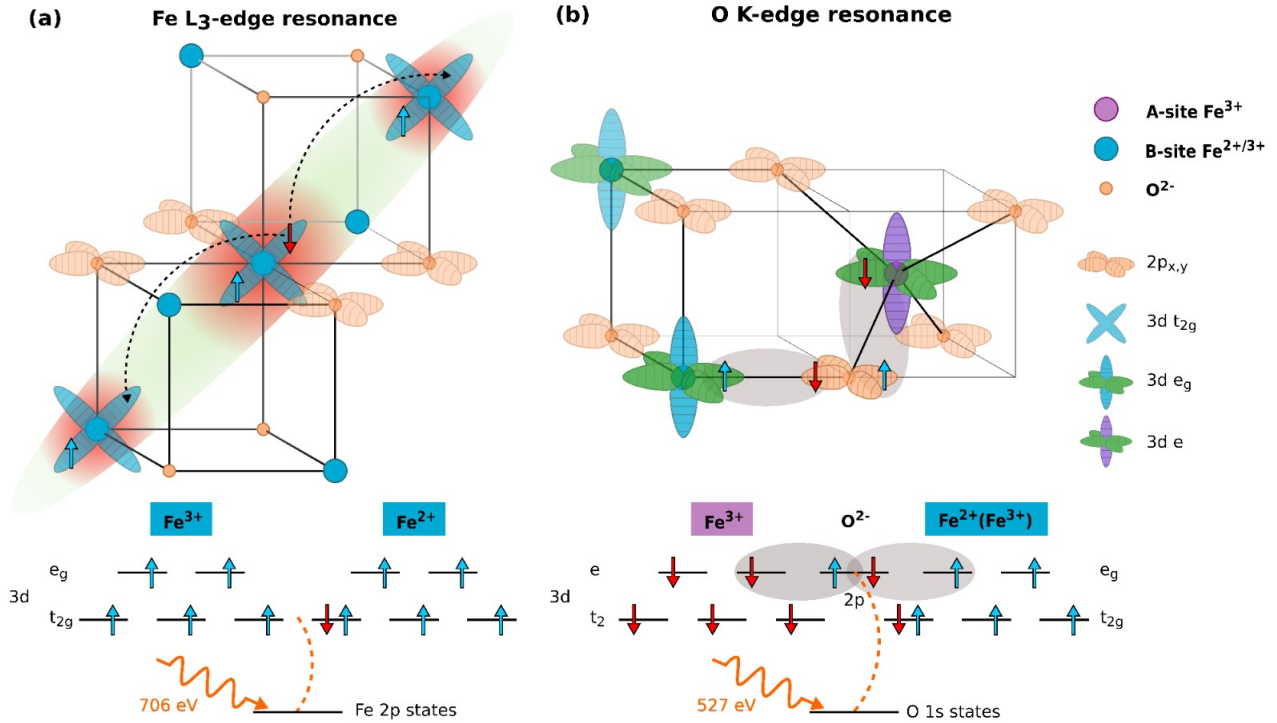


**Figure 3.1**: **(a)** Fe $L_3$-edge resonance (2p $\rightarrow$ 3d states) probes the orbital occupancy of the $t_{2g}$ electrons of the $B$-site Fe cations. Since the orbital order is not linked to lattice dynamics, the signal originates from direct d-d electron hopping within corner sharing trimeron chains. In the diagram, the extra electron in the central $Fe^{2+}$ can hop directly to neighboring $Fe^{3+}$ $t_{2g}$ sites along the trimeron. **(b)** The O $K$-edge resonance (1s $\rightarrow$ 2p states) probes the oxygen 2p orbital states that are hybridized to both the $t_{2g}$ and $e_g$ orbitals on the octahedral and tetrahedral iron sites. The lobes of the $B$-site Fe-$e_g$ and O-2p orbitals are aligned forming $\sigma$ bonds, and therefore are more strongly hybridized compared to the hybridization between the $A$-site Fe-$e_g$ or any of the $t_{2g}$ orbital states with the O-2p orbitals. The gray highlighted region shows a possible antiferromagnetic superexchange interaction between an A and B site Fe cation.

## 3.4  Experimental Setup

The resonant XPCS experiment was conducted at the Coherent Soft X-ray (CSX) beamline at the National Synchrotron Light Source II (NSLS-II). A 50 nm thick magnetite

thin film grown epitaxially on MgO(001) by reactive sputtering in $Ar/O_2$ environment was used for this experiment. The magnetite film quality was characterized by x-ray diffraction, and resistivity measurements showed a metal-insulator transition at $T_v = 116$ K for the heating cycle, as seen in Fig. 3.2. A schematic of the experimental scattering geometry is shown in Fig. 3.3 where a coherent x-ray beam is tuned to the Fe $L_3$-edge (705.7 eV) and O $K$-edge (527.2 eV) resonant energies to probe the $(00\frac{1}{2})$ peak. The sample alignment was performed at 25 K where the energy was optimized in a fixed-Q energy scan as shown in Fig. 3.4(a,c), and the sample geometry was subsequently optimized in $\theta$-$2\theta$ as shown in Fig. 3.4(b,d). The (001) Bragg peak is also accessible in the monoclinic phase, but not necessarily at resonance, meaning this peak is allowed purely based on the crystal symmetry of the low-temperature state [13]. Therefore, we also monitored the (001) Bragg peak off resonance at 800 eV to isolate the structural order from any charge- or orbitally-ordered signal.
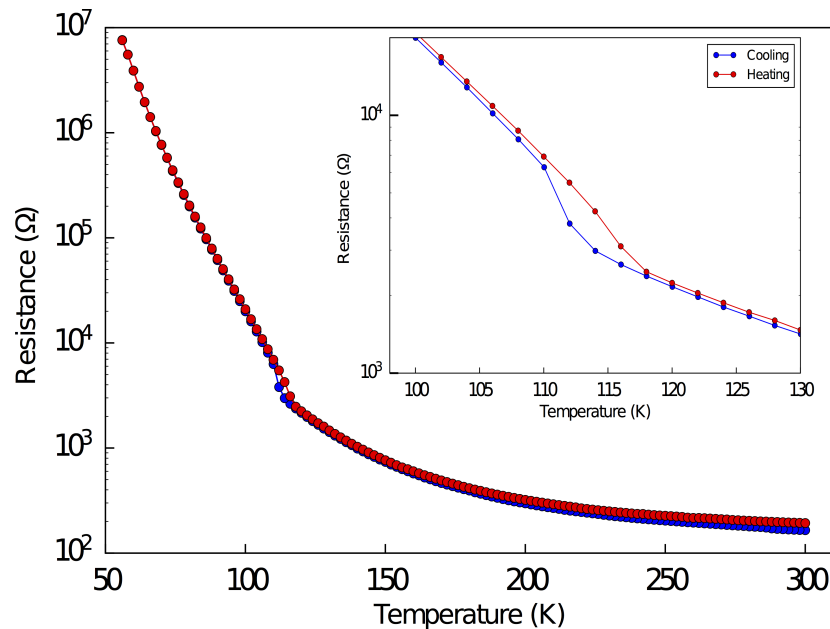


**Figure 3.2**: Metal-to-insulator transition for 50 nm thin films of $Fe_3O_4$ used for the experiment at NSLS-II CSX beamline where $T_V = 110$ K and 116 K for cooling and heating cycles, respectively.

A CCD detector with 30 um x 30 um pixel size located 34 cm from the sample was used to record the measurements, and an example of the detector image for the $(00\frac{1}{2})$ peak at the O $K$-edge resonance is shown in Fig. 3.5(a). The degree of contrast can be visualized from a line cut through the central speckle pattern as shown in Fig. 3.5(b). A Gaussian function was used to fit the peak where the full width at half maximum (FWHM) in reciprocal space, $\Delta Q$, is used to define the correlation length $\lambda = 1/\Delta Q$. Superimposed in Fig. 3.5(b) is the (001) Bragg peak at 800 eV that shows the correlation length of the lattice structure is approximately ten times greater than the orbital correlation length, indicating the oxygen 2p orbital domains are not defined by structural domain boundaries. The $(00\frac{1}{2})$ peak at the O $K$-edge resonance was measured between 25 K to 109 K and its correlation length and integrated peak intensity as a function of temperature are shown in 3.5(c). The corresponding correlation lengths and integrated peak intensity for the $(00\frac{1}{2})$ peak at the Fe $L_3$-edge is shown in 3.9(b). The correlation lengths of the $(00\frac{1}{2})$ peak at the O $K$-edge and Fe $L_3$-edge well below the Verwey transition temperature are approximately 13 nm and 16 nm respectively, which is consistent with literature data [42, 48]. The integrated peak intensity, a measure of the percentage of insulating domains in the system, follows the same trend for the iron and oxygen resonant edges as expected since both signals are only sensitive to the insulating monoclinic phase.

## 3.5   Results

The speckle pattern overlaid on the $(00\frac{1}{2})$ peak is the fundamental attribute in the XPCS technique that allows us to measure dynamics of the system. When a coherent beam interacts with the nanoscale heterogeneities, in this case orbital domains, the interference between the coherent beam and the nanoscale heterogeneities create the speckle pattern seen within the $(00\frac{1}{2})$ peak. Since we have a stable coherent beam, any fluctuations of the
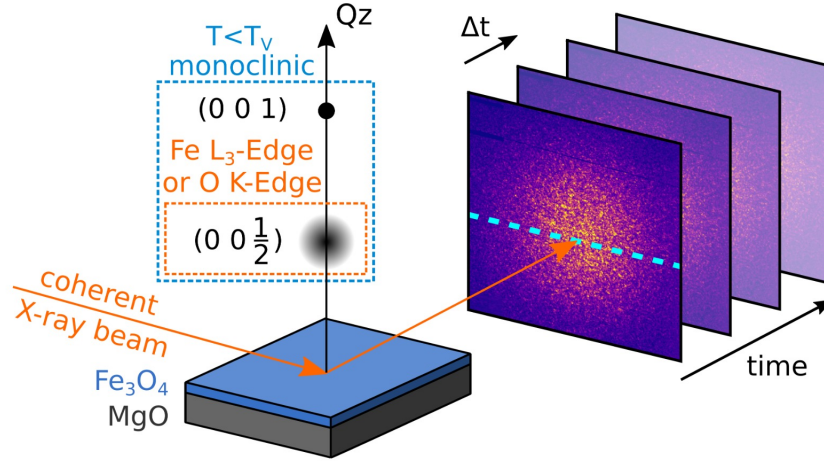
**Figure 3.3**: Experimental setup of the XPCS experiment where coherent soft x-rays are tuned to the Fe $L_3$-edge (705.7 eV) and the O $K$-edge (527.2 eV) to access the $(00\frac{1}{2})$ peak that only exists in the low-temperature monoclinic phase at resonance. The $(001)$ is also a forbidden Bragg peak that can be accessed in the low-temperature state, though not necessarily at resonance. A CCD records the speckle pattern of the $(00\frac{1}{2})$ peak at the O $K$-edge resonance with a delay time of $\Delta$t between each image.

orbital domains will manifest itself as spatial and temporal intensity changes in the speckle pattern. Therefore, by correlating the intensity of successive speckle patterns, it is possible to resolve the dynamic timescale of the system from how fast or slow the speckle pattern decorrelates in time.

We can analyze the dynamics by calculating the $g_2(\mathbf{q}, t_1, t_2)$ two-time intensity-intensity autocorrelation function given in Eq. 3.1 where the intensity of the $(00\frac{1}{2})$ peak is correlated pixel-by-pixel with itself at different times, $t_1$ and $t_2$, during the entire scan. No q-dependence was found in the dynamics, and therefore the central speckle pattern extending out to the FWHM for both the iron and oxygen resonant edges was used to calculate the two-time correlation function. Scans at each temperature were recorded immediately after the sample temperature setpoint was reached, and the scans lasted 4 hours with a delay time of 1 second between successive detector images (2 seconds for the 109 K measurement). The normalized correlation plots for the Fe $L_3$-edge and O $K$-edge at 85 K, 90 K, and 100 K are shown in Fig. 3.6, but the first 30-45 minutes of each scan can
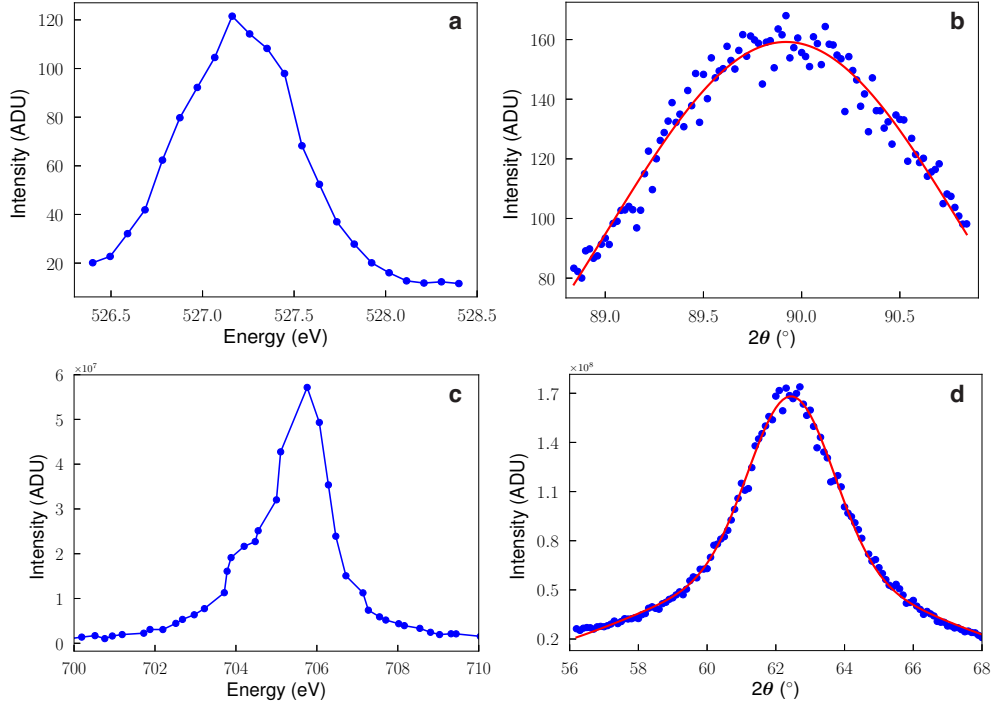
**Figure 3.4**: Energy and $2\theta$ alignment scans for the the the $(00\frac{1}{2})$ superlattice reflection at 25 K. **(a,b)** The intensity of the $(00\frac{1}{2})$ peak as a function of energy and $2\theta$, respectively, at the O $K$-edge resonant conditions. **(c,d)** The intensity of the $(00\frac{1}{2})$ peak as a function of energy and $2\theta$, respectively, at the Fe $L_3$-edge resonant conditions. *Note: The average intensity was used for the O $K$-edge alignment while the total integrated intensity was used for the Fe $L_3$ edge.*

be ignored due to instability as the sample equilibrated. The two-time correlation plots for all temperature measurements between 25 K and 109 K are shown in Fig. 3.7

$$g_2(\mathbf{q}, t_1, t_2) = \frac{\langle I(\mathbf{q}, t_1) I(\mathbf{q}, t_2) \rangle}{\langle I(\mathbf{q}, t_1) \rangle \langle I(\mathbf{q}, t_2) \rangle} \tag{3.1}$$

From the correlation plots, we see that the signal at the Fe $L_3$-edge is continuously dynamic throughout the scan while a static signal is seen at the O $K$-edge. After normalizing to the average intensity of the speckle pattern, the $t_1 = t_2$ line is the fully correlated reference value while lines orthogonal to $t_1 = t_2$ show increasing delay time between speckle patterns. In Fig. 3.7, the region where the sample is stable is marked by the dotted black lines, and for the O $K$-edge signal, the correlation value is approximately the same as the $t_1$
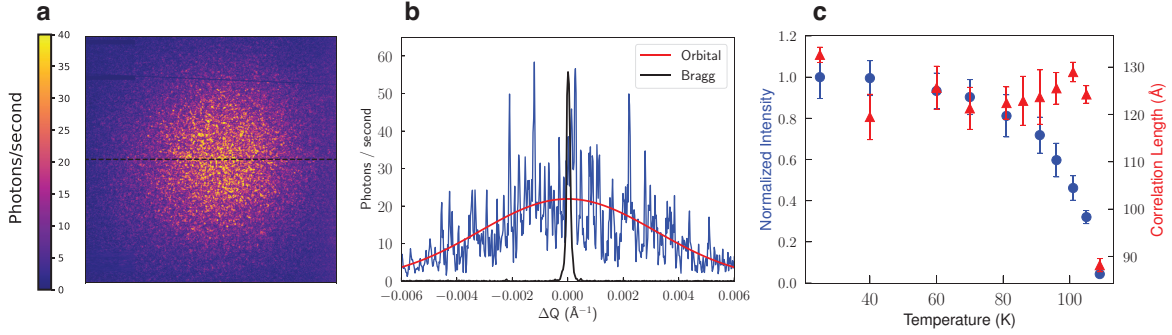
**Figure 3.5**: **(a)** A CCD detectore image of the $(00\frac{1}{2})$ superlattice peak at the O $K$-edge resonant energy at 27 K. **(b)** A line cut through the speckle pattern in (a) that shows the degree of contrast of the signal. A Gaussian function is fitted to the $(00\frac{1}{2})$ orbitally-ordered peak, and the (001) Bragg reflection is superimposed to show the difference in the orbital and structural correlation lengths. **(c)** The normalized integrated intensity of the $(00\frac{1}{2})$ peak per second at the O $K$-edge as a function of temperature is plotted along with the correlation length defined by $1/\Delta Q$, where $\Delta Q$ is the FWHM of the Gaussian fit to the peak as seen in (b).

$= t_2$ value at all points, indicative of a static signal. On the other hand, the correlation value drops away from the $t_1 = t_2$ line for the Fe $L_3$-edge, showing the speckle pattern is changing in time.

Since the two-time correlation plots for the Fe $L_3$-edge exhibit characteristic patterns of equilibrium dynamics, we can also visualize the dynamics by creating "waterfall" plots or kymographs as seen in Fig. 3.8(a) and Fig. 3.10, which depict the evolution of the speckle pattern as a function of time. These waterfall plots are intensity vs. time plots, and show the measured intensity along the line cut through the central speckle pattern.From the kymograph plot for 27 K, it is clear that the observed speckles remain stable throughout the three-hour measurement and no evolution of the speckle pattern is observed. On the other hand, for temperatures closer to the Verwey transition, at 70 K and 90 K, fluctuations in the speckle pattern are observed with speckles appearing and disappearing as a function of time.

It is also possible to further quantify the dynamic timescale from the $g_2(\mathbf{q},t)$ one-time autocorrelation function defined in Eq. 3.2 where $I(\mathbf{q},\tau)$ and $I(\mathbf{q},\tau+t)$ are intensities
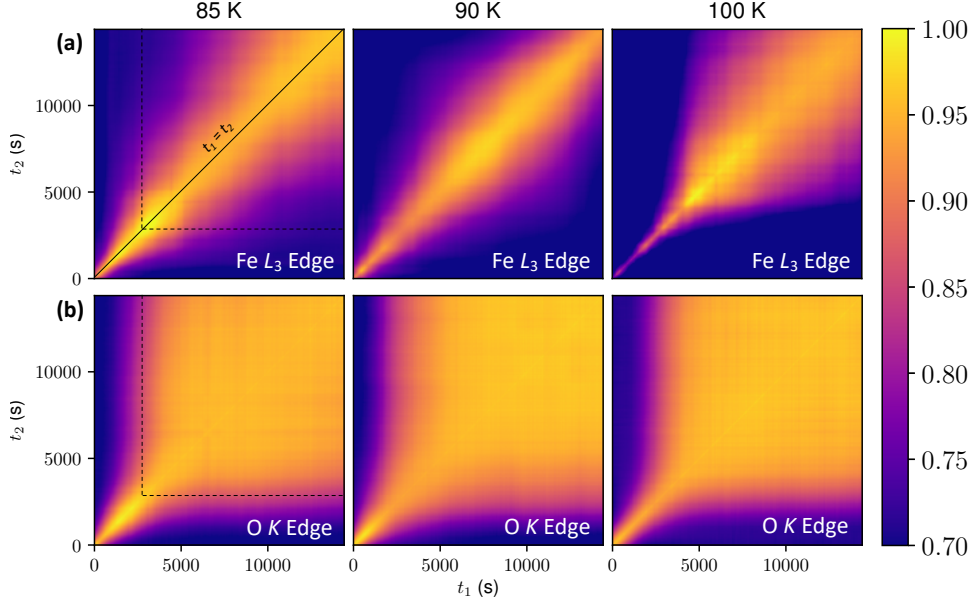
**Figure 3.6**: Normalized two-time intensity-intensity autocorrelation functions defined by Eq. 1 for the **(a)** Fe $L_3$-edge and the **(b)** O $K$-edge at 85 K, 90 K, and 100 K. A 1s exposure time was used for each scan that lasted 4 hours. The first 30-45 minutes of each scan is attributed to sample instability from temperature equilibration — the approximate stable region of the scan is marked by the dotted line. The $(00\frac{1}{2})$ signal at the Fe $L_3$-edge that is sensitive to the Fe $t_{2g}$ orbital structure is clearly dynamic while the O $K$-edge signal that is sensitive to the O 2p orbital structure remains static.

of a given pixel separated in time by $t$, and the $g_2(\mathbf{q},t)$ is calculated from averaging all pixels for a given $\Delta q$ range of 1.5 x $10^{-3}\text{Å}^{-1}$ in the speckle pattern.

$$g_2(\mathbf{q},t) = \frac{\langle I(\mathbf{q},\tau)I(\mathbf{q},\tau+t)\rangle_\tau}{\langle I(\mathbf{q},\tau)\rangle_\tau^2} \tag{3.2}$$

This autocorrelation function calculated from the intensities is related to the intermediate scattering function (ISF), $|F(\mathbf{q},t)|^2$, as defined in Eq. 3.3 where A is the speckle constrast directly related to the spatial and temporal coherence of the x-ray beam. For ergodic systems, the ISF follows a stretched exponential trend defined by $F(\mathbf{q},t) = e^{-(t/\tau)^\beta}$ where $\tau$ is the decay consant and $\beta$ is the stretching exponent. The temporal evolution of the ISF for temperatures ranging from 27 K to 102 K is shown in Fig. 3.8(b) with an ISF value of 1
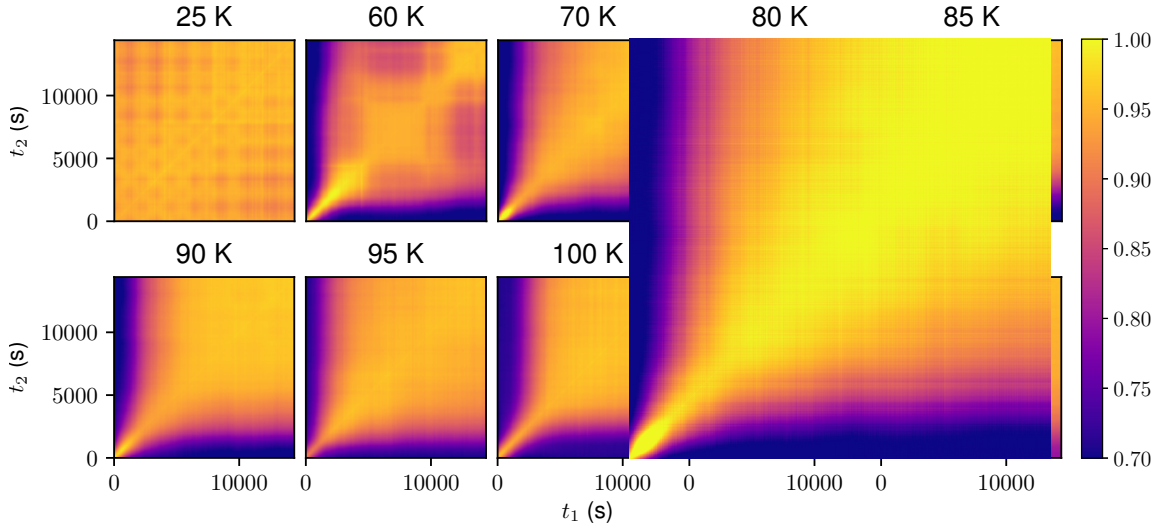
**Figure 3.7**: Normalized two-time intensity correlation plots for all temperature measurements between 25 K and 109 K of the $(00\frac{1}{2})$ peak at the O $K$-edge (527.7 eV) resonance

representing a completely correlated system while 0 represents a fully decorrelated system.

$$g_2(\mathbf{q},t) = 1 + A|F(\mathbf{q},t)|^2 \tag{3.3}$$

We observe a strong temperature dependence of the ISF, where the timescales increase as the sample temperature is increased from 27 K to approximately 90 K. However, surprisingly, as the temperature is further increased from 90 K to 102 K, a decrease in the fluctuation decay time, $\tau$, is observed. Fig. 3.9(a) shows the values obtained for $\tau$ and $\beta$ as a function of temperature. The error bars were calculated using the uncertainty in counting statistics for different q-regions since there is no q-dependence. We found the value of the stretching exponent to be greater than 1 ($\beta$ fit=1.5), manifested by the compressed shape of the ISF. A compressed exponential with $\beta > 1$ represents a collective or jamming behavior while a value of $\beta < 1$ indicates more liquid-like fluctuations [49]. Furthermore, the obtained fit value of 1.5 in magnetite is considered a universal signature of collective relaxation behavior, and has been previously observed in soft matter systems i.e. gels,

sponges etc. [49, 50], materials exhibiting charge density waves [21], and magnetic systems [51].
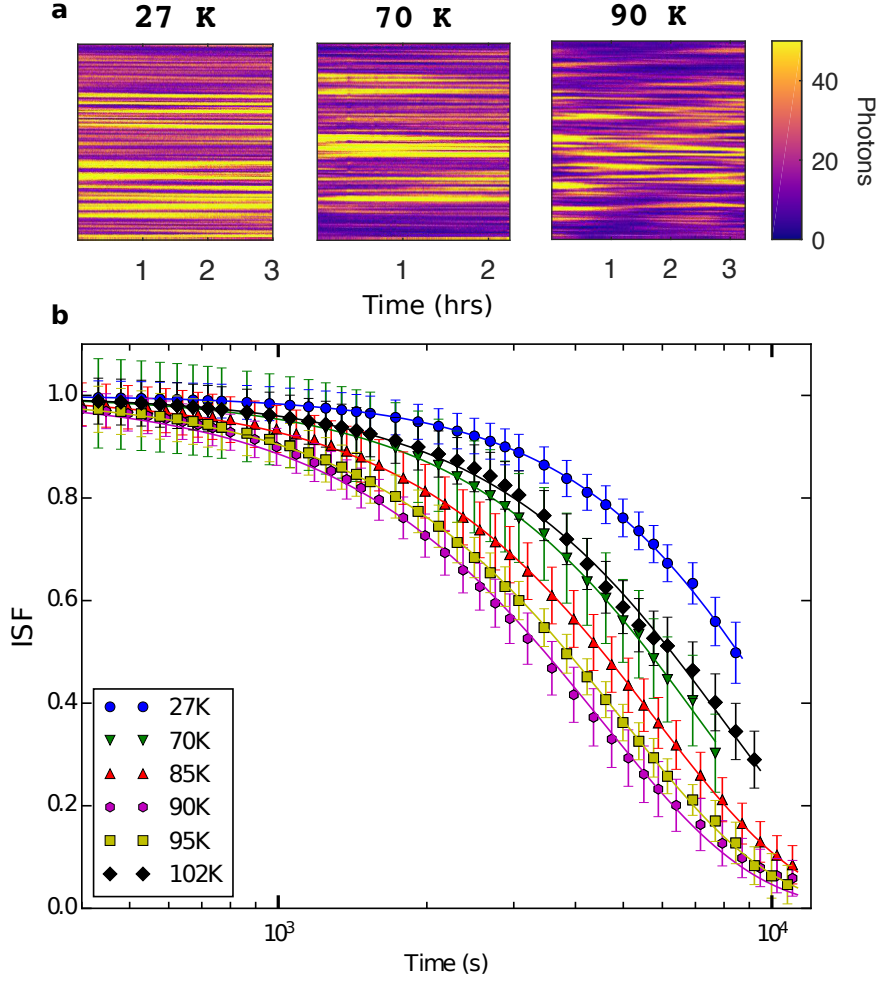


**Figure 3.8**: **(a)** Kymographs or 'waterfall' plots at selective temperatures to demonstrate orbital dynamics in the magnetite film. The waterfall plots are obtained by plotting the central line cut through the speckle pattern, as shown in Fig 3.5(a) but for the Fe $L_3$ $(00\frac{1}{2})$ peak, as a function of time throughout each scan. **(b)** Intermidiate scattering function (ISF) and fits to the ISF from Eqs. (1) and (2) are plotted as a function of time for selected temperatures.

As observed in the ISF plots, the fluctuation timescales given by $\tau$ exhibit a minimum near T = 90 K. This nonlinear behavior can be divided into two regimes, (i) below 90 K where $\tau$ decreases as temperature increases and (ii) above 90 K, where $\tau$ increases as

temperature increases. The first regime was fitted using the standard thermally activated Arrhenius behavior (as shown in Fig. 3.9(a)) with an activation barrier of $\Delta E/k_B = 32 \pm 5$ K. This activation energy represents the effective energy for orbital domain fluctuations, which grow as more thermal energy is added to the system albeit still significantly below the Verwey temperature. Similar dynamics have been previously observed in other correlated systems such as Cr, manganites, and magnetic systems (Dy and Ho) [49, 50, 21, 51]. However, the second regime, where slowdown of fluctuation timescales approaching the transition temperature is observed, cannot be described by the thermally-activated behavior.

The temperature dependence of the $(00\frac{1}{2})$ reflection is shown in Fig. 3.9(b) and its variation across the Fe $L_3$-edge. Correlation lengths of the orbital domains were also plotted as a function of temperature and are shown in 3.9(b). The correlation length was obtained from a fitted Gaussian peak (as shown in Fig. 2(b)) of the central speckle pattern, with the correlation length ($\lambda$) defined as $1/\Delta Q$ where $\Delta Q$ is the full width at half maximum (FWHM) of the fitted Gaussian. The observed FWHM at 27 K is 6.4 x $10^{-3}$ Å$^{-1}$ resulting in a correlation length scale of 15.7 nm, which represents the average size of domains with a visible impact on the speckle pattern. The estimated value of orbital ordering correlation length is an order of magnitude lower than lattice ordering correlation length scales and is similar to previously observed values in bulk magnetite of 11-37 nm [42, 52]. The difference in correlation length scales from the orbital and structural ordering indicates higher levels of disorder in orbital ordering not observed for structural ordering. Although the origin of lower values of orbital ordering length scales is still not well understood, strain effects, internal defects and doping have been suggested to play a key role [53, 54]. For magnetite, it has been interpreted as a signature of disorder in orbital occupancy of $t_{2g}$ orbitals by the Fe$^{2+}$ electron [42, 52]. Similar values of orbital correlation length scales have been observed in manganite systems ($\sim 30$ nm) where it is associated with orbital glass-like state existing on well-ordered lattice of charge order [53, 54, 55].

By combining the peak intensity, correlation timescales and length scales, we can now describe the underlying process behind the insulator-to-metal transition. In the first regime (below 90 K), as more thermal energy is injected into system, the fluctuations in orbital order increases and therefore, a decrease in fluctuation timescale is observed. The peak intensity stays almost constant, indicating that the system is still insulating. Once the fluctuations achieve a critical energy (near 90 K), the system enters into a second regime and the phase transformation begins. In the second regime (above 90 K), $\tau$ increases as the temperature increases, and the thermally activated Arrhenius behavior breaks down. The peak intensity decreases indicating a reduction in the amount of insulating phase. This implies a transformation of insulating state to metallic state, which significantly changes the boundary conditions of the remaining insulating domains consisting of an orbitally- ordered trimeron network. This is also consistent with the observed decrease in correlation lengths of orbitally-ordered domains from 17 nm to 6 nm with a normalized integrated peak intensity drop of 80% to 10% near 100 K. In this phase separation regime, the metallic/insulating interface leads to the pinning of the trimeron chains, resulting in a slowdown of orbital fluctuation timescales.

With the results from the O $K$-edge, we can further conclude that while nucleating metallic domains govern the change of characteristic dynamic timescales at the B-site Fe $t_{2g}$ states, the origin of the fluctuations is due to thermally-driven, direct hopping of the conduction electron between $t_{2g}$ states along trimeron chains as seen in Fig. 3.1(a). Both the O $K$-edge and Fe $L_3$ resonant signals are only sensitive to the insulating phase and can be seen from the drop in total intensity as metallic domains begin to nucleate approaching the metal-insulator transition temperature. If there is enough thermal energy to drive structural fluctuations between metallic and insulating phases at each temperature, that would manifest as a dynamic speckle pattern at both the O $K$-edge and Fe $L_3$-edge. The static signal at the O $K$-edge indicates an absence of structural fluctuations and therefore

cannot be the source of the dynamic speckle pattern seen at the Fe $L_3$-edge.

Ruling out any structural fluctuations, the origin of the dynamic speckle pattern at the Fe $L_3$-edge and the static speckle pattern at the O $K$-edge must be electronic in nature. The speckle pattern is a fingerprint of the orbital-specific electron occupancies, and any changes to this configuration will result in a different speckle pattern. Considering the hybridization between the O 2p states to all of the Fe 3d states at both the tetrahedral and octahedral sites, we expected to see the dynamic Fe $L_3$-edge signal sensitive to the octahedral $t_{2g}$ states to partially contribute to O $K$-edge signal, but that is not the case. At the oxygen sites, antiferromagnetic superexchange interactions where an electron hops between an octahedral and tetrahedral iron site via the O 2p orbital states and double exchange interactions where an electron hops between octahedral iron sites through the O 2p orbitals are both possible. The collective electron exchange interactions over time would alter the O $K$-edge speckle pattern. Therefore, the static speckle pattern at the O $K$-edge shows that superexchange and double exchange electron exchange interactions are mostly absent or suppressed in the monoclinic phase of magnetite. Since there is no electron hopping via the oxygen sites, the dynamic signal at the Fe $L_3$-edge can only be attributed to the direct hopping of the conduction electron between $t_{2g}$ states along trimeron chains as seen in Fig. 3.1a.

Above 116 K, the speckles completely disappear, indicating a complete transformation to the metallic phase. This transition temperature observed at the $(00\frac{1}{2})$ reflection matches well with the conductivity data which shows the metal-to-insulator transition at 116 K. Here we note the $(00\frac{1}{2})$ orbital ordering reflection is sensitive to the insulating phase in this regime and does not reveal the nature of the emergent metallic phase.
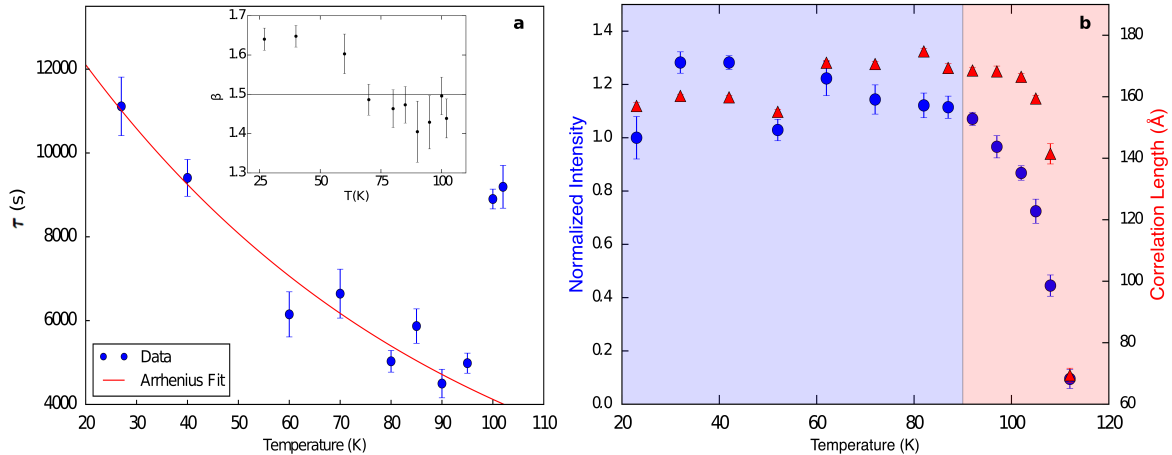
**Figure 3.9**: **(a)** Characteristic orbital fluctuation timescales as a function of temperature obtained from fits to the intermediate scattering function data shown in Fig. 3.6(b). An Arrhenius trend (red line) with an activation energy of $\Delta E/k_B = 32 \pm 5$ K is fitted in the first regime ($< 90$ K). Inset shows the fitted stretched exponential value, $\beta$, as a function of temperature that describes the nature of the dynamics. **(b)** The integrated intensity of the $(00\frac{1}{2})$ peak and the correlation length scales of the insulating domains is calculated from a fitted Gaussian to the central speckle pattern where the correlation length, $\lambda$, is $1/\Delta Q$ where $\Delta Q$ is the FWHM of the fitted Gaussian peak.

## 3.6 Discussion

Our results are supported by well-established theory on orbital ordering in transition-metal oxides by Khomskii and Kugel and recent studies of the trimeron network [44, 56]. The strength of orbital hybridizations, and consequently the potential for electron interactions, depends on the degree of orbital overlap between neighboring sites, and has been generalized as the Goodenough-Kanamori-Anderson rules [44]. Strong ferromagnetic double exchange interactions can occur independently through 180° bonds on both the $A$- and $B$-sites via the oxygen atoms while strong antiferromagnetic superexchange interactions can occur through the $\mathrm{Fe}_{A(e)}$-O-$\mathrm{Fe}_{B(t_{2g})}$ and $\mathrm{Fe}_{A(t_2)}$-O-$\mathrm{Fe}_{B(e_g)}$ channels. By measuring the charge-orbitally ordered $(00\frac{1}{2})$ peak at the O $K$-edge resonance, we probe the aforementioned electron interactions that occur through the oxygen atoms. Our static signal indicates that minimal or no electron hopping occurs at the oxygen sites in the low-temperature monoclinic phase
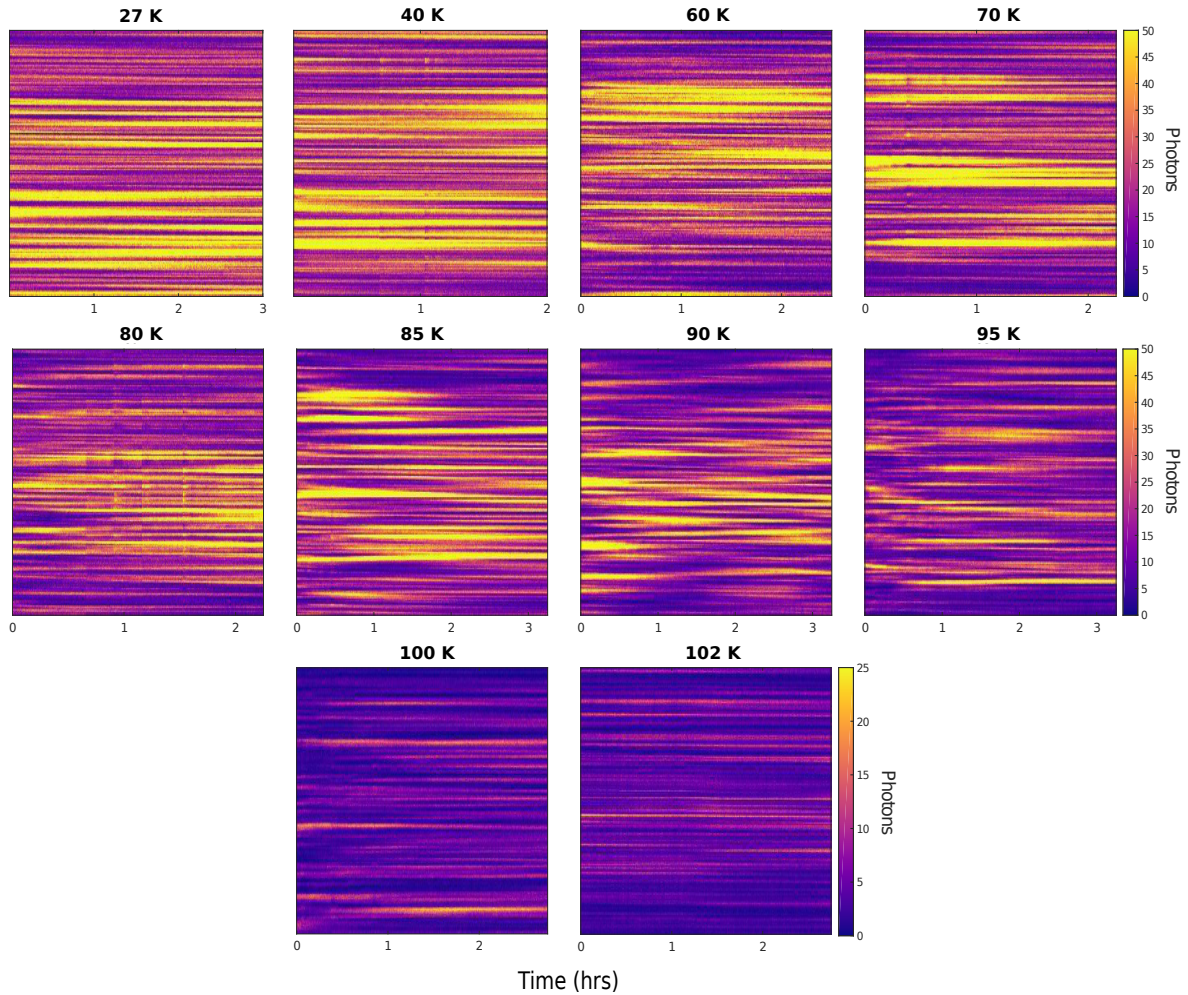
**Figure 3.10**: Kymographs or 'waterfall' plots at the Fe $L_3$ edge for all temperatures where XPCS scans were taken.

of magnetite regardless of orbital hybridization strength tied to the oxygen sites. This nanoscale picture is also seen in other systems such as cubic vanadates where quantum effects among $e_g$ orbitals are mainly suppressed by JT distortions [57]. Another possible electron hopping mechanism can occur directly between the 3d sites of neighboring iron cations if there is strong orbital overlap, and this is the case for $B$-site $t_{2g}$ orbitals where the lobes are directed towards each other as seen in Fig. 1a. In the case of magnetite, the interatomic distance of Fe cations are shortened within trimeron chains, creating even stronger orbital overlap that allows for direct d-d electron hopping [36]. The dynamic

signal seen at the Fe $L_3$-edge in our measurements that is sensitive to only the $t_{2g}$ sites of the *B*-site Fe cations is experimental confirmation of the direct d-d electron hopping.

## 3.7 Conclusion

In summary, we have shown an experimental approach that uses x-ray photon correlation spectroscopy at resonant elastic geometry to directly probe the strength of orbital hybridizations and its effects on electron exchange interactions in magnetite by exploiting a Bragg-forbidden, orbitally ordered peak. Our results have shown that contrary to Verwey's hypothesis that the conduction electron freezes in the insulating state, there is still sufficient thermal energy in the system to drive these electrons to hop along trimeron chains. The absence of electron exchange interactions at the O-2p orbitals and the Fe-3d orbitals outside of the trimeron chains further suggest that only the Fe cations within trimeron chains play a role in the Verwey transition. Finally, magnetite belongs to a class of transition-metal oxides where the interaction of the transition-metal 3d electrons with the field of $O^{2-}$ ligands is responsible for many fascinating nanoscale effects that give rise to various classes of electronically ordered materials [38, 47, 56, 55]. With new generation coherent x-ray synchrotron sources, we can employ the same experimental technique to reveal unseen dynamical trends in other materials with strong electron correlations such as nickelates and cuprates.

## 3.8 Acknowledgements

Chapter 3, in full, is a reprint of the materials Orbital Domain Dynamics in Magnetite Below the Verwey Transition adapted from Physical Review Letters, Roopali Kukreja, Nelson Hua, Joshua Ruby, Andi Barbour, Wen Hu, Claudio Mazzoli, Stuart Wilkins, Eric E. Fullerton, and Oleg G. Shpyrko (2018), 121, 177601 and Dynamic and Suppressed Electron Exchange Interactions in Magnetite Below the Verwey Transition currently under review for Physical Review Letters, Nelson Hua, Jianheng Li, Stjepan B. Hrkac, Andi Barbour, Wen Hu, Claudio Mazzoli, Stuart Wilkins, Roopali Kukreja, Eric E. Fullerton, and Oleg G. Shpyrko (2020). The dissertation author was the second author to the first publication and the primary investigator and first author of the second publication.

# Chapter 4

# Measuring Electron-Phonon Coupling Timescales in Chromium by Photoexcitation

## 4.1  Introduction

Charge density wave (CDW) order is an important component of many quantum material phase diagrams as it often acts as a competing or cooperative order to magnetic and superconducting states [58, 59, 60]. The role of electron-electron and electron-phonon interactions involved in these mixed phase states or near CDW order-disorder transitions play a vital role in the emergent behavior of these systems. However, investigation into the role of the CDW with x-rays is often difficult to perform. To couple to the CDW often requires resonant x-rays that produce either weak signals [58] or an enhanced signal of a lattice peak where the CDW is convolved with the lattice. Furthermore, many of these superconducting and magnetic material systems are stoichiometrically complex with various doping levels that renders pinpointing the electronic effects to specific sites difficult. Here,

we perform an x-ray pump-probe experiment on elemental chromium, a stoichiometrically simple system, to investigate the electron-phonon coupling timescales from the CDW.

Chromium is an itinerant aniferromagnet with an incommensurate CDW and spin-density wave (SDW) first detected by neutron scattering in 1959 [61, 62]. Recent x-ray experiments on thin film chromium samples have revealed a CDW pinned at the interfaces with a phase transition around T = 220 K [63, 64, 65, 66]. In both bulk and thin films, the CDW appears as satellites about the (002) Bragg peak in reciprocal space. In bulk Cr, the position and intensity of the satellite peaks reveal the amplitude and period of the CDW, but the phase is lost [67]. In thin films however, the finite thickness of the film gives rise to Laue oscillations or fringes where the CDW satellite peak interferes with the Laue fringes on either side of the (002) Bragg peak at $(0, 0, 2 \pm\delta)$ [63]. This interference allows us to determine the phase, revealing a CDW with pinned antinodes at the interfaces and 7.5 periods for a 28 nm thin film sample [63]. By following the evolution of $\delta$ or change in the CDW position relative to the Laue fringes, a transition region of 220-240 K was revealed between a CDW with 7.5 periods above the transition temperature and 8.5 periods below the transition temperature [64]. In the transition region, there is a coexistence of phases between the two quantized CDW periods. Previously, an x-ray pump probe experiment at 115 K showed that an ultrafast photoexcitation enhances the CDW amplitude above its equilibrium value and was attributed to electron-phonon interactions [65]. Here, we extend the same experiment to encompass a range of temperatures above and below the transition region to extract electron-phonon coupling times.

## 4.2   Experimental Setup

A 28 nm thin film of chromium was synthesized on MgO(001) by DC magnetron sputtering at a temperature of 500° C and annealed for one hour at 800° C. The Néel
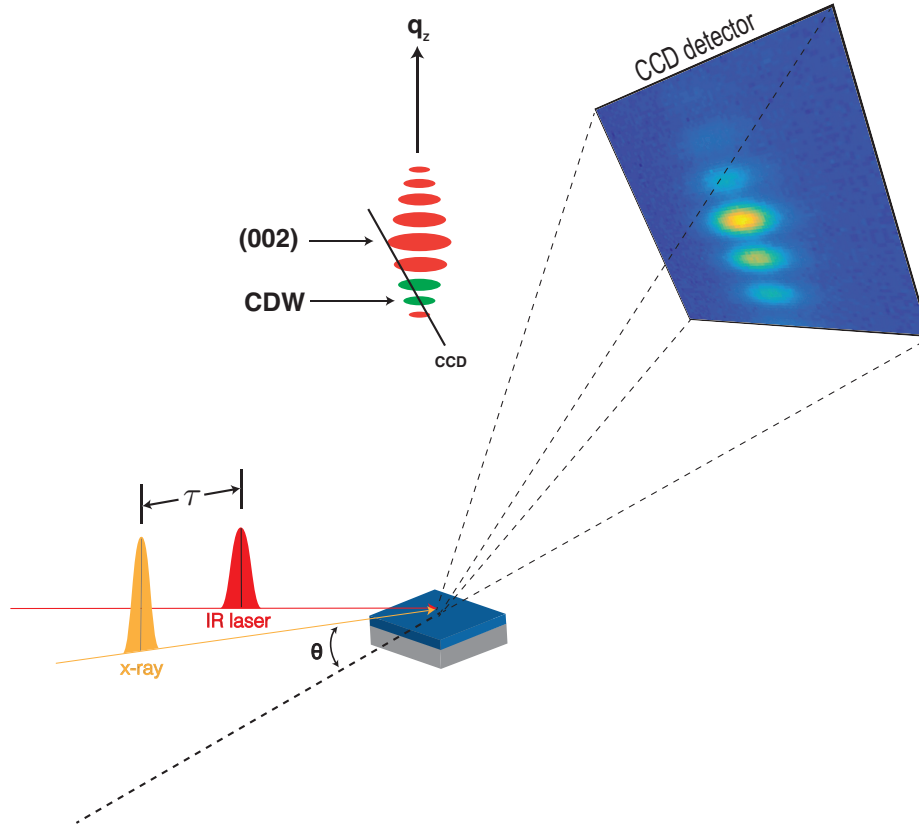
**Figure 4.1**: The sample is aligned to the (002) Bragg peak where the high quality, finite film thickness gives rise to the Laue fringes shown in the schematic. The CDW order exists on the $7^{th}$ and $8^{th}$ fringes of the (002) peak, and the sample and detector are further optimized so that the detector slices through both of the fringes. An optical laser with 40 fs pulses is used to excite the system while an XFEL pulse with a varied delay of $\tau$ subsequently probes the system.

temperature of the film was determined to be 290 K and x-ray diffraction showed good crystal quality that is further demonstrated by the signal measured at the x-ray free electron experiment. The x-ray pump-probe experiment was conducted at the XPP beamline of the Linac Coherent Light Source (LCLS) at the Stanford Linear Accelerator Center. A schematic of the experimental setup is shown in Fig. 4.1 where the sample and CCD detector were aligned to the CDW-enhanced $7^{th}$ and $8^{th}$ fringes of the (002) Bragg peak, around q = 4.2 Å$^{-1}$. An optical laser with 40 fs pulses was used where three fluences designated as high (4 mJ/cm$^2$), medium (2 mJ/cm$^2$), and low (1 mJ/cm$^2$) were set by

controlling the angle of the wave plate. Diffraction patterns were collected for a series of time delays, $\tau$, between the optical laser pulse and the x-ray pulse spanning a range of 0-12 ps, with a resolution of 50 fs step sizes. These measurements were conducted between 110 K - 300 K in increments of 20 K steps, except for the 190 - 260 K range where 10 K step sizes were used to cover the transition region.

## 4.3   Results

The CCD detector images were reduced by averaging the intensity along the $q_z$ axis and plotted as a function of time delay as shown in the top row of Fig. 4.2 for select temperatures. The evolution of the CDW is evident from the $7^{th}$ to $8^{th}$ fringe, and by integrating the intensity of those two fringes for each time delay, we can follow the transient amplitude as seen in the bottom row of Fig. 4.2. The intensity is normalized to the static amplitude of the fringe coming from the interference of the Laue oscillation and the CDW. The transient CDW intensity can then be modeled by equation 4.1 where $A_F$ is the final CDW amplitude (or the amplitude of the static CDW), $B$ is the amplitude of the modulated sinusoidal decay, $t_p$ is the period of oscillation, $t_d$ is the daming time of the oscillation, $t_0$ is the offset, $t_{ep}$ is the decay time for the shift of the quasi equilibrium towards $A_F$, and C = $A_F$ - $A_1$ as depicted in the schematic of Fig. 4(d) of [65]. The fits are shown in Figs. 4.4 and 4.5 where fits to both fringes were made only in the 220-230 K region; otherwise, the signal-to-noise ratio of the CDW was too low to obtain accurate fits. Finally, the temperature and fluence dependence of the time-dependent evolution of the photoexcited CDW is shown in Fig. 4.3.

$$A(\tau) = A_F + B \cdot \cos\left(2 \cdot \pi \cdot \frac{\tau - \tau_0}{t_p}\right) \cdot \exp\left(-\frac{\tau - \tau_0}{t_d}\right) - C \cdot \exp\left(-\frac{\tau - \tau_0}{t_{ep}}\right) \qquad (4.1)$$
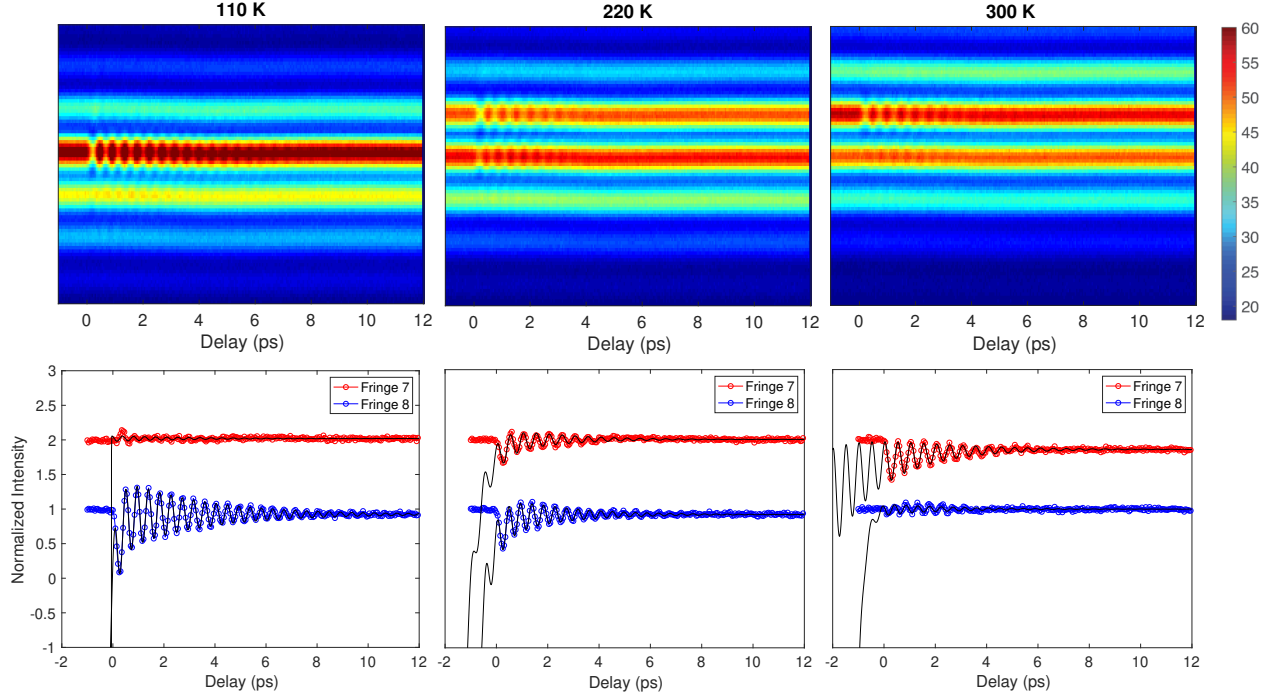
**Figure 4.2**: **(Top Row)** Integrated intensity along the $q_z$ axis about the $7^{th}$ and $8^{th}$ fringes where the CDW is as a function of time delay. Near the transition temperature of 220 K, the photoenhanced CDW is present on both fringes. **(Bottom Row)** Fits to the oscillating CDW intensity for both fringes using Eq. 4.1
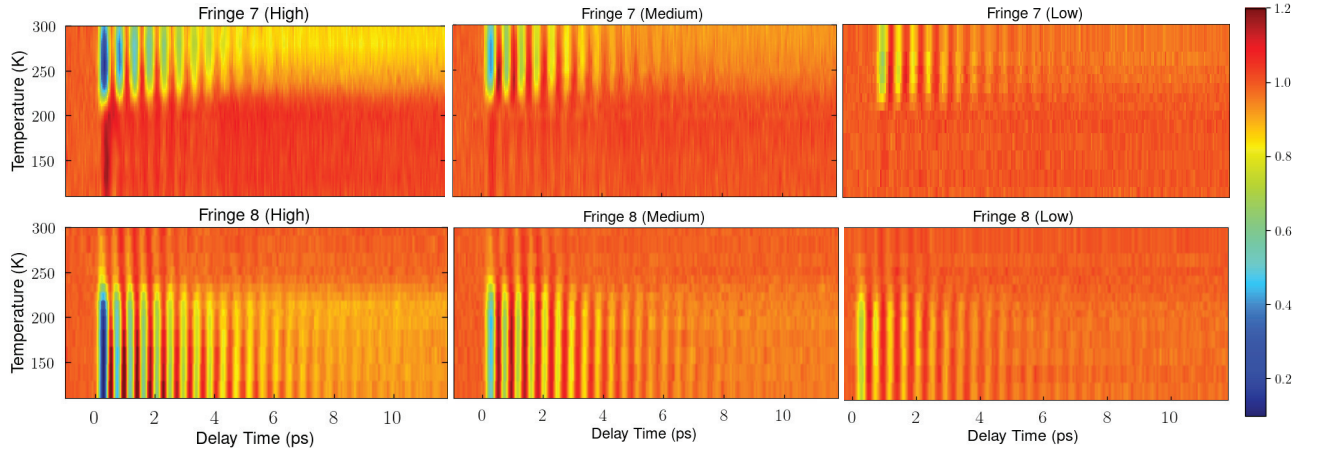


**Figure 4.3**: The time-resolved temperature dependence of the photoinduced enhanced CDW for high (4 mJ/cm$^2$), medium (2 mJ/cm$^2$), and low (1 mJ/cm$^2$) fluences.

The electron-phonon coupling times as a function of temperature and fluence are shown in Fig. 4.4(a). At low temperatures, the electron-phonon time constant is approximately 0.2 ps and remains relatively constant up to the transition region, except

49

for the high fluence. Above the transition where the system is mostly in the 7.5 period CDW phase, there is a significant increase in $t_{ep}$ and we see a fluence dependence. This indicates the shift in the quasi equilibrium position of the CDW persists longer for a CDW with a smaller periodicity. The Néel temperature at 290 K potentially plays in role in the fluence dependence of the electron-phonon coupling time where the photoexcitation at higher temperatures puts the system above the Néel transition for a longer times. The damping time shown in Fig. 4.5 is approximately 3 ps for all fluences in the low temperature state, and is in agreement with previous measurements where the long time scale points to phonon-phonon interactions as the principal decay mechanism. The damping time decreases to about 2 -2.5 ps at higher temperatures as expected where the periodicity of the CDW is lowered. The remaining fits are presented in Fig. 4.5 where the 110 K fits match well with the 115 K fits from a previous experiment [65].
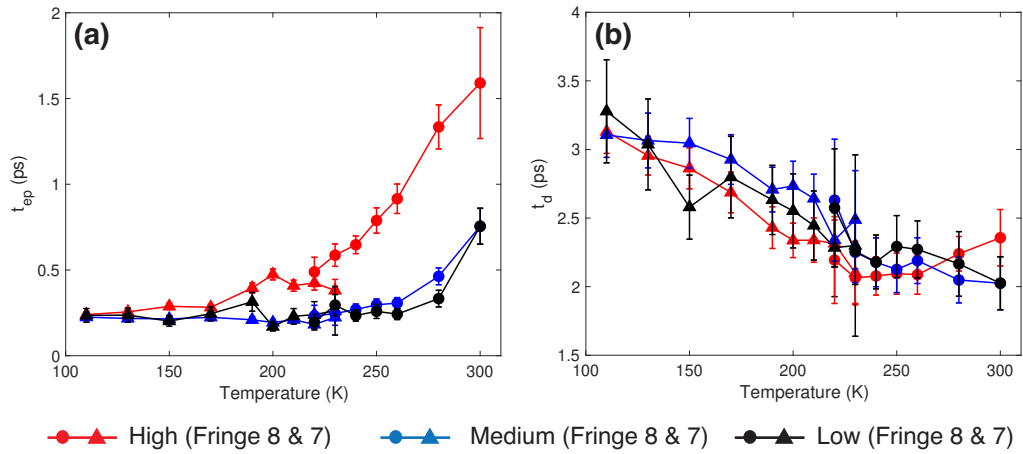


**Figure 4.4**: Extracting the electron-phonon coupling time **(a)** and the damping time **(b)** from fits to the transient CDW amplitude. There is a clear increase in the electron-phonon coupling times at all fluences with increasing temperature whereas a decrease in the damping time with temperature is seen for all fluences.
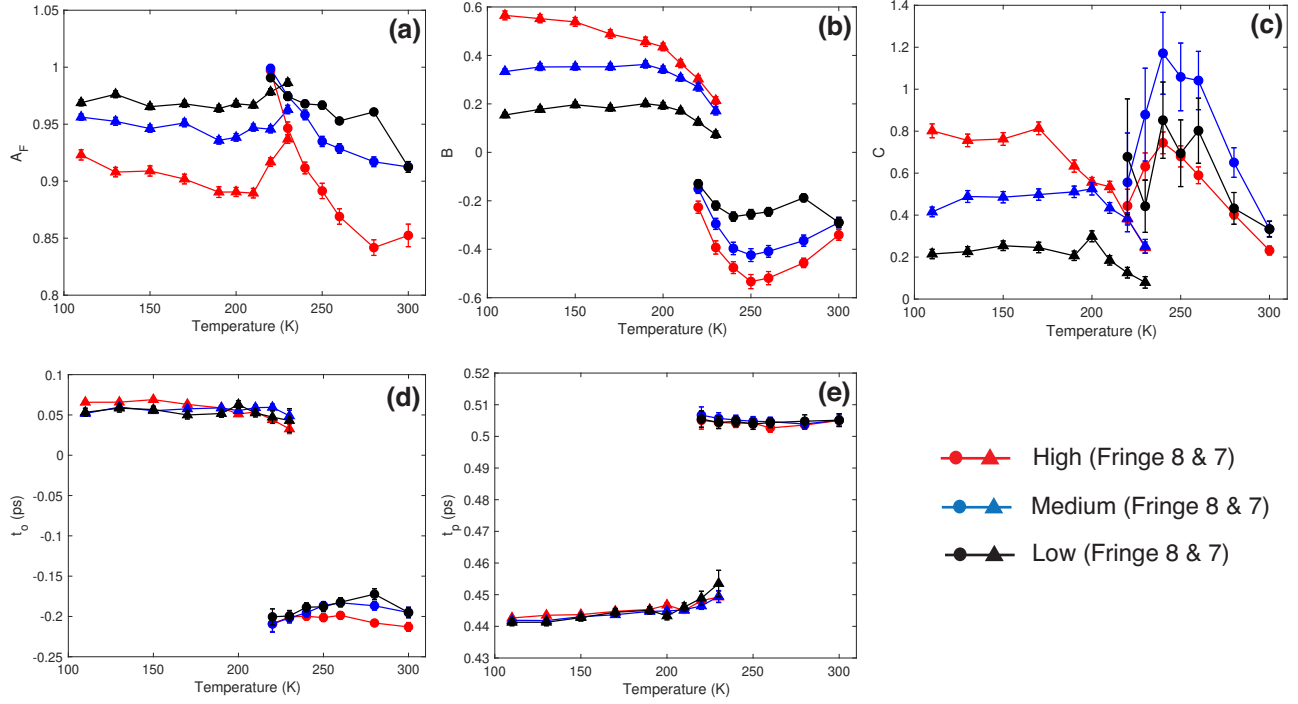
**Figure 4.5**: The remaining fit parameters where **(a)** $A_F$ is the final CDW amplitude (or the amplitude of the static CDW), **(b)** $B$ is the amplitude of the modulated sinusoidal decay, **(c)** C = $A_F$ - $A_1$ as depicted in the schematic of Fig. 4(d) of [65], **(d)** $t_0$ is the offset, and **(e)** $t_p$ is the period of oscillation.

## 4.4 Acknowledgements

# Chapter 5

# Nanoscale Imaging of Electrically-Tuned Strain Fields in a Ferroelectric/Ferromagnetic Heterostructure

## 5.1 Abstract

Recent advances in the control of magnetism at the nanoscale now provide unique opportunities in developing energy efficient spintronic-based memory and logic devices due to emergent behaviors such as magnetic ordering and magnetic phase separation [12, 13, 68]. Traditionally, manipulating the magnetic properties of complex materials can be achieved by varying the temperature or composition (doping), but alternative methods like strain-induced modification of magnetic domains has been less explored. Nanostructures can accommodate larger values of strain (up to 10% in some cases), and can be applied using various epitaxial growth methods and dynamically altered by an external

stimulus. Therefore, lattice strain can be used as a tuning parameter to modify magnetic properties on the nanoscale or even introduce novel magnetic phases (such as skyrmions) that can be applied in advanced functional materials. To understand the response from multiferroric materials that uses an intermediary strain field as a coupling mechanism, x-ray nanodiffraction was used to spatially resolve the coupled strain field between PZT and LSMO, a ferroelectric/ferromagnetic heterostructure, that results from an applied electric field in the ferroelectric PZT layer.

## 5.2   Introduction

Engineering composite device structures in which the ferromagnetic-ferroelectric interfaces are coupled via a magnetostrictive and piezoelectric strain is an active area of research seeking to create new functionalies in materials systems [69]. Theoretical and experimental evidence have confirmed the sensitivity of the magnetic state to strain fields as small as $10^{-4}$ [70]. Therefore, the magnetization response is expected to be highly anisotropic and consequently, spatially dependent. A previous study using a Kerr microscope has already shown dynamic domain wall motion in the ferromagnetic stack (magnetic spin-valve) from a piezoelectric signal, but no strain information was obtained [17]. In this study, PZT thin films are used as the piezoelectric material where the application of an electric field displaces negative and positive charge carrier centers, leading to an electric polarization and lattice distortions. This PZT layer is epitaxially coupled to the LSMO layer that acts as the ideal ferromagnetic layer due to its magnetostriction and colossal magnetoresistance (CMR) properties.

By driving the piezoelectric response using an externally applied electric field, we hope to modify or induce the magnetic behavior in the ferromagnetic LSMO film via the epitaxial lattice coupling (strain at the interface) as the primary mechanism. As seen in

Fig. 5.1(a), the difference in the magnetic hysteresis loop for LSMO grown directly on STO compared to LSMO grown on PZT is evidence of possible defects or strain due to the interface that modifies the magnetic anisotropy in the system. In many composite devices where PZT is used, an out-of-plane electric field across the PZT film thickness is applied to drive the polarization state, which means PZT is clamped on either side by electrodes [refs]. Freestanding PZT structures has only recently been fabricated and are shown to have structural and electronic properties that are different than clamped PZT [71, 72]. Intuitively, the absence of a substrate or electrode on the surface can potentially allow for more dynamic strain and polarization states. Here, we aim to apply an in-plane strain to a freestanding PZT structure with a thin bar of LSMO grown epitaxially on PZT.
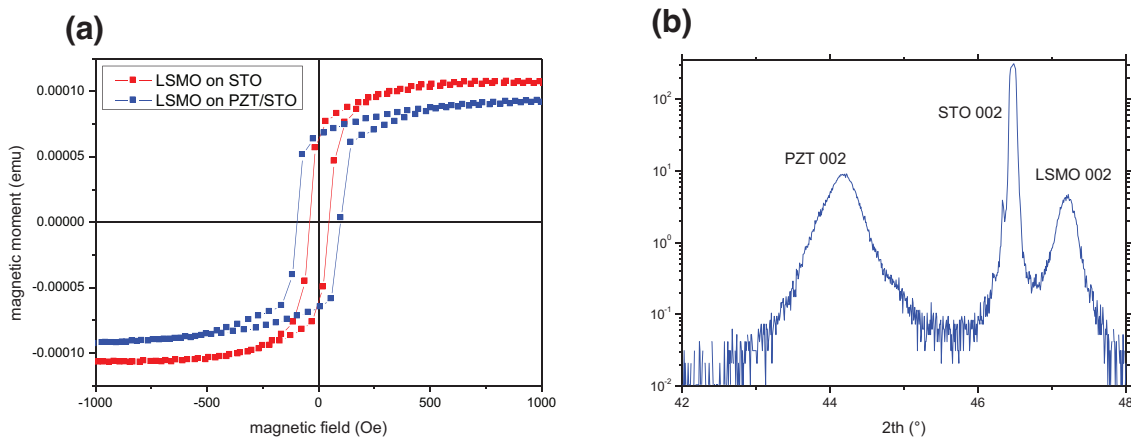


**Figure 5.1**: **(a)** The magnetic hysteresis loop of LSMO when grown directly on STO compared to LSMO grown on the PZT. The modified hysteresis loop is evidence of defects or strain in the system. **(b)** The x-ray diffraction profile of the device structure about the (002) peak.

The characterization of the nanoscale distribution of strain was performed with high resolution x-ray nanodiffraction while the resulting magnetic properties of the film were measured using x-ray photoemission microscopy (X-PEEM) in order to understand how the applied electric field affects magnetic properties such as magnetic domain formation, magnetic anisotropy, and magnetic domain wall motion. This is a multifaceted project that

seeks to answer questions in both fundamental condensed matter physics and materials science. Both PZT and LSMO belong to a class of strongly correlated electron materials, and through this study, we aim to elucidate the correlation between the charge and lattice degrees of freedom in PZT and the magnetoelastic coupling in LSMO. Furthermore, determining the strain propagation between the two layers allows us to engineer dynamically functional materials from epitaxial growth methods that can be additionally enhanced and actively controlled via an electrically driven *in-situ* strain field.

## 5.3   Ferroelectric and Ferromagnetic Layers

Altering the doping levels of $Pb(Zr_x:Ti_{1-x})O_3$ has been a standard method to control functional properties as it has been shown that the permittivity, piezoelectric coefficients, and aging rates are highly dependent on doping ratios [73]. In x = 0.7, PZT exhibits less mosaic spread with larger domains whereas x=0.52 is characterized by smaller domains with a larger relative permittivity that allows for ease of domain reorientation in the presence of an electric field. Therefore, we used the x=0.52 doping level in order to maximize the potential for strain propagation across the interface. LSMO has been shown to exhibit strain-tunable magnetic anisotropy by various epitaxial growth methods [74, 75], and is thus a suitable ferromagnetic layer to investigate electrically-tuned magnetic domain formation via strain at the interface.

The device structure is shown in Fig. 5.2 where a 100 nm thick film of PZT with lateral dimensions of 5 x 30 µm is grown on an STO subtrate by pulsed laser deposition (PLD). A 40 nm layer of LSMO is subsequently deposited and etched away into a bar with 1 x 30 µm lateral dimensions. Larger Au electrodes are deposited along the length of the PZT film where an in-plane electric field will be applied while smaller Au electrodes are connected at the ends of the LSMO bar to monitor the capacitance.

## 5.4 Experiment

The nanodiffraction experiment was carried out at the Hard X-ray Nanoprobe at the Center of Nanoscale Materials of Argonne National Laboratories, where the experimental setup using diffractive optics is shown in Fig. 2.7. The 25 µm beam spot size was achieved by adjusting the focal length of the Fresnel zone plate (FZP) with the aid of a fluorescence detector. The Au fluorescence signal was recorded as a function of step size across the edges of the Au electrodes where the optimized focal length corresponded to the sharpest dropoff in intensity. The PZT and LSMO (002) Bragg peaks were separately optimized with rocking curves and θ-2θ scans at an x-ray energy of 10 keV. Following each optimization of the Bragg peak, 2D maps from raster scans across the device covering a lateral area of 1.2 x 2.6 µm for LSMO and 2 x 4 µm for PZT at the center of the device were performed. A schematic of the raster scan measurements of the nanodiffraction experiment and the recorded diffraction pattern is shown in Fig. 5.2(a). To obtain an accurate value of the strain, the maps were performed at the optimized Bragg peak angle and $\pm$ 0.15°. Due to the spread of incoming wavevectors from the diffractive optics, the center-of-mass of the peak contains both strain and lattice rotation contributions, but the sum of these three maps averages out the lattice rotation to give purely the lattice constant. These 2D maps were measured at the voltages of [0 V, 5 V, 10 V, 15 V, 20 V] for both the LSMO and PZT (002) structural peaks with additional [0 V, -5 V, -10 V, -15 V, -20 V] measurements for the PZT (002) peak to track hysteretic behavior. The PZT (013) structural peak was also mapped for the [0 V, -5 V, -10 V, -15 V, -20 V] voltages, but the signal from the LSMO (013) peak was too weak to track.

Due to the scanning nature of the x-ray microscopy technique, the limitation of scanning times allowed for just a portion of the 30 µm long device. The central region of each device was aligned at the beginning of each 2D map by performing orthogonal line scans across the device. The Au fluorescence signal indicated the edges of the PZT device

56

in both width and length. Both the Mn and Au fluorescent signals were also used in the analysis to correct for smaller misalignments between maps. For example, Fig. 5.3(b,d) show how the projected Au and Mn fluorescence intensity across the width of the device look.
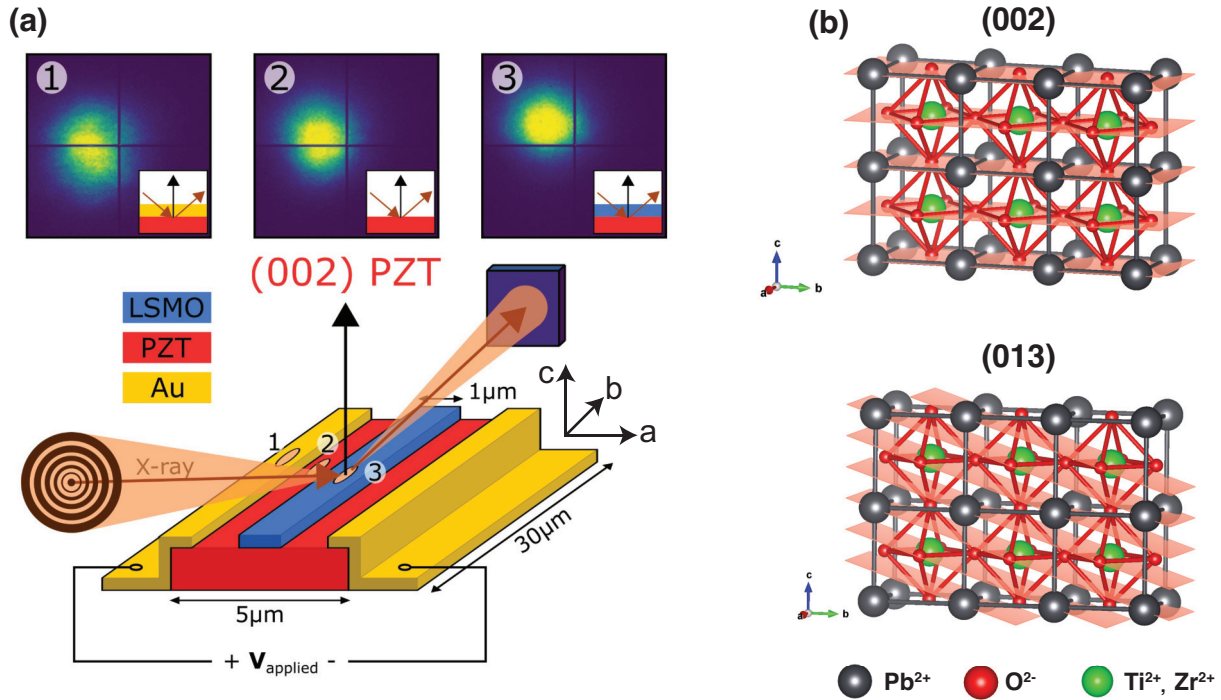


**Figure 5.2**: **(a)**The device consists of a 40 nm bar of LSMO that is 1 μm in width grown epitaxially on a 100 nm film of PZT. A 25 nm x-ray beam is used to raster scan across the PZT/LSMO device while a CCD detector records the diffraction pattern at each point, specifically following the (002) structural peak of LSMO and PZT as well as the (013) structural peak of PZT. Nanodiffraction maps of the device were performed with an *in-situ*, in-plane electric field between 0-20 V. **(b)** The lattice planes corresponding to the diffraction peaks of PZT probed.

## 5.5   Results

Pb($Zr_{0.52}$:$Ti_{0.48}$)$O_3$ is a perovskite ferroelectric with a tetragonal crystal structure (approximately a=b=4.05 Åand c = 4.15 Å  depending on various growth conditions) with a polarization vector directed along the c-axis. Due to the high relative permittivity that
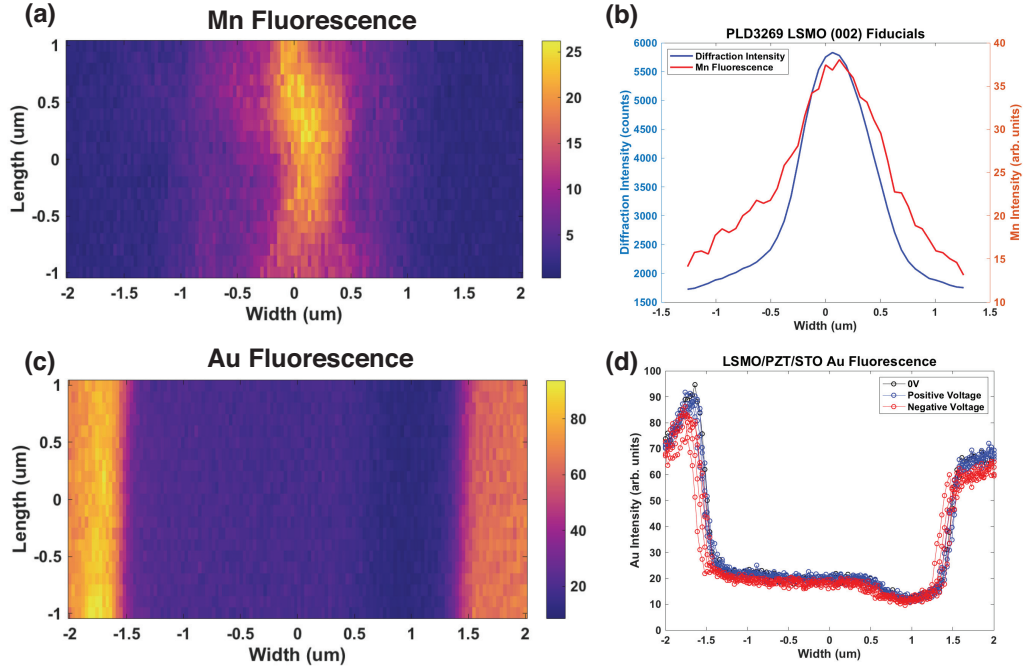
**Figure 5.3**: **(a,c)** A fluorescence detector is simultenously used to monitor the fluorescence signal coming from Au and Mn. These are used to locate the device, monitor drifts, and correlate regions when comparing different voltage scans. **(b)** The Mn fluorescence and diffraction peak intensity during a line scan across the device. **(c)** The projected Au fluorescence signal for various scans can be used to more accurately align and compare regions on the device.

allows for 90° domain reorientation, it is possible to have a mixed phases of the two domain orientations. For example, powder samples of PZT using a standard Rigaku system showed both the (002) and (200) diffraction peaks, and by following the changes in relative intensity of both peaks as a function of applied electric field, the fraction of 90° domain reorientations was determined [76]. The XRD of the PZT (002) film in our device structure, shown in Fig. 5.1(b) shows a single peak corresponding to the c-axis, meaning there is only one domain reorientation with the polarization vector directed out-of-plane.

The 2D maps of the lattice spacing as a function of voltage are shown in Fig. 5.4. From the (002) diffraction signal, we can directly calculate the LSMO and PZT c-axis lattice constant while the d-spacing of the (013) lattice planes are shown. Evidently, the high spatial resolution of the probe reveals the spatial heterogeneities in the individual

layers, but as expected, the average lattice constants of PZT and LSMO without an applied electric field correspond to approximately 4.1 Å and 3.85 Å, respectively. Fig 5.5(a,b,c) show the average lattice spacings across the width of the device. The shaded gray and beige regions mark the location of the LSMO bar and the Au electrodes, respectively, determined by the point of half maximum of the Mn and Au fluorescence signals. The strain across the bar shown in Fig. 5.5(d,e,f) are calculated by using the 0 V signal as the reference. We note the lattice spacing of LSMO shows an asymmetry across the bar, and the resulting voltage-induced negative strain also shows an asymmetric contraction, though to a lesser extent. The PZT (002) and (013) signals both show an asymmetry where there is a large positive strain near the driving electrode. However, at both the driving and grounded electrodes, the PZT strain is partially suppressed under the Au electrodes as evidenced by the abrupt change in strain state at the electrode edges.

The 2D maps of the integrated intensity of the diffraction peaks at each point are shown in Fig. 5.6. The features of the nanoscale heterogeneities can be seen in the intensity maps, which are also used to correlate the scan regions at each voltage. For example, the features from the intensity maps of LSMO show that roughly the same region was scanned before each voltage scan, though there are still minor drifts. In all cases, there is an increase in the diffraction peak intensity, to varying degrees, as a function of increasing voltage. The average PZT (002) and (013) Bragg peak intensities across the device depicted in Fig. 5.7 show the region of increased intensity is near the driving electrode. The (002) peak only shows a maximum increase of intensity by about 12% for the highest voltage while the (013) peak shows a 50% increase in intensity for the highest voltage. Finally, the lattice tilt orthogonal to the incident beam can be calculated by following the center-of-mass of the diffraction peak orthogonal to the 2θ direction on the CCD detector. These lattice tilt maps shown in Fig. 5.8 reveal the degree of mosaicity in these regions as well as slight lattice rotations due to the applied electric field. The lattice tilt of the (002) planes of
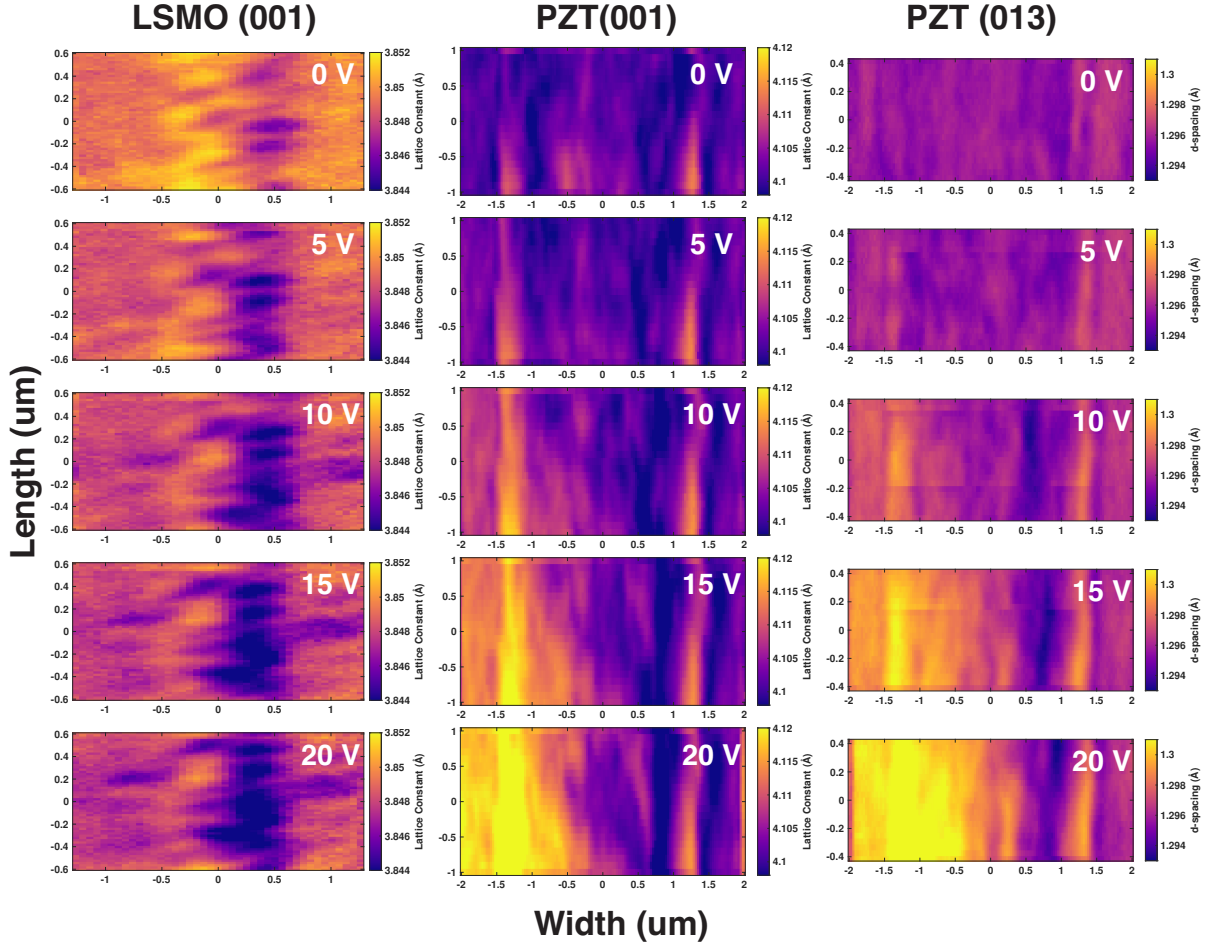
**Figure 5.4**: The c-axis lattice constant of both LSMO and PZT are calculated from the (002) diffraction peak signal while the spacing of the (013) lattice planes are shown for various applied voltages.

LSMO and PZT remain relatively static at all voltages, but the PZT (013) lattice planes appear to be more susceptible to the electric field as reflected by variations of lattice tilt in selective regions.

To demonstrate the large strain in PZT near the driving Au electrode was not due to imperfect sample growth (potentially poor contact of one of the electrodes), the direction of the electric field was reversed (denoted by the negative voltages). As seen in Fig. 5.9(a), the mirror reflection of the general asymmetric trend in the strain is seen when the direction of the applied electric field is reversed. The smallest strain is located right below the LSMO,
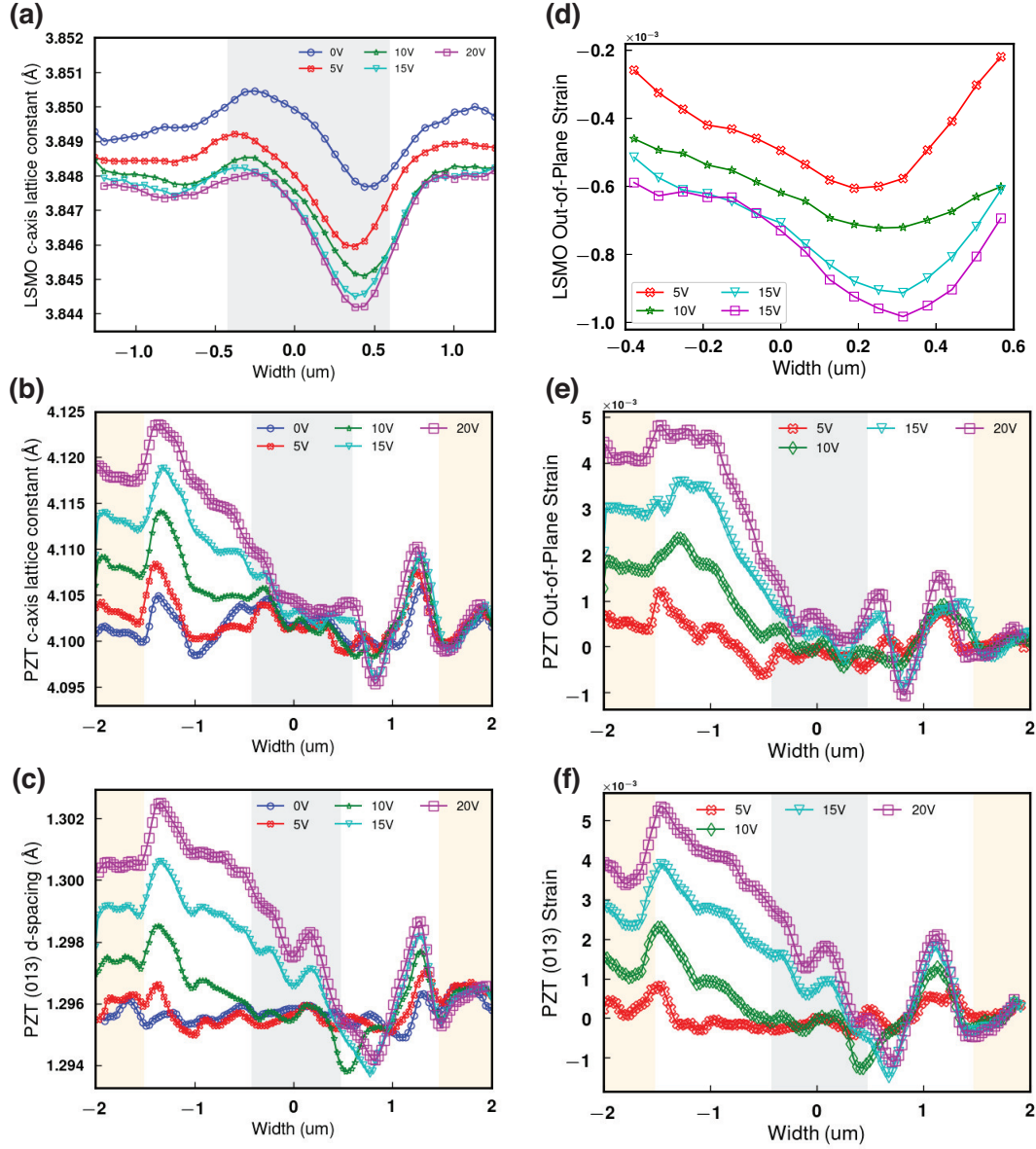
**Figure 5.5**: **(a,b,c)** By averaging the 2D maps of the lattice spacing along the length of the bar, the average lattice constant across the width of the bar of the LSMO and PZT c-axis as well as the lattice spacing of the PZT (013) lattice planes are calculated. **(d,e,f)** The average strain across the bar is calculated by using the 0 V scan as the reference.

though to conclusively determine whether LSMO is actively suppressing the strain state in that region requires the same nanodiffraction experiment without the LSMO bar. The average c-axis lattice constant of PZT for all voltages are also calculated for three different
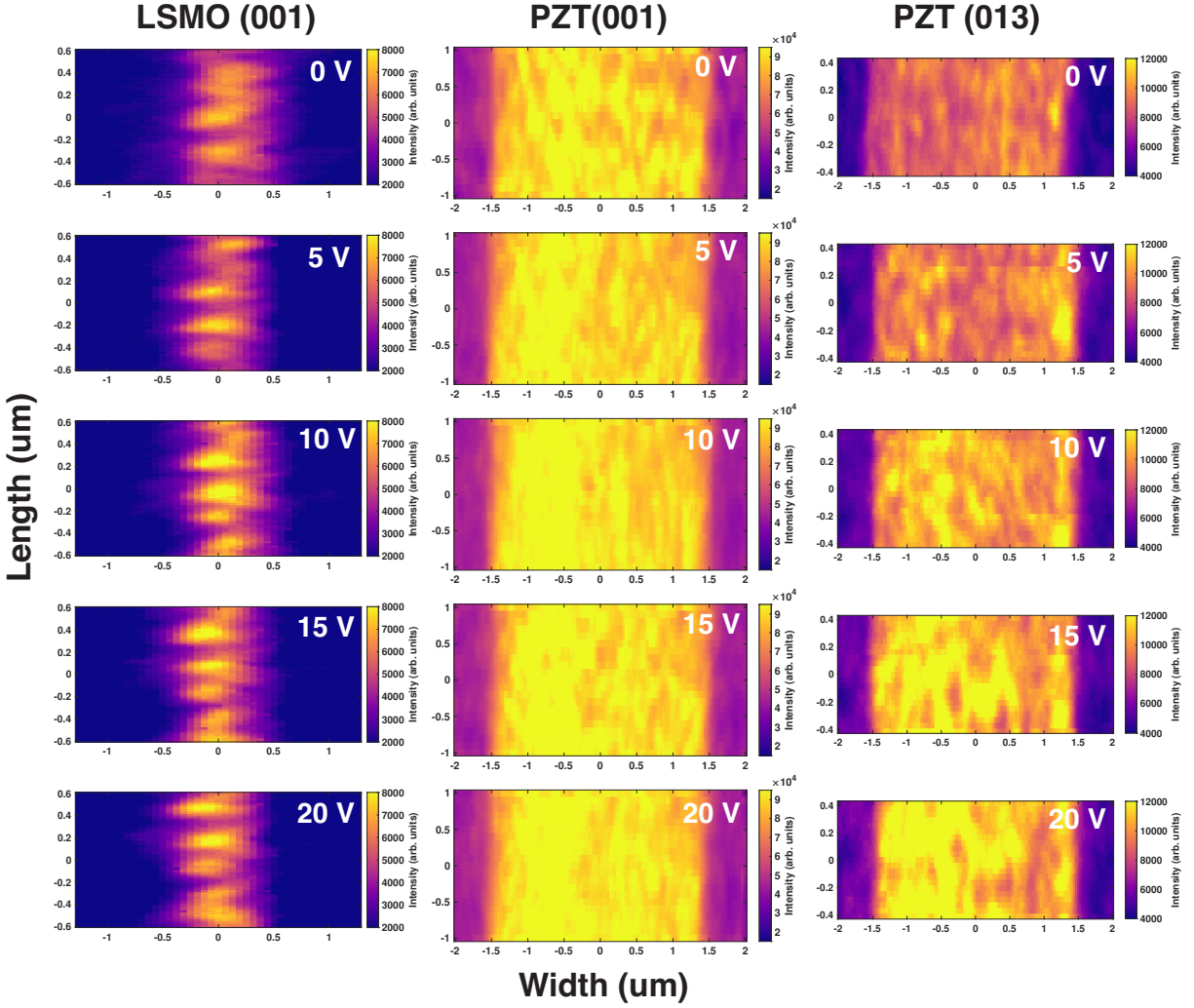
**Figure 5.6**: The integrated diffraction peak intensity of both LSMO and PZT are shown for various applied voltages.

regions: directly below the Au (the beige regions in Fig. 5.9(a)), directly below the LSMO (the gray region in Fig. 5.9(a)), and just PZT (the white regions in Fig.5.9(a)). In the clamped PZT geometry, the resulting strain from an applied voltage in PZT reveals the typical butterfly hysteresis loop, but the direction of electric field and strain are parallel. Here, Fig. 5.9(b) shows that under the LSMO region, the strain orthogonal to the electric field direction also follows a similiar butterfly hysteresis loop.
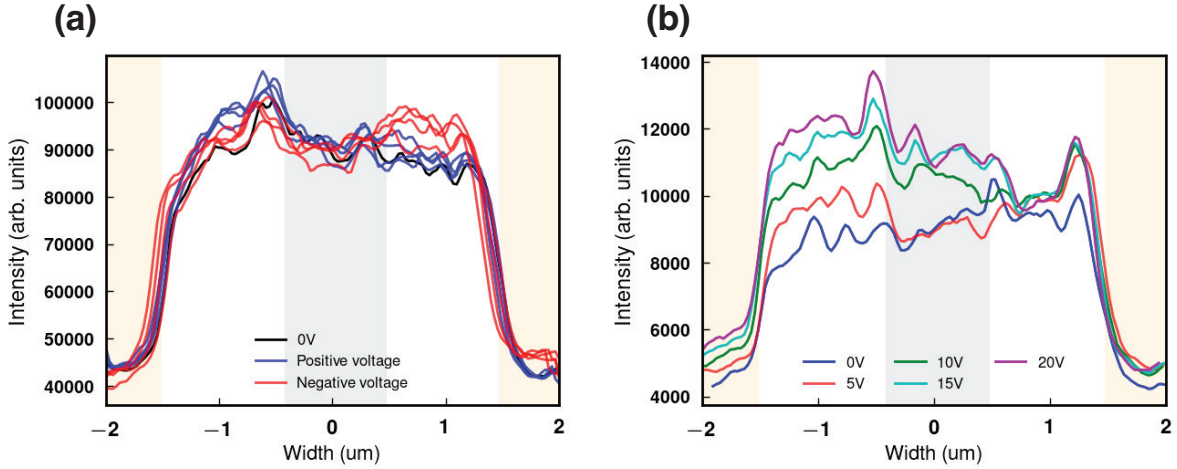
**Figure 5.7**: **(a)** The average integrated intensity of the PZT (002) Bragg peak across the device for positive and negative applied voltages. The Bragg peak has a slightly higher intensity near the driving electrode. **(b)** The average integrated intensity of the PZT (013) Bragg peak across the bar. In the region near the driving electrode, the intensity increases by as much as 50%.

$$\frac{1}{d^2} = \frac{h^2 + k^2}{a^2} + \frac{l^2}{c^2} \tag{5.1}$$

Finally, the b-axis lattice constant corresponding to the direction along the length of the device can also be calculated from the (002) and (013) lattice spacing. The relation between the d-spacing for lattice planes and the tetragonal lattice constants is given in Eq. 5.1. From the (002) diffraction maps, the c-axis lattice constant was extracted whereas the d-spacing corresponding to the $(h,k,l) = (013)$ lattice planes was directly measured from the (013) diffraction maps. Since there is a large difference in the incident angle for the (002) and (013) diffraction peaks, the area of the central region mapped is twice as large for the (002) peak. Furthermore, there is no feature between the two sets of maps (d-spacing, intensity, lattice tilt) that would allow us to accurately correlate the regions. Therefore, the b-axis lattice constant was calculated point by point from the average signals across the width of the device. Fig. 5.10(a) shows the calculated b-axis lattice constant and Fig. 5.10(b) shows the corresponding strain. The b-axis lattice constant at 0 V is approximately
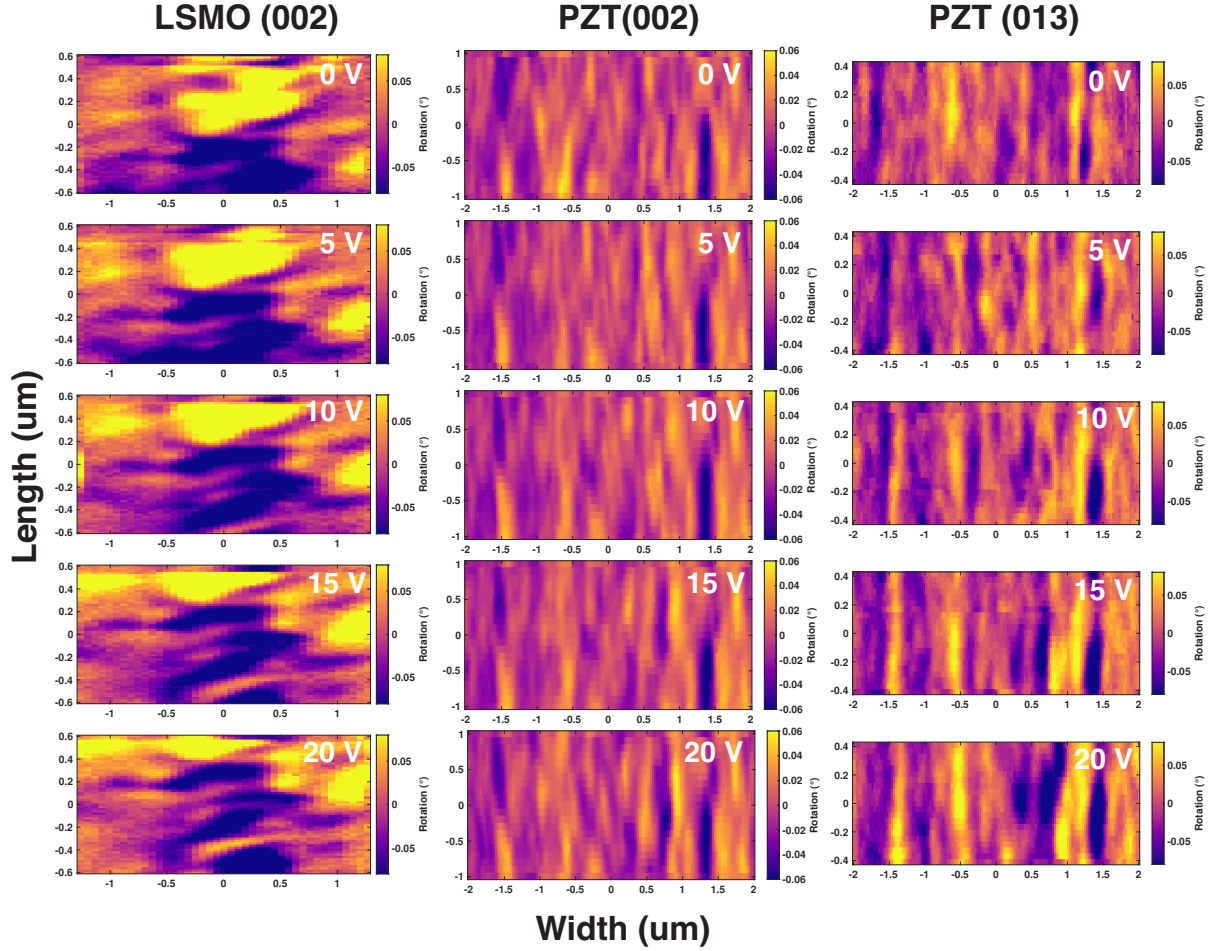
**Figure 5.8**: The lattice tilt of respective lattice planes in LSMO and PZT are shown for various applied voltages.

4.05 Å, which is in line with the expected values for the tetrahedral phase of PZT [77]. When a voltage is applied, the in-plane lattice constant remains relatively unchanged up to 10 V, but at the highest applied voltage of 20 V, an almost 2% strain is seen near the region below the LSMO.

## 5.6 Discussion and Conclusion

The results of the x-ray nanodiffraction experiment reveal the spatially-resolved, electrically-induced strain in both the PZT and LSMO layers. As demonstrated in the
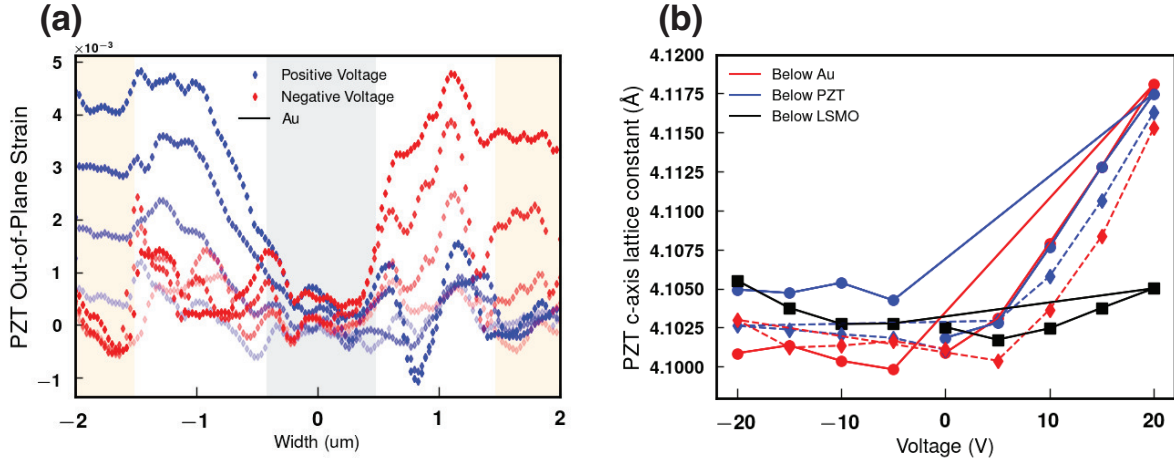
**Figure 5.9**: **(a)** The strain of the PZT (002) lattice planes for both polarizations of the applied in-plane electric field. Increasing opacity correspond to higher absolute values of the voltage. **(b)** The average c-axis lattice constant of PZT corresponding to the regions below Au, below LSMO, and just PZT are shown for all voltages.
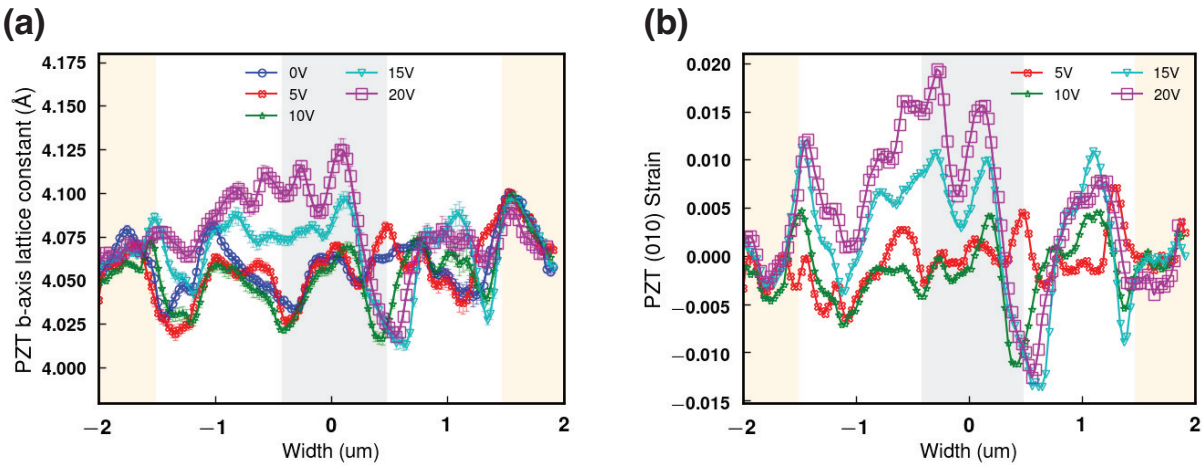


**Figure 5.10**: **(a)** The b-axis of PZT calculated from the c-axis lattice constant and the (013) d-spacing. **(b)** The in-plane strain of PZT along the length of the device is calculated by using the b-axis lattice constant at 0 V as reference. **(c)** The average integrated PZT (013) peak intensity across the bar. **(d)** The average integrated PZT (002) peak intensity across the bar.

2D maps, the system exhibits rich and surprising nanoscale features previously not seen in PZT, most notably the 2% strain along in the b-axis of the device, orthogonal to the applied electric field direction. The typically clamped PZT geometry where electrodes are placed on either side of the larger surface area shows strain on the order of $10^{-3}$ [78]

where the applied electric field drives the increase in polarization and strain along the same direction. In our device, the b and c axes are both orthogonal to the direction of the applied electric field. Based on the positive strain along the c-axis, the applied in-plane voltage does not appear to induce a $90°$ reorientation of the domains, but counterintuitively suggests an increase in the magnitude of the out-of-plane polarization. Even the region where PZT strains the least, under the LSMO, there is a small positive strain. This positive out-of-plane strain in PZT corresponding to a negative out-of-plane strain in LSMO also goes against the expected strain propagation across an interface. However, other possible interfacial effects such as the role of the in-plane strain, octahedral rotations and breathing modes may be the dominating mechanisms.

To determine the role of other possible mechanisms at play, we modeled the x-ray diffraction intensities for the (002) and the (013) peak. Introducing a breathing mode by varying the Ti-O bond length by as much as 5% leads to an increase in the (013) peak intensity and a decrease in the (002) peak intensity, but both by less than 0.5%. While this does not rule out the possibility of breathing modes in the system, breathing modes do not contribute to the large changes in the peak intensities. A displacement of the Pb (A-cation) along the (001) direction by 4% (shift of 0.16 Å) resulted in a 37% decrease in the (013) peak intensity but only a 13% decrease in the (002) peak intensity. These simulations suggest the largest contribution to the changes in peak intensity comes from the displacement of the Pb atom where the initial 0 V state consists of the displaced Pb atom while the applied voltage drives the Pb atom back into its tetragonal lattice position. The displacement mechanism alone would result in a slightly smaller increased (013) intensity than observed in our experiment, but the difference can be accounted for by taking the octahedral rotations into account. It is already well known that octahedral rotations of the oxygen anions exist in PZT and in many complex oxides of perovskite structure [79]. Based on our model, correcting for an upper limit of a 10 degree octahedral rotation ($a^-b^-c^-$ in

66

Glazer notation) leads to a 5% increase int he (013) peak intensity while maintaining a constant (002) peak intensity. Therefore, the observed variations in the peak intensities, particularly near the driving electrode, suggests the voltage corrects for the distortions originating from the octahedral rotation and Pb displacements in PZT.

Finally, the 2% increase of the in-plane strain is unheard of in PZT, and is considered extreme in many other material systems as well. Since the PZT is epitaxially coupled to the STO substrate, the PZT layer closer to the STO is likely less strained than near the surface, but this suggests the PZT near the surface would portrude on the ends by as much as 300 nm. The time limitation of the experiment from the scanning probe microscopy technique however also limits the scan region to the central 2 μm of the 30 μm device structure. It is very possible there are domains along the device on the micron lengthscale consisting of large positive and negative in-plane strain. The more probable explanation is the possibility of an electrically-induced structural phase transition from a tetragonal to either a rhombohedral or monoclinic lattice structure. The x=0.52 composition is right at the morphotropic phase boundary (MPB) between tetragonal and rhombohedral phases [80], and the b-axis lattice constant near the driving electrode is appoximately the same as the c-axis lattice constant. There is also evidence to suggest that a monoclinic phase exists at this boundary as well where an application of an electric field increases the monoclinic phase fraction [81, 82]. However, without measuring the PZT a-axis strain, it is not possible to differentiate between the two structures.

In summary, the x-ray nanodiffraction experiment revealed electrically-induced strain, cation displacements and octahedral rotations that were more strongly affected near the driving electrode. The localized effects and hysteretic behavior opens the possibility to tune the material property of freestanding PZT device structures for applications.

## 5.7 Acknowledgements

# Chapter 6

# Nanoscale Resolution of Strain Fields in Highly Spin Polarized LSMO Nanoislands

## 6.1  Introduction

Nanomaterials can sustain higher strain rates than their bulk counterparts, and this strain rate is dependent upon the growth methods applied in the fabrication process. For the case of magnetic nanomaterials, a typical synthesis process of well-ordered magnetic nanostructures resorted to selective etching or electroplating of the film [83, 84]. However, these methods lacked long-range order and control of the position of magnetic nanostructures [74]. A new fabrication method that makes use of ion implantation renders etching unnecessary as the ions cause a structural distortion that changes the magnetic properties of the film [74]. This ion implantation method has been applied specifically to $La_{0.7}Sr_{0.3}MnO_3$ (LSMO), which is a soft ferromagnetic metal with highly tunable properties that can be exploited to control spin textures and magnetic behavior in patterned structures. The

ability to manipulate the topological spin textures has recently become the standard for developing spin-based memory devices, which makes LSMO an attractive material for investigation [85, 86, 87]. Furthermore, doped rare-earth manganites have been shown to have a high degree of spin-polarization and exhibit colossal magnetoresistance (CMR), making them attractive for applications in general memory and sensory applications [88]. In addition, with a variety of ground states due to competing degrees of freedom and the interplay between charge, spin, orbital and lattice order, these materials are an active ground to study fundamentals of correlated systems.

This novel structuring technique that uses $Ar^+$ implantation to control local magnetic ordering has been employed to fabricate highly spin polarized LSMO nanoislands on STO [75, 74, 89]. Using the PEEM-3 microscope at the Advanced Light Source, the x-ray magnetic circular dichroism shows that the ion-implanted regions have no AFM domain contrast, which means $Ar^+$ can be used to locally suppress magnetic ordering. The distortion in the lattice structure due to the ion implantation also induces an epitaxial strain state along the vertical interfaces of the LSMO nanoislands and the matrix that competes with the strain imposed by the $SrTiO_3$ (STO) substrate. The flux-closure domains that form within these nanoislands suggest the shape anisotropy dominates over the substrate-induced strain, but to unequivocally understand the origin of the domain patterns is dependent on understanding the competing effects of magnetization history, film thickness, and lattice structure. Here we use x-ray nanodiffraction to spatially resolve the strain field to find correlations to the magnetic domain patterns and aid future defect engineering in memory and sensory devices [88, 75].
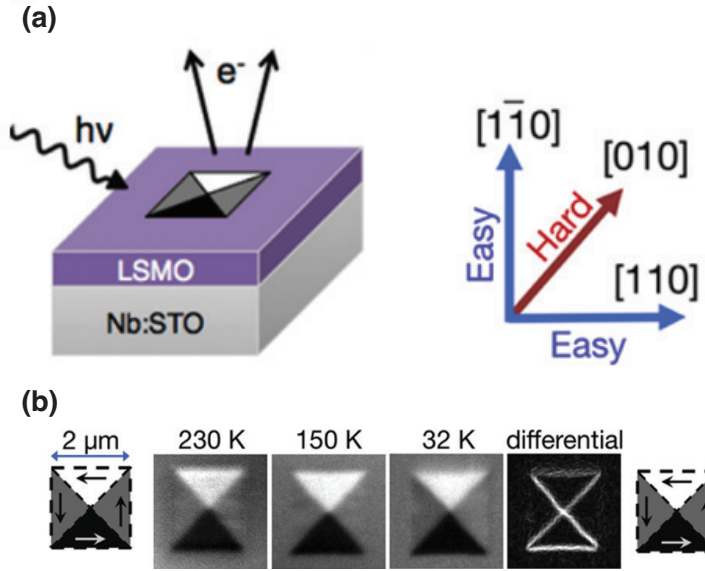
**Figure 6.1**: **(a)** Schematic of the X-PEEM experiment where x-rays tuned to the Mn $L_2$ and $L_3$ edges with right circular and left circular polarizations lead to photoemitted electrons [89]. **(b)** By taking the difference of the right and left circular polarized signals, the spatially resolved magnetic domain contrast can be seen. Here, the contrast along with the magnetic polarization vectors for the square nanoisland is shown [74].

## 6.2   Experimental Setup

The samples were fabricated by the Takamura group at the University of California Davis. LSMO films were grown on (001) and (110) STO substrates by pulsed laser deposition with a KrF laser. Subsequently, a double layer mask of 20 nm polymethyl methacrylate (PMMA) and 400 nm of hydrogen silsequioxane (HSQ) was spin coated and patterned using electron beam lithography. The mask pattern consists of square, diamond, and circular islands distributed at various densities on the substrate. Finally, the nonmasked areas were subjected to $Ar^+$ ion implanation [74]. The magnetic domain pattern of the square nanoislands from the X-ray photoemission electron microscopy (X-PEEM) experiment is shown in Fig. 6.1 where flux-closure domains determined by the shape anisotropy is clearly seen.

The subsequent nanodiffraction experiment carried out by the dissertation author

is aimed at spatially resolving the strain field of the square nanoislands, specifically the ones with a lateral dimension of 2 µm and a thickness of 40 nm, as depicted in Fig. 6.1(b). The experiment was carried out at the Hard X-ray Nanoprobe beamline at the Center of Nanoscale Materials of Argonne National Laboratory where a diffractive nanoprobe setup, schematically shown in Fig. 2.7, is used. With this type of setup, the Fresnel zone plate (FZP) focuses the beam to a spot size of approximately 25 nm at the sample with a set of incoming wavevectors that span about $0.3°$ in the incident angle. The resulting diffraction pattern seen at the detector with the FZP imprint is a unique signal containing information about the strain and lattice rotations coming from the sample. Fig. 6.2(a) shows an example of how strain and tilted lattice planes result in two unique diffraction patterns compared to the unstrained case, and it is possible to disentangle the independent signals with proper analysis that is detailed in the subsequent section.

Unlike X-PEEM that is a single-shot full-field microscopy technique, x-ray nanodiffraction relies on raster scanning an x-ray beam across the sample while recording the diffraction pattern at each point. The sample was located 1 m from a 516 x 516 pixel CCD detector with 55 µm pixel resolution. The LSMO (002) peak was aligned in symmetric scattering geometry with an incident angle of $18.7°$. The focal length of the FZP distance from the sample was optimized by scanning the beam across the edge of a nanoisland while monitoring how sharp the integrated (002) diffraction peak falls as a function of scan steps to acquire a beam spot size of 25 µm. Given these parameters, a strain down to $10^{-4}$ is possible to detect. A schematic of the scattering geometry and location of the CCD detector is shown in Fig. 6.3 where two different coordinate systems are used to describe the detector and sample location. Raster scans covering the extent of the 2 µm LSMO nanoisland was performed at 293 K, at 293 K with an out-of-plane magnetic field of 0.3 T, and at 175 K with an out-of-plane magnetic field of 0.3 T.
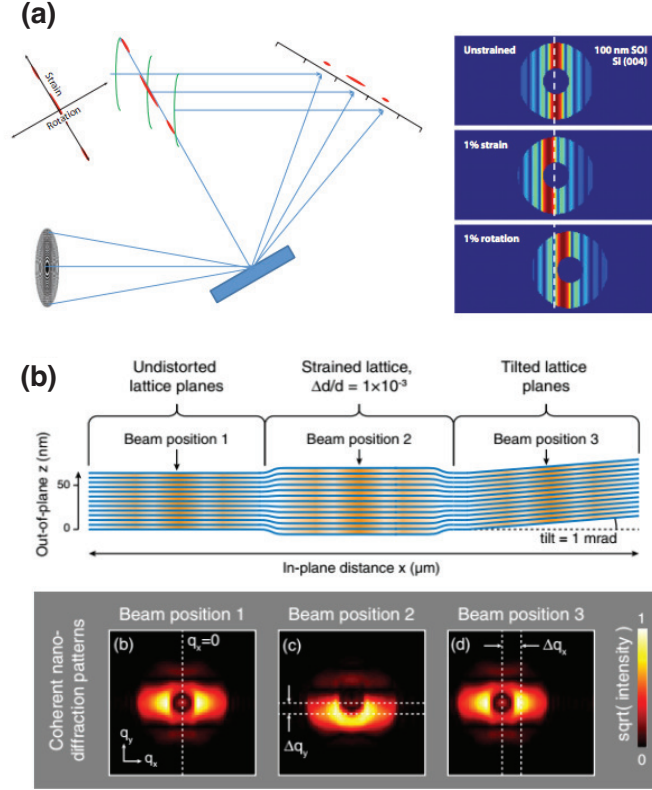
**Figure 6.2**: **(a)** The Fresnel zone plate focuses the beam at the sample and the scattered signal is recorded on a CCD detector. Since the diffractive optics consists of a range of wavevectors, the signal on the detector contains information about the lattice spacing as well as any lattice rotation (degree of tilt from moasic blocks). A simulated signal of completely unstained, a 1% strain, and a 1% rotation of the CCD detector is shown on the right [26]. **(b)** Another example of how a strained lattice and tilted lattice planes show up in the diffraction pattern [90].

## 6.3   Analytical Method

In the experimental setup depicted in Fig. 6.3, the x-axis of the CCD detector covers a small range of $2\theta$ positions. Any strain in the LSMO nanoisland OR any lattice tilt along the beam axis will shift the diffraction pattern along the x-axis of the CCD detector. Typically, rocking curves with at least three $\theta$ positions are necessary to average out the lattice tilt in order to extract the strain. In this experiment, the diffraction pattern produced from diffractive optics contains the outline of the FZP that is capable of resolving the strain from the lattice tilt without the need to perform rocking curves. As shown

73
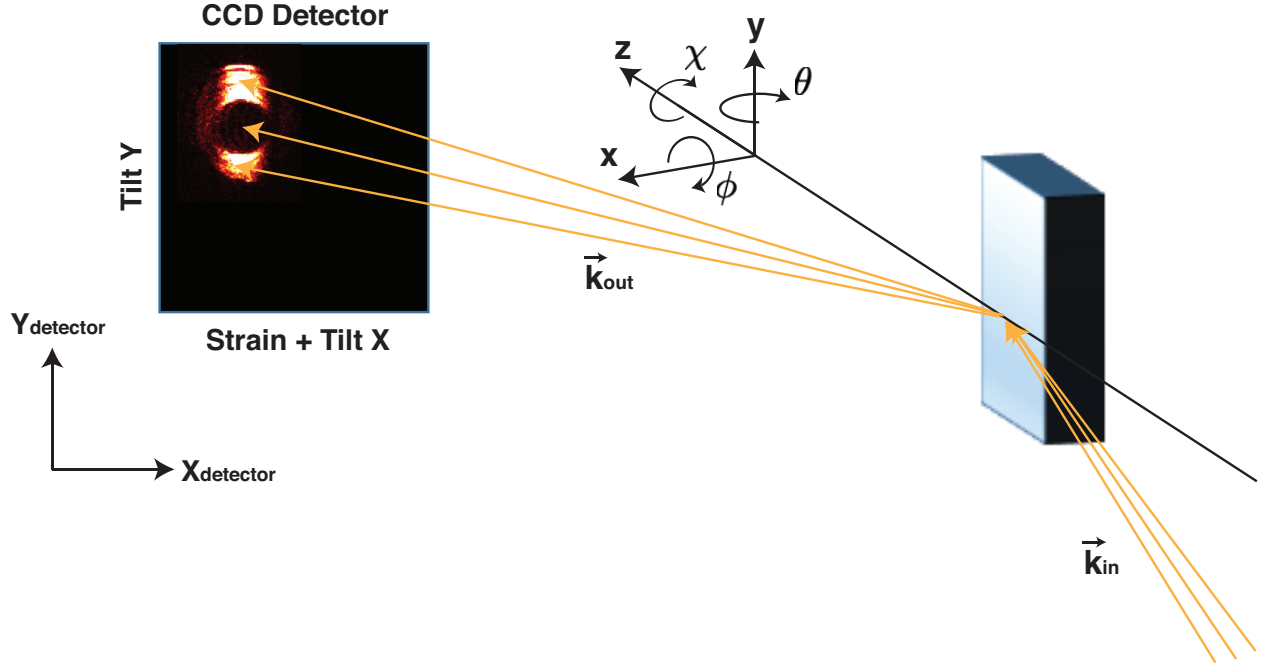
**Figure 6.3**: Two reference frames, one for the CCD detector and one for the sample, are used to describe the geometry of the experiment. Here the diffraction pattern projected along the x-direction of the detector contains information about the out-of-plane strain and any lattice rotation about the y-axis of the sample. The diffraction pattern projected along the y-direction of the detector contains information about the lattice rotation about the x-axis of the sample.

in Fig. 6.2(a), the strain and tilted lattice planes show up in orthogonal directions in reciprocal space, and the slice through the Bragg peak by the CCD detector in reciprocal space records the projection of both the strain and lattice tilt.

The strain and lattice tilt can be extracted from the experimental data using a simulation method. Given the parameters of the experiment, including the dimensions of the FZP, it is possible to map how the initial wavevectors, $\vec{k}_{in}$, scatters off a set of lattice planes and onto the CCD detector. The set of known experimental parameters is given in Table 6.1 where the matrix of initial wavevectors is used to calculate the q-dependent thin film Patterson function. Fig. 6.4(a) shows an experimental detector image of the LSMO (002) peak whereas Fig. 6.4(b,c) show the simulated diffraction patterns of an unstrained and a strained LSMO thin film. The sharp STO (002) peak on the detector corresponds

| Experimental Parameters | Varied Parameters |
|---|---|
| θ | ✓ |
| χ | ✓ |
| φ | — |
| R (sample-to-detector distance) | — |
| δ ($Y_{detector}$) | — |
| 2θ ($X_{detector}$) | — |
| d-spacing | ✓ |
| Intensity | ✓ |
| Sample thickness | — |

**Table 6.1**: The experimental parameters used to simulate the initial diffraction pattern and the parameters to vary in an optimization algorithm to determine the strain and lattice tilt.

to a well-defined lattice constant of 3.90 Å and is used to calibrate the lattice spacing of LSMO. Otherwise, it is masked out when performing the analysis.

The analysis can be carried out by comparing the experimental detector image with the simulated image. This is quantified by looking at the residual intensity, i.e. the quantity we want to minimize is given by $\delta|I_{exp}(x,y) - I_{sim}(x,y)|^2$. Throughout the raster scan, certain experimental parameters such as the sample-to-detector distance and the location of the CCD detector (given by δ for the vertical direction and 2θ is for the horizontal direction) are fixed. However, at each point of the scan, the intensity, strain, and lattice tilt can vary. Therefore, a nonlinear optimization algorithm is used where these aforementioned parameters are varied until the residual is minimized. Looking at the experimental geometry in Fig. 6.3, the lattice tilt in the two orthogonal basis vectors can be artificially produced by rotations in θ (corresponding to a shift of the diffraction pattern along the x-axis of the detector) and in χ (corresponding to shift in the diffraction pattern along the y-axis of the detector). To retrieve the degree of lattice tilt at each spatial point of the nanoisland, θ and χ are therefore varied as well.
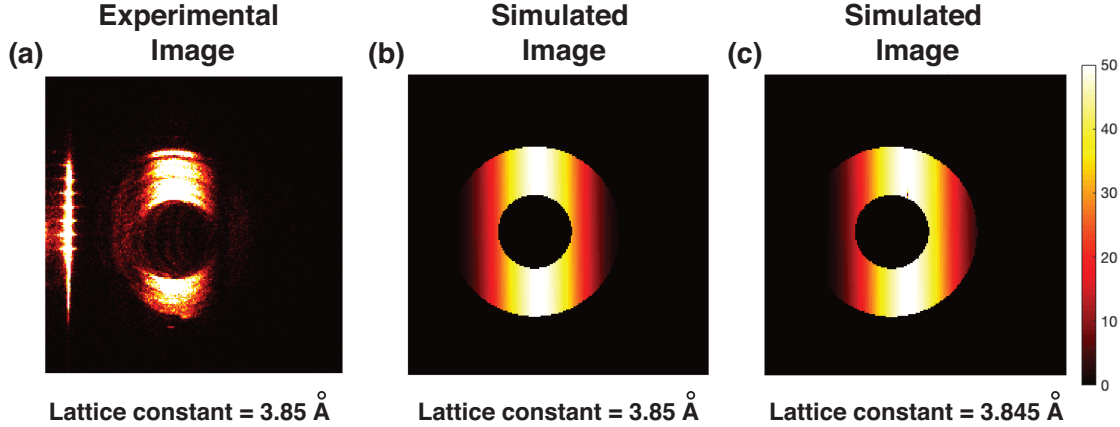
**Figure 6.4**: **(a)** Cropped section of the CCD detector where the sharp STO (002) subtrate peak is on the left and the LSMO (002) diffraction peak is on the right. The substrate peak corresponds to 3.90 Å and is used to calibrate the lattice spacing of LSMO. **(b)** A simulated diffraction pattern of a 40 nm unstrained LSMO (002) peak. **(c)** A simulated diffraction pattern of a 40 nm strained LSMO (002) peak with a lattice constand of 3.845 Å.

## 6.4   Results and Conclusions

The results of the analysis showing the spatially resolved strain and lattice tilts as a function of temperature and magnetic field are shown in Fig. 6.5. The same 2 µm nanoisland within the array was used for all scans. As seen in the top row of Fig. 6.5, unique features of the spatially-resolved lattice spacing is seen in all three scans, which is both a good fiducial to demonstrate reproducibility of the technique as well as revealing the nanoscale heterogeneity present within the nanoisland. Evidently, introducing a 0.3 T out-of-plane magnetic field induces magnetostriction where the out-of-plane lattice constant contracts quite uniformly throughout the nanoisland, corresponding to an average strain of $1.3 \times 10^{-4}$. However, as the system is placed in a low-temperature (175 K) environment, the average lattice spacing over the nanoisland does not change, but the gradients between regions of slightly different lattice spacings are sharper, as seen in the top row of Fig.

6.5. Comparing the lattice spacing maps to the magnetic domains revealed by X-PEEM, there appears to be no correlation between the out-of-plane strain state with the magnetic domains.
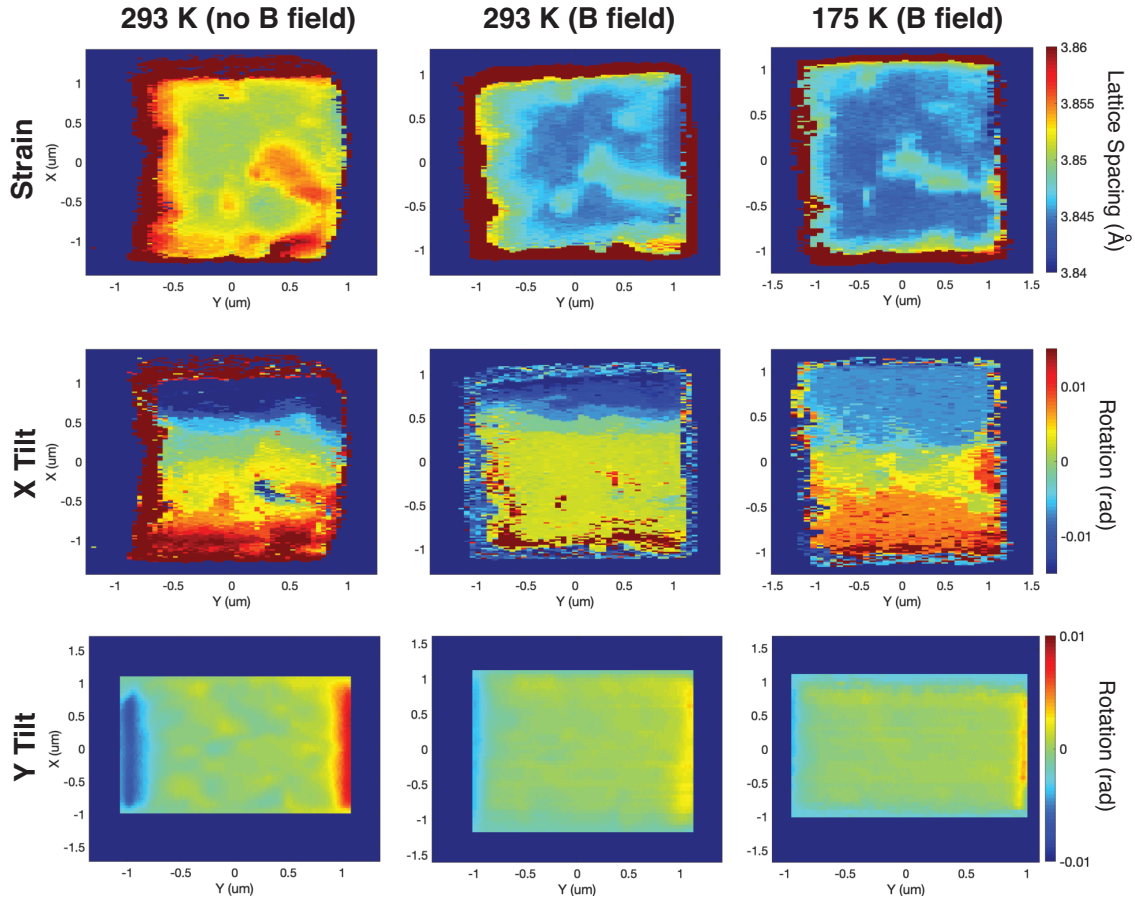


**Figure 6.5**: 2D maps of the lattice constant, lattice tilt in the x-direction, and the lattice tilt in the y-direction at 293 K, at 293 K with a 0.3 T out-of-plane magnetic field, and at 175 K with a 0.3 T out-of-plane magnetic field.

The lattice tilt in the x-direction calculated from the analytical method described in Section 6.3 show sharp rotations near the edges that extend well into the nanoisland. Accompaning the strain when a magnetic field is applied, the initial tilt at the lower edge of the nanoisland flattens out, but the top edge of the nanoisland remains tilted. Finally, at low temperatures, there is no change in the average lattice constant of the nanoisland, but the tilt of the lattice planes resembles the case at room temperature without an applied

magnetic field, though to a lesser degree. The 2D map of the x-direction lattice tilt at low temperatures with an applied magnetic field resembles the magnetic domain pattern revealed by X-PEEM. Based on the symmetry of the nanoisland, the lattice tilt in the y-direction is expected to behave similarly, but the 2D maps here show very little variation across the nanoisland. However, since there is no strain information contained along the y-direction of the CCD detector, the lattice tilt in this direction was calculated from the center-of-mass of the diffraction peak.

Based on the results, there is no clear indication that magnetic domains are correlated with the out-of-plane strain state, or rather the strain is not the dominating mechanism driving the formation of the flux-closure domains. The initial lattice tilt near the edges of the nanoisland is most likely due to the chemical etching process during the fabrication stage, but does show a dynamic response when a magnetic field is applied at lower temperatures, but the only in one direction. There is no indication why this asymmetry arises except for the analytical methods used to extract the degree of lattice rotation. Therefore, it is possible further refinements of the analysis method is needed to either more accurately extract the lattice tilt in both directions or to quantify the error.

## 6.5    Acknowledgements

# Chapter 7

# Extracting Contrast in an X-Ray Speckle Visibility Spectroscopy (XSVS) Experiment under Imperfect Conditions

Pump-probe experiments at synchrotrons and free electron lasers to study ultrafast dynamics in materials far from equilibrium have been well established, but techniques to investigate equilibrium dynamics on the nano- and pico- second timescales remain underdeveloped and experimentally challenging. A promising approach relies on a double probe x-ray speckle visibility spectroscopy setup at split-and-delay beamlines of x-ray free electron lasers. However, the logistics in consistently producing two colinear, perfectly overlapping pulses necessary to conduct a faithful experiment is difficult to achieve. In this paper, a method is introduced to extract contrast in the case where an angular misalignment and imperfect overlap exists between the two pulses. Numerical simulations of a dynamical system show that contrast can still be extracted for significant angular misalignments

accompanied by partial overlap between the two pulses.

## 7.1    Introduction to XSVS

X-ray photon correlation spectroscopy (XPCS) is a powerful coherent x-ray technique capable of probing the nanoscale dynamics for a wide range of material systems [21, 51, 91, 20, 92]. When a coherent beam interacts with the atomic or electronic structure, the interference creates a speckle pattern in the far field that is a signature of the nanoscale heterogeneities present in the system. By measuring how fast or slow the speckle pattern evolves, it is possible to resolve and quantify the fluctuation timescale of the order parameter. This can be achieved by measuring the time-averaged intensity-intensity autocorrelation function between detector images that are separated by a delay time, $\tau$, as defined in Eq. 7.1.

$$g_2(\mathbf{q},t) = \frac{\langle I(\mathbf{q},t)I(\mathbf{q},t+\tau)\rangle_t}{\langle I(\mathbf{q})\rangle^2}. \tag{7.1}$$

Here $g_2(\mathbf{q},t)$ is a correlation function, $\mathbf{q}$ is the x-ray scattering vector, $t$ and $\tau$ are time variables, and the angular brackets denote averaging over the time $\tau$. The decay rate of the correlation function $g_2(\mathbf{q},t)$ gives one the characteristic timescale of dynamics present in the system [93, 94]. However, this approach based on the evaluation of the g2-function has an inherent limitation in the temporal resolution that is defined by the framerate of the detector, which is presently on the order of milli- to micro- seconds for the fastest CCD and photon-counting area detectors [95, 96].

With the advent of split-and-delay lines at x-ray free electron lasers (XFELs) [97, 98, 99, 100], it is now possible to circumvent this limitation with a modified technique known as x-ray speckle visibility spectroscopy (XSVS) that is capable of probing ultrafast dynamics such as atomic diffusion and skyrmion lattice phases [101, 102]. Instead of relying

on several detector images, XSVS exploits a single speckle pattern on the detector generated by either one or several x-ray pulses. XSVS has already been successfully employed using a single x-ray pulse with variable duration, in other words, a single coherent XFEL pulse [101]. If the system is static or the dynamical timescale is longer than the pulse duration, then the speckle pattern on the detector will have a relatively high contrast value defined by the temporal and spatial coherence of the beam. However, if the system exhibits dynamics within the pulse duration, the speckle pattern on the detector smears out, resulting in a lower contrast value than its corresponding static case. This decay of the speckle contrast, defined as $\beta(t)$ in an XSVS experiment, provides a timescale for the dynamics in the system. Therefore, by varying the pulse duration, it is possible to probe dynamics by examining the change in contrast. For example, a coherent pulse varied between 10 fs and 120 fs was used to measure caging effects of ultrafast water dynamics [103]. The disadvantage with the single pulse method is the limitation of the largest time delay that is defined by the sub-picosecond pulse duration.

A second method of XSVS that is capable of probing a wider range of timescales uses two identical coherent pulses that are separated by a delay time as shown in Fig. 7.1(a). The experimental setup in this case uses optics in a split-and-delay line to separate a coherent pulse into two identical probes, delaying one of the probes in time, and recombining them into two colinear signals [104]. In practice, this is extremely difficult to achieve consistently [105] and there will often be an angular misalignment between the two pulses and a nonperfect overlap on the sample as illustrated in Fig. 7.1(b). In both cases, the speckle contrast is affected in a double probe XSVS experiment where the detector records the sum of two speckle patterns. Using numerical simulations, we show how the angular misalignment and nonperfect overlap affects the speckle contrast, and how it is possible to recover the contrast lost through selective binning of the detector data.
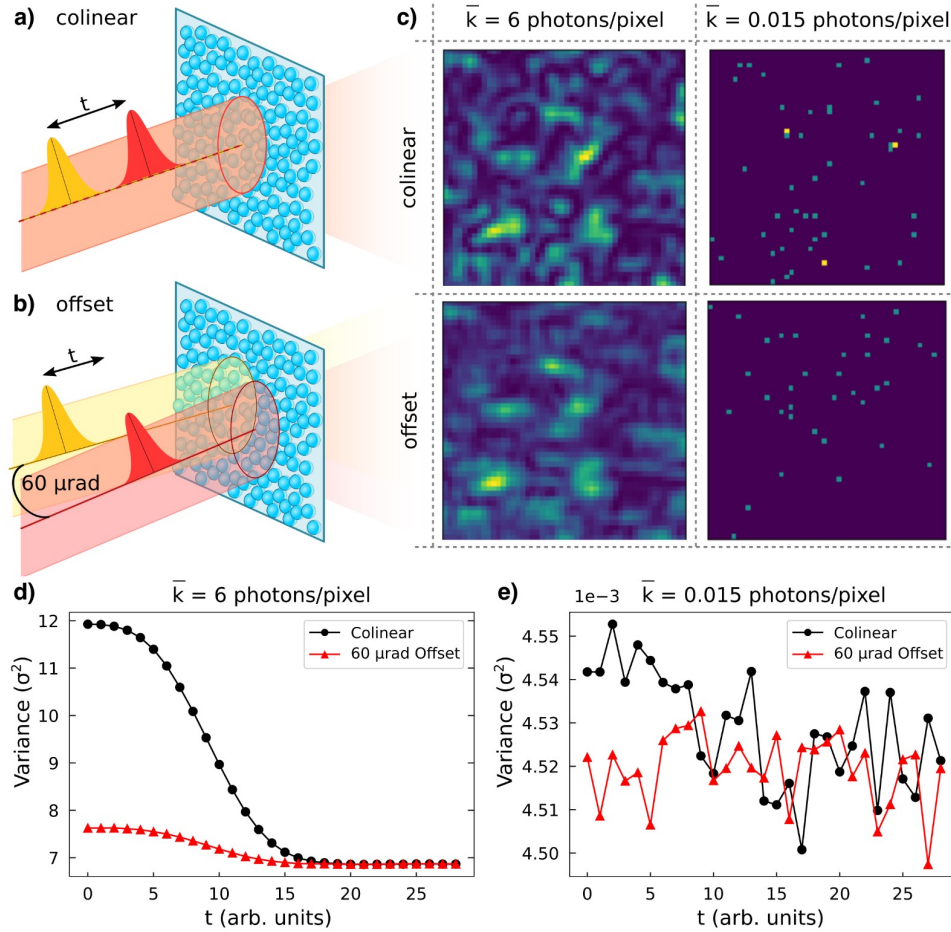
**Figure 7.1**: Schematic for an XSVS experiment where the two pulses are colinear and perfectly overlapping **(a)** and where the two pulses have an angular mismatch and imperfect overlap **(b)**. **(c)** The corresponding detector images for the two cases **(a)** and **(b)** for a high photon count regime (left column) and low photon count regime (right column) where Poisson noise is significant. The contrast as measured by the variance for the high photon count regime **(d)** and for the low photon count regime **(e)**.

## 7.2 Extracting Contrast

The contrast $\beta$ for a speckle pattern on an area detector is defined in Eq. 7.2 as:

$$\sigma^2(\mathbf{q}) = \beta(\mathbf{q}) + \frac{1}{\overline{k}(\mathbf{q})}, \tag{7.2}$$

where $\overline{k}$ is the average photon count per pixel corresponding to the scattering vector $\mathbf{q}$, and $\sigma^2$ is the normalized variance of the photon count [106]. In the high photon count regime where $\overline{k}$ is large, it is possible to measure the decay of contrast by simply tracking the variance of the speckle pattern since the last term in Eq. 7.2 is small compared to $\beta$. In the low photon count regime where $\overline{k}$ is small, the last term becomes significant and the variance can no longer accurately capture the contrast. This is demonstrated in Fig. 7.1(d,e) where the decay of contrast using the variance is evident in the system where $\overline{k} = 6$ photons/pixel but fails for the case of $\overline{k} = 0.015$ photons/pixel. This becomes problematic for a XSVS experiment since the typical signal produced from the interaction of a single or double pulse with a system, especially at large q values, is quite low [105]. To overcome this impediment, we have to resort to photon counting statistics and measure the contrast in terms of coherent modes, $M$, where $\beta = 1/M$. The value of $M$ represents the number of independent speckle patterns recorded by the detector.

Here we consider a speckle pattern with $M$ coherent modes where the intensity distribution is well approximated by a gamma density function, and where the discretized photon counts on the detector follows a Poisson distribution. The signal on the detector follows the compound distribution of these two independent probability distributions, which is the negative-binomial distribution, P(K), as given in Eq 7.3:

$$P(K) = \frac{\Gamma(K+M)}{\Gamma(M)\Gamma(K+1)} \left(1 + \frac{M}{\overline{k}}\right)^{-k} \left(1 + \frac{\overline{k}}{M}\right)^{-M}, \tag{7.3}$$

where $M$ is the speckle degree of freedom, $P(K)$ is the probability of finding $K$ photon

hits, and $\overline{k}$ is the average photon per pixel of the entire detector. In a real experiment, a proper droplet algorithm must be applied to convert the area detector signal into localized and discretized photon counts. In our simulations, this is achieved by feeding the final speckle pattern on the detector, characterized by the gamma distribution of the speckle intensity, through a Poisson filter. By counting the double K=2 and triple K=3 photon hits on the detector, it is possible to extract the contrast by fitting M to the P(K=2) and P(K=3) cases of the negative binomial distribution in Eq. 7.3.

## 7.3   Simulations

Speckle patterns are simulated following the example presented in [107]. A random phasor field $\phi(q_x, q_y)$ is created on a 1024 x 1024 grid, and a Gaussian beam $G_1(x, y) = A \cdot \exp\left[-\dfrac{x^2 + y^2}{2\sigma^2}\right]$ with a full width at half maximum (FWHM) profile of 235 pixels is centered on the middle of the grid at $(x_1, y_1) = $ (512, 512). The intensity of the speckle pattern produced on a 1024 x 1024 pixel area detector in the far field can be calculated using discrete Fourier transforms described in Eq. 7.4.

$$I(q_x, q_y) = \left|\mathcal{F}^{-1}\left[G_1(x - x_1, y - y_1)\mathcal{F}\left[e^{i\phi(q_x, q_y)}\right]\right]\right|^2 \tag{7.4}$$

Here $\mathcal{F}$ and $\mathcal{F}^{-1}$ denote the direct and inverse Fourier transforms, respectively. A dynamic system can then be created using a predefined correlation timescale [108]. In this approach, the random phasor field $\phi(q_x, q_y, t)$ is iteratively evolving in time as described by

$$\phi(q_x, q_y, t + dt) = \phi(q_x, q_y, t) + D(q_x, q_y, t) \cdot \sqrt{\ln[c(t)] - \ln[c(t + dt)]}, \tag{7.5}$$

where $D(q_x, q_y, t)$ is a Gaussian distribution with zero mean and unitary standard deviation to confine the magnitude of change to the phase field, and $dt$ is the time step between

two consecutively generated speckle patterns. In (Federico, 2006), the authors showed the standard deviation between successive phase fields, $\phi(q_x, q_y, t)$ and $\phi(q_x, q_y, t+dt)$, is related to the correlation function by $\sqrt{\ln[c(t)] - \ln[c(t+dt)]}$. The dynamics of the system is thus encoded in the time-dependent correlation function, $c(t)$, which describes how fast the correlation between speckle patterns decay with time. A monotonic function, $c(t) = \exp(-(t/t_c)^2)$ was chosen to simulate a dynamical system where $t$ is an arbitrary unit of time and $t_c$ is a time constant set to 200 to describe the temporal evolution. The final speckle pattern of a dynamic system in a double probe XSVS experiment with colinear pulses is therefore:

$$I(q_x, q_y) = \left| \mathcal{F}^{-1}\left[ G_1(x - x_1, y - y_1)\mathcal{F}\left[ e^{i\phi(q_x, q_y, 0)} \right] \right] \right|^2 + \left| \mathcal{F}^{-1}\left[ G_2(x - x_2, y - y_2)\mathcal{F}\left[ e^{i\phi(q_x, q_y, t)} \right] \right] \right|^2,$$

$$(7.6)$$

where $t$ is the time delay between the two pulses and $G_1(x, y) = G_2(x, y)$ for overlapping, colinear pulses. To simulate a partial overlap between the two pulses, the center of the second pulse is simply shifted to a different point $(x_2, y_2)$. An example of detector images for a high and low $\overline{k}$ value at $t = 0$ for this case is shown in Fig. 7.1(c).

To simulate an angular mismatch $\Delta\theta$ along the x-direction to the second pulse, we introduce a phase shift to the second Gaussian beam so that the illumination function $G_2(x, y)$ can be written as

$$G_2(x - x_2, y - y_2) = A \cdot \exp\left[ -\frac{(x - x_2)^2 + (y - y_2)^2)}{2\sigma^2} \right] \cdot \exp\left[ i\Delta q_x \cdot x \cdot s \right]. \qquad (7.7)$$

Here $\Delta q_x = q \cdot \Delta\theta$ for a small angular mismatch $\Delta\theta$ between the propagation directions of the two pulses where $q = 2\pi/\lambda$ is the wavevector of photons with wavelength $\lambda$, $x$ is the index of the pixels, and $s$ is the size of the pixel in real space. We chose an energy of

10 keV and set the size of a pixel to $s = 6.38$ nm/pixel to give a realistic FWHM of the Gaussian beam to be 1.5 µm (235 pixels). The parameters for our simulation produced an average speckle size on the detector of approximately 2 pixels as calculated from fitting a Gaussian to the normalized 2D autocorrelation of a detector image at time zero. In any real experiment, the speckle size is determined by the wavelength, the spot size of the coherent pulse, and the sample-to-detector distance and should be calibrated so that the average speckle size is at least 1-pixel size. Typically this is achieved by changing the sample-to-detector distance, but this parameter is fixed in our system due to the use of discrete Fourier transforms to simulate the speckle pattern on the detector instead of using a continuous Fourier transform. To model a low photon count regime, the amplitude of the Gaussian pulses, $A$, was defined so that the final detector images have an average photon count between $\overline{k} = 0.014$-$0.015$ photons/pixel within approximately two standard deviations. To account for the statistical nature of the photon detecting process, 50 independent phasor fields $\phi(q_x, q_y)$ were simulated and advanced for a total of 30 time steps.

## 7.4   Results

### 7.4.1   Angular Misalignment

A perfectly overlapping, but slightly misaligned second pulse effectively shifts the second signal along the detector to create a smeared speckle pattern as demonstrated in Fig. 7.1(c) (left column) for the high photon regime where the second pulse is misaligned by 60 µrad. Note that such smearing is not visually evident for low photon counts where the Poisson fluctuations are on the order of the signal itself, as shown in Fig. 7.1(c) (right column). To compare the difference in contrast between the colinear and misaligned cases, we first calculate the number of K=2 photoevents relative to the average intensity $\overline{k}$ at time zero where the system is static, and compare the results to the probability distribution

87

for full contrast P(K=2, M=1) and zero contrast P(K = 2, M $\to \infty$). In Fig. 7.2(a), we can immediately see the probability P(K=2) for the misaligned case is lower than for the colinear one, which means the decrease of the contrast is caused by the angular misalignment. The two probes are fully coherent in our simulation and therefore, the theoretical maximum contrast is 1 for a completely static system where there is only a single speckle degree of freedom (M=1), and $\frac{1}{2}$ for a completed decorrelated system with 2 speckle degrees of freedom (M=2) coming from the interaction of 2 pulses with different phasor fields. At each time delay, the speckle contrast was evaluated as $\beta$=1/M, where M was determined by fitting Eq. 7.3 for P(K=2) photon hits over the 50 independent diffraction patterns. The error bars are defined to be one standard deviation from the best fit. After evaluating the contrast $\beta$ at all time delays in Fig. 7.2(b), we see the contrast drop from approximately 1 to $\frac{1}{2}$ for the colinear case but is approximately $\frac{1}{2}$ at all time delays for the misaligned case. In other words, a 60 µrad angular mismatch is sufficient to completely destroy the contrast in a double probe XSVS experiment.

In principle, since an angular misalignment shifts the speckle pattern along the detector, the original speckles with 2 or 3 photon hits produced from the two pulses effectively split between neighboring pixels along the detector. Therefore, it should be possible to partially recover the contrast lost by binning the detector images along the direction of misalignment, i.e. summing together the photon counts of N neighboring pixels along the x-direction. By binning, some information about the speckle pattern is lost because now we consider only the total signal within a bin, which might include a few speckles. At first glance, this contradicts the well-established rule stating the optimal setup for an XPCS experiment corresponds to one speckle per pixel. However, for extremely low photon flux, the probability that several photons belonging to different speckles fall in the same bin is negligible. Moreover, our simulations show that the increased photon count per bin outweighs the loss of some resolution on the detector, which is already spoiled by
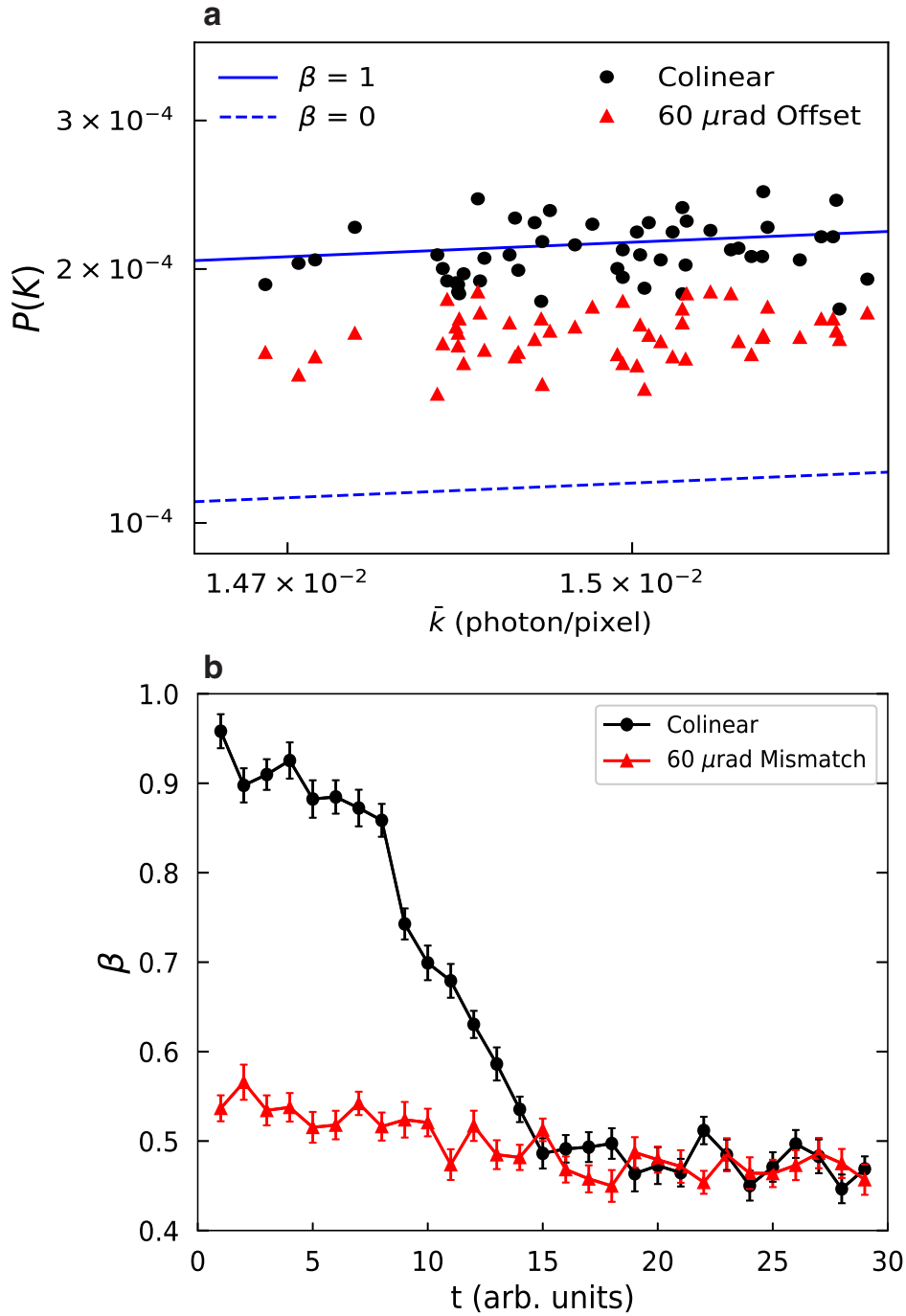
**Figure 7.2**: **(a)** The distribution of K=2 photon hits on a 1024 x 1024 detector in a static system for 50 independent phasor fields for the cases (i) two pulses are colinear and overlapping (ii) the two pulses are overlapping, but misaligned by 60 $\mu$rad. The solid blue line marks a contrast of $\beta = 1$ and the dotted blue line marks a contrast of $\beta = 0$. **(b)** The change of contrast for a dynamical system for the (i) and (ii) cases from fitting the P(K=2) case in Eq. 7.3.

the angular mismatch.

In Fig. 7.3(a), we directly show that by binning the data, the contrast can be partially recovered to the point where the decay is significant above the error bars. Since our speckle size is approximately 2 pixels, we see that a bin size of 2 pixels does not drastically change the contrast trend, but the decay is evident starting at N=4 pixel bin sizes. The contrast trend for the misaligned case also approaches the one for the colinear case with increasing bin size. Since the colinear pulses accurately describe the underlying dynamics, we can consider the bin size of 10 pixels to be the optimal binning as the contrast decay of the misaligned case most resembles the colinear one. However, by binning the data, we are also adding more speckle degrees of freedom within a bin, i.e. effectively increasing M, and thus inherently lowering the range of the theoretical maximum and minimum contrast. Therefore, while the contrast trends of the two cases do approach each other monotonically with bin size, the absolute change in contrast between time zero and long-time delays grows smaller as well. In Fig. 7.3(b), the characteristic timescale extracted from fitting the contrast decay with a stretched exponential function is shown for various bin sizes for both the colinear and misaligned cases. It is evident that the error bars grow smaller with bin size, and the fits to the misaligned case approach that of the colinear case after N = 2 bin size.

In Fig. 7.4(a,b), the absolute change in contrast between time zero and long-time delays for various angular misalignments from 0 to 90 µrad and for various bin sizes up to N=10 pixels calculated from P(K=2) and P(K=3) fits are shown. These values were calculated after averaging the first and last three time delays (t=0, 1, 2 and t=27, 28, 29) as the starting and ending contrast values. At low angular mismatches, the offset in the second probe is not large enough to split the speckles across the detector and thus, binning does not improve the resolution in the contrast difference. However, at higher values of angular mismatch, it is clear the maximum drop of contrast during the time-series
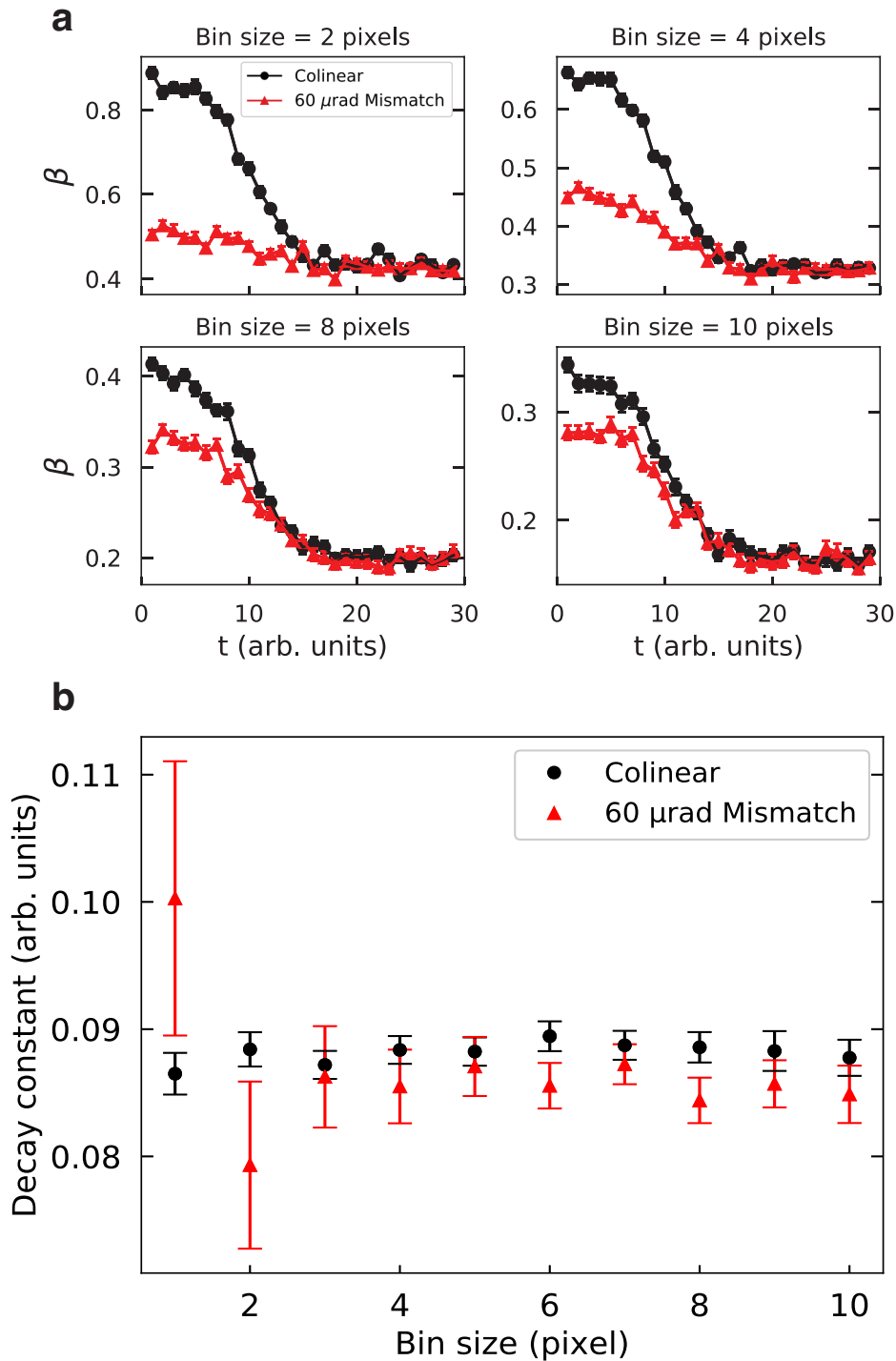
**Figure 7.3**: **(a)** The decay of contrast from fits to the negative binomial distribution for P(K=2) after binning detector images along the direction of the angular misalignment for various bin sizes. The range of $\beta$ grows smaller with increasing bin sizes since there are more speckle degrees of freedom, but the 60 µrad and colinear contrast profiles approach each other as well. **(b)** The characteristic decay time constant extracted from fitting a stretched exponential function to the change in contrast for various bin sizes in both the colinear and angular mismatch cases.

is achieved for a bin size exceeding the speckle size. In Fig. 7.4(c), we show that the optimal bin size in terms of contrast difference varies depending on the angular mismatch angle. For all cases where binning recovers the decay of contrast outside the error bars, the dynamic timescale can be accurately extracted from an exponential fit.

The effects of binning can also be achieved by using a detector with larger pixel sizes. However, bins have a rectangular shape elongated in the direction of angular mismatch. Binning in the orthogonal direction would only decrease the contrast value and not correct for the angular mismatch. Moreover, the optimal binning N is determined by the speckle size and the value of angular mismatch $\Delta\theta$, which can change from one experiment to another even at the same beamline. Therefore, collecting the data using existing detectors with small pixels and performing the binning at the data analysis stage can be advantageous at current split-and-delay setups.

## 7.4.2  Imperfect Overlap

The effect on contrast for imperfectly overlapping Gaussian probes was also investigated without taking into account the angular misalignment. The two probes with a FWHM of 235 pixels originally centered on the 1024 x 1024 phasor field were displaced so that the centers of the Gaussian probes were separated in increments of 20 pixels along the x-direction. We define a fractional offset as the ratio of the probes' displacement to the FWHM of the probes. Since the pulses have a Gaussian profile, a more accurate representation is a weighted overlap between the two that can be calculated from a 2D autocorrelation of the Gaussian pulses centered at $(x_1, y_1)$ and $(x_2, y_2)$, as defined in Eq. 7.8:

$$p(x_2 - x_1, y_2 - y_1) = \frac{\iint G_1(x - x_1, y - y_1)G_2(x - x_2, y - y_2)dxdy}{\iint G_1(x - x_1, y - y_1)dxdy \iint G_2(x - x_2, y - y_2)dxdy}, \tag{7.8}$$
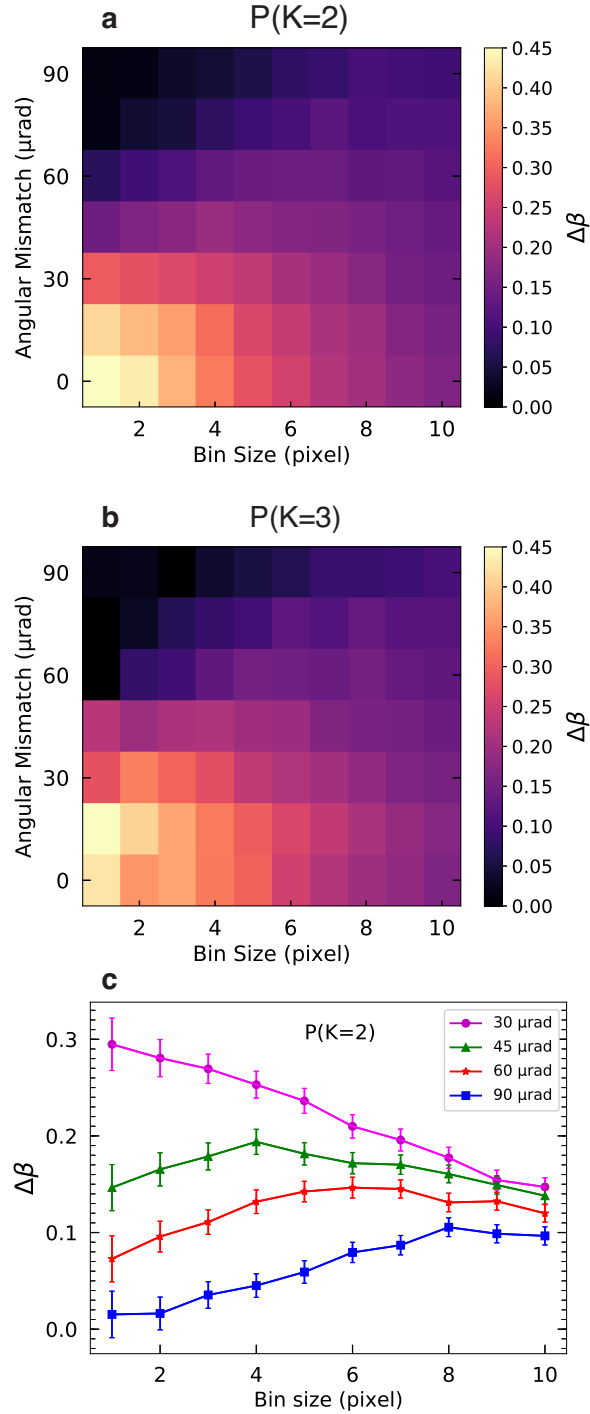
**Figure 7.4**: The decay of contrast for various bin sizes and angular mismatch angles from fits to the negative binomial distribution for **(a)** P(K=2) and **(b)** P(K=3) cases. **(c)** The contrast difference for various bin sizes and select angular mismatches to show optimal bin sizes. The contrast difference is calculated from averaging the contrast of the first three time steps (t=0,1,2) and averaging the contrast of the last three time steps (t=27,28,29).

where $G_1(x,y)$ and $G_2(x,y)$ are intensity profiles of the two x-ray pulses.

The overlap percentages as a function of fractional offset for Gaussian profiles are shown in Fig. 7.5(a) along with the change in contrast. We see that even at a fractional offset of 50%, there is still a contrast difference of 0.2 that is sufficient to extract dynamic timescales in a system. This is not surprising since the distribution in intensity for a fully coherent Gaussian beam allows for a large offset as seen by the weighted overlap. In Fig. 7.5(b), we show that binning the detector along the direction of displacement decreases the contrast difference for all offsets, as expected. Therefore, binning of the data cannot improve the contrast value, suppressed by the partial overlap. However, the decrease in contrast is not dramatic, especially for Gaussian beams.

To demonstrate the possibility of binning the data where both the angular mismatch and imperfect spatial overlap are present, we performed simulations with both effects. The results shown in Fig. 7.6 indicate that a sufficient decay of contrast can be obtained for a wide range of parameters, namely, for $\Delta\theta < 90$ µrad and the fractional offset less than 0.4.

## 7.5   Conclusion

The parameters of our simulation are set to mimic a realistic double probe XSVS experiment, but in general, the experimental should be set up so the speckle size is at least one pixel on the detector. This can be achieved by varying the sample-to-detector distance or the beam spot size, with the latter being a variable in our simulation. A larger beam (5-10 µm) will produce speckles smaller than the detector pixels. Indeed this will make the system more robust to the angular mismatch, but will also reduce the initial contrast and open the possibility of making different speckles indistinguishable within a pixel. Using a larger beam is not equivalent to binning, since we propose to bin along the direction of angular mismatch (for example $q_x$), and changing the beam size will influence the speckle
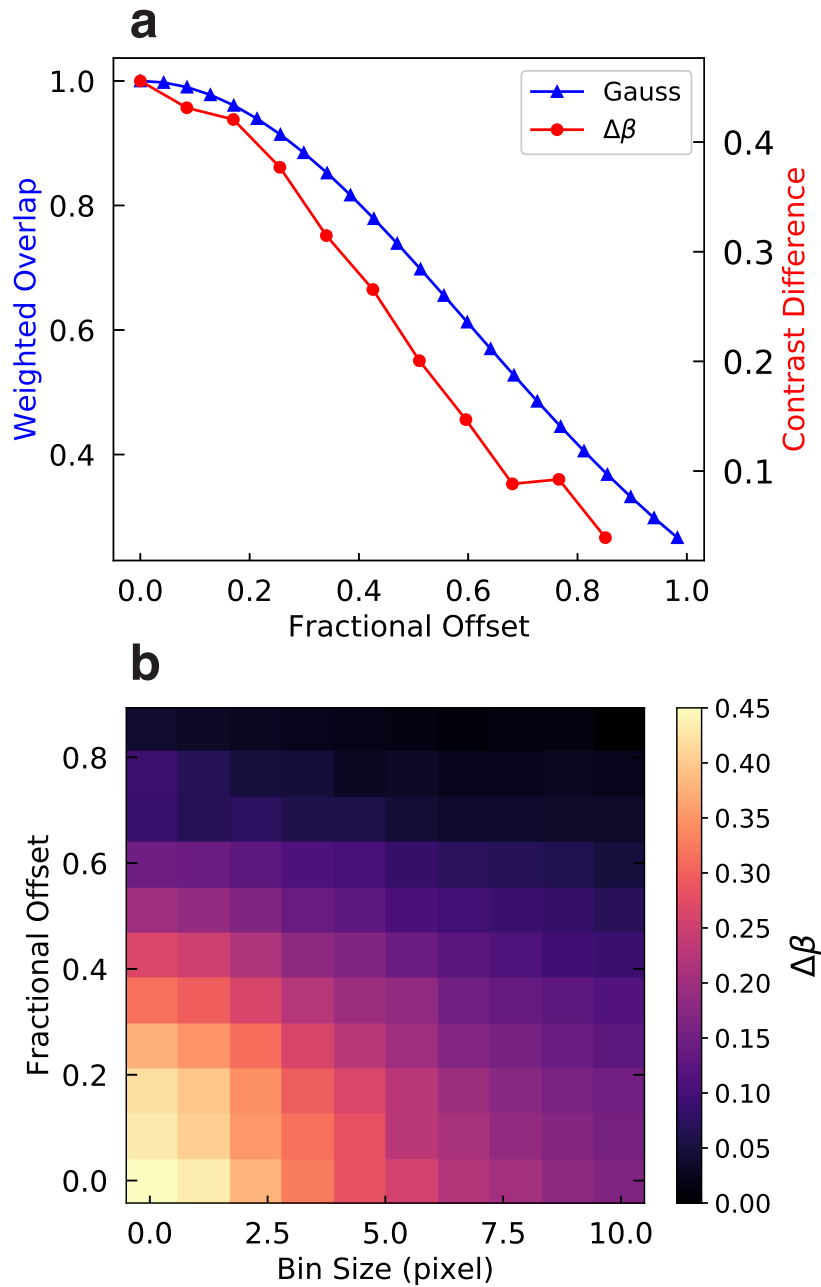
**Figure 7.5**: **(a)** The fractional offset is defined as the ratio of the displacement of the two pulses to the FWHM of the pulses. The overlap percentages corresponding to circular and Gaussian profiles and the contrast difference are shown. **(b)** Effect of binning the detector along the direction of pulse displacement for various bin sizes and fractional offsets.
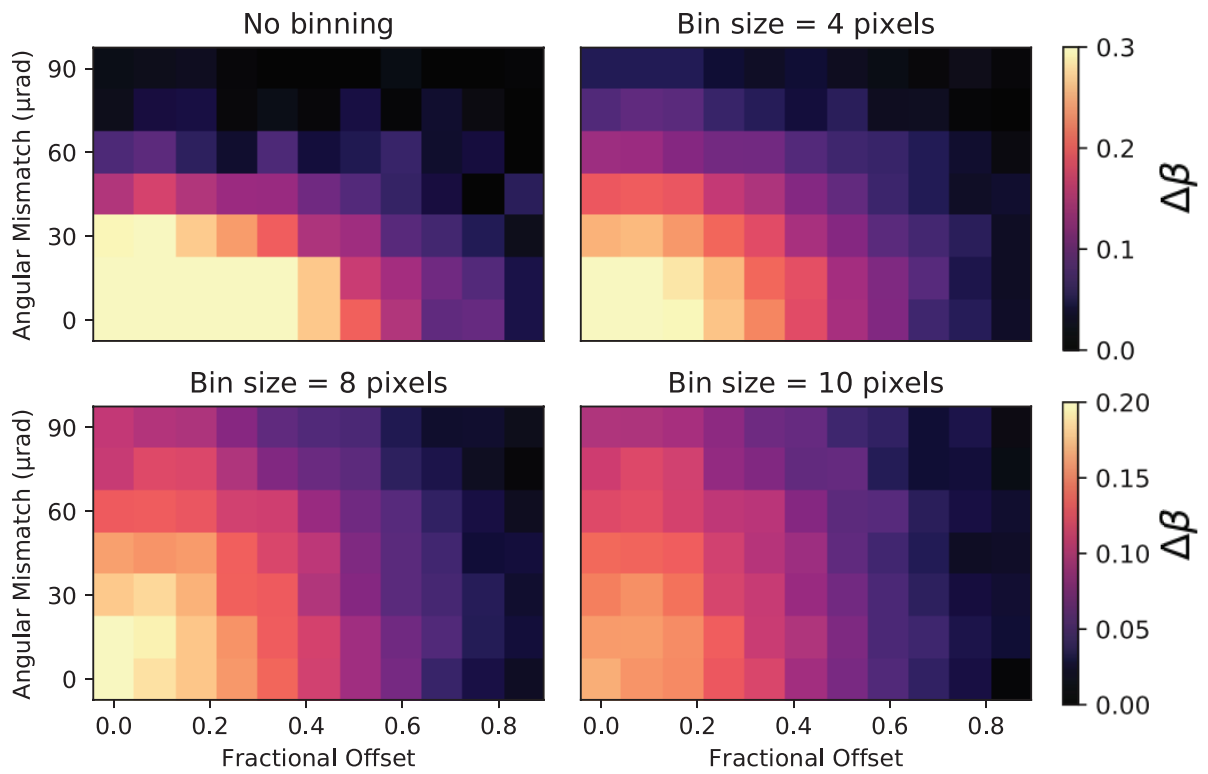
**Figure 7.6**: The effects of binning on the contrast difference is shown for various bin sizes when an angular mismatch and nonperfect overlap exists.

size in both directions ($q_x$ and $q_y$). Our simulations show that binning in the direction perpendicular to the angular mismatch doesn't help to eliminate the effect of the angular mismatch on the speckle contrast. Therefore, using a smaller beam together with binning along one direction is more efficient than using larger beam (which is equivalent to binning along two directions).

Our simulations of a 2D phasor field is representative of surface scattering from a sample in reflection geometry or a thin sample in transmission geometry that is typical for systems of interest in an XSVS experiment [94]. Through numerical simulations, we show that a double probe XSVS experiment can endure a large offset in the overlap between the two pulses, but a small angular misalignment can completely destroy the contrast difference necessary to measure dynamics. Depending on the magnitude of the overlap and angular misalignment, a proper binning of the detector along the direction of angular misalignment can partially recover the contrast. Recently, another approach has been proposed to compensate for the shift of the speckle pattern by evaluating the autocorrelation function [105]. In principle, both techniques yield similar results in partially recovering the original contrast, and should act as complementary tools to verify the results in a double probe XSVS experiment. In our case, in addition to the angular mismatch, we simulated a dynamic speckle pattern with a predefined correlation function in the low-photon count regime. By successfully extracting the time constant from fitting a stretched exponential to the decay of contrast in the binned data, we show that this analysis tool is effective in addressing a double probe XSVS experiment where an angular misalignment and partial overlap exists.

## 7.6    Acknowledgements

# Appendix A

# Analysis of g$_2$(q,t)

The center of the speckle pattern was determined from fitting a 2D Gaussian function to the initial image taken for each temperature. 7 circular regions of interest (ROIs) about the center of the pattern extending over a $\Delta$Q of 5 x $10^{-3}$ Å$^{-1}$ were chosen for each temperature, and the g$_2$(q,t) was calculated separately for each ROI. After fitting the g$_2$(q,t) for each ROI with Eq. (2), no statistically significant difference $\tau$ and $\beta$ suggests there is no q-dependence in the dynamics from the orbitally-ordered domains. This was confirmed for all temperatures. Since there is no q-dependence, the error bars for the ISF were calculated from the ROIs.

To remove artifacts in the speckle pattern fluctuation due to temperature equilibration, the first 30-75 minutes of each scan were not used to calculate the g$_2$(t). Determining the cutoff for each temperature measurement was based on 1) the kymographs where the fluctuations in the speckles due to the sample settling was evident and 2) g$_2$(t) calculations on sliding intervals of time. For example, for a 4-hour scan, a 2-hour interval was used to calculate the g$_2$(t) where the starting point was incremented by 10 minutes. Since no aging is expected in the system, the g$_2$(t) should be the same regardless of which time interval within the measurement is taken. We estimated the point in time when the sample settled

based on the difference between $g_2(t)$ calculations that were separated by a 10-minute difference in starting points.

# Bibliography

[1] T. Li, A. Patz, L. Mouchliadis, J. Yan, T. Lograsso, I. Perakis, and J. Wang, "Femtosecond switching of magnetism via strongly correlated spin-charge quantum excitations," *Nature*, vol. 496, 2013.

[2] Y. Tokura, M. Kawasaki, and N. Nagaosa, "Emergent functions of quantum materials," *Nature Physics*, vol. 13, no. 11, pp. 1056–1068, 2017.

[3] W. Röntgen, "On a new kind of rays," *Nature*, vol. 53, 1896.

[4] W. Bragg, R. James, and C. Bosanquet, "Xxix. the intensity of reflexion of x-rays by rock-salt," *The London, Edinburgh, and Dublin Philosophical Magazine and Journal of Science*, vol. 41, no. 243, pp. 309–337, 1921.

[5] J. Watson and F. Crick, "Molecular structure of nucleic acids: A structure for deoxyribose nucleic acid," *Nature*, vol. 171, 1953.

[6] E. Dagotto, "Complexity in strongly correlated electronic systems," *Science*, vol. 309, 2005.

[7] S. Kivelson and S. Kivelson, "Defining emergence in physics," *Nature Physics*, vol. 1, no. 1, p. 16024, 2016.

[8] Y. Cao, V. Fatermi, S. Fang, K. Watanabe, T. Taniguichi, E. Kaxiras, and P. Jarillo-Herrero, "Unconventional superconductivity in magic-angle graphene superlattices," *Nature*, vol. 556, pp. 43–50, 2018.

[9] P. Monthoux, A. V. Balatsky, and D. Pines, "Toward a theory of high-temperature superconductivity in the antiferromagnetically correlated cuprate oxides," *Phys. Rev. Lett.*, vol. 67, pp. 3448–3451, 1991.

[10] D.-H. Lee, "Routes to high-temperature superconductivity: A lesson from fese/srtio3," *Annual Review of Condensed Matter Physics*, vol. 9, no. 1, pp. 261–282, 2018.

[11] J. Grollier, S. Guha, H. Ohno, and I. K. Schuller, "Preface to special topic: New physics and materials for neuromorphic computation," *Journal of Applied Physics*, vol. 124, no. 15, p. 151801, 2018.

[12] R. Jansen, "Silicon spintronics," *Nature Materials*, vol. 11, no. 5, pp. 400–408, 2012.

[13] C. Chappert, A. Fert, and F. Van Dau, "The emergence of spin electronics in data storage," *Nature Materials*, vol. 6, no. 11, pp. 400–408, 2007.

[14] C. W. M. Castleton and M. Altarelli, "Orbital ordering in the manganites: Resonant x-ray scattering predictions at the manganese $L_{ii}$ and $L_{iii}$ edges," *Phys. Rev. B*, vol. 62, pp. 1033–1038, 2000.

[15] J. Als-Nielsen, *X-rays and their interaction with matter*. John Wiley & Sons, Ltd, 2011.

[16] B. Cullity and S. Stock, *Elements of X-ray Diffraction*. Prentice Hall, 2001.

[17] N. Lei, T. Devolder, G. Agnus, P. Aubert, L. Daniel, J.-V. Kim, W. Zhao, T. Trypiniotis, R. Cowburn, C. Chappert, D. Ravelosona, and P. Lecoeur, "Strain-controlled magnetic domain wall propagation in hybrid piezoelectric/ferromagnetic structures," *Nature Communications*, vol. 4, 2013.

[18] W. Goldburg, "Dynamic light scattering," *American Journal of Physics*, vol. 67, 1999.

[19] R. Pecora, "Dynamic light sattering measurement of nanometer particles in liquids," *Journal of Nanoparticle Research*, vol. 2, pp. 123–131, 2000.

[20] Z. Evenson, B. Ruta, S. Hechler, M. Stolpe, E. Pineda, I. Gallino, and R. Busch, "X-ray photon correlation spectroscopy reveals intermittent aging dynamics in a metallic glass," *Physical Review Letters*, vol. 115, 2015.

[21] O. Shpyrko, E. Isaacs, J. Logan, Y. Feng, G. Aeppli, R. Jaramillo, H. Kim, T. Rosenbaum, P. Zschack, M. Sprung, S. Narayanan, and A. Sandy, "Direct measurement of antiferromagnetic domain fluctuations," *Nature*, vol. 447, 2007.

[22] B. Ruta, Y. Chushkin, G. Monaco, L. Cipelletti, E. Pineda, P. Bruna, V. M. Giordano, and M. Gonzalez-Silveira, "Atomic-scale relaxation dynamics and aging in a metallic glass probed by x-ray photon correlation spectroscopy," *Phys. Rev. Lett.*, vol. 109, p. 165701, Oct 2012.

[23] J. Fink, E. Schierle, E. Weschke, and J. Geck, "Resonant elastic soft x-ray scattering," *Reports on Progress in Physics*, vol. 76, no. 5, p. 056502, 2013.

[24] B. Y. Pan, H. Jang, J.-S. Lee, R. Sutarto, F. He, J. F. Zeng, Y. Liu, X. W. Zhang, Y. Feng, Y. Q. Hao, J. Zhao, H. C. Xu, Z. H. Chen, J. P. Hu, and D. L. Feng, "Intertwined spin and orbital density waves in mnp uncovered by resonant soft x-ray scattering," *Phys. Rev. X*, vol. 9, p. 021055, 2019.

[25] D. Gibbs, D. R. Harshman, E. D. Isaacs, D. B. McWhan, D. Mills, and C. Vettier, "Polarization and resonance properties of magnetic x-ray scattering in holmium," *Phys. Rev. Lett.*, vol. 61, pp. 1241–1244, 1988.

[26] M. Holt, R. Harder, R. Winarski, and V. Rose, "Nanoscale hard x-ray microscopy methods for materials studies," *Annual Review of Materials Research*, vol. 43, no. 1, pp. 183–211, 2013.

[27] J. Kim, C. Ko, A. Frenzel, S. Ramanathan, and J. E. Hoffman, "Nanoscale imaging and control of resistance switching in vo2 at room temperature," *Applied Physics Letters*, vol. 96, no. 21, p. 213106, 2010.

[28] R. P. Winarski, M. V. Holt, V. Rose, P. Fuesz, D. Carbaugh, C. Benson, D. Shu, D. Kline, G. B. Stephenson, I. McNulty, and J. Maser, "A hard x-ray nanoprobe beamline for nanoscale microscopy," *Journal of Synchrotron Radiation*, vol. 19, no. 6, pp. 1056–1060, 2012.

[29] S. Hruszkewycz, M. Holt, J. Maser, C. Murray, M. Highland, C. Folkman, and P. Fuoss, "Coherent bragg nanodiffraction at the x-ray nanoprobe beamline," *Phil. Trans. R. Soc. A.*, vol. 372, p. 20130118, 2014.

[30] M. Imada, A. Fujimori, and Y. Tokura, "Metal-insulator transitions," *Reviews of Modern Physics*, vol. 70, 1998.

[31] Y. Yanase, T. Jujo, T. Nomura, H. Ikeda, T. Hotta, and K. Yamada, "Theory of superconductivity in strongly correlated electron systems," *Physics Reports*, vol. 387, 2003.

[32] E. Verwey, P. Haayman, and F. Roemijn, "Physical properties and cation arrangement of oxides with spinel structures ii. electronic conductivity," *The Journal of Chemical Physics*, vol. 15, 1947.

[33] M. Coey, "Condensed-matter physics: charge-ordering in oxides," *Nature*, vol. 430, 2004.

[34] M. Iizumi, T. Koetzle, G. Shirane, S. Chikazumi, M. Matsui, and T. S., "Structure of magnetite (fe3o4) below the verwey transition temperature," *Acta Crystallographica Section B*, vol. 38, 1984.

[35] E. Verwey, "Electronic conduction of magnetite (fe3o4) and its transition point at low temperatures," *Nature*, vol. 144, 1939.

[36] M. Senn, J. Wright, and J. Attfield, "Charge order and three-site distortions in the verwey structure of magnetite," *Nature*, vol. 481, 2011.

[37] J. Wright, J. Attfield, and P. Radaelli, "Charge orderd structure of magnetite fe3o4 below the verwey transition," *Physical Review B*, vol. 66, 2002.

[38] D. Khomskii and M. Mostovoy, "Orbital ordering and frustrations," *Journal of Physics A: Mathematical and General*, vol. 36, 2003.

[39] K. Kugel and D. Khomskii, "Crystal structure and magnetic properties of substances with orbital degeneracy," *Soviet Journal of Experimental and Theoretical Physics*, vol. 37, 1973.

[40] K. Kugel and D. Khomskii, "The jahn-teller effect and magnetism: Transition metal compounds," *Soviet Physics - Uspekhi*, vol. 25, 1982.

[41] G. Subias, V. Cuartero, J. Garcia, J. Herrero-Martin, J. Blasco, M. Concepcion Sanchez, and F. Yakhou, "Soft resonant x-ray scattering in highly stoichiometric magnetite," *Journal of Physics: Conference Series*, vol. 190, 2009.

[42] J. Schlappa, C. SchuBler-Langeheine, C. Chang, H. Ott, A. Tanaka, Z. Hu, M. Haverkort, E. Schierle, E. Weschke, G. Kaindl, and L. Tjeng, "Direct observation of t2g orbital ordering in magnetite," *Physical Review Letters*, vol. 100, 2008.

[43] D. Huang, H.-J. Lin, J. Okamoto, K. Chao, H.-T. Jeng, G. Guo, C.-H. Hsu, C.-M. Huang, D. Ling, W. Wu, C. Yang, and C. Chen, "Charge-orbital ordering and verwey transition in magnetite measured by resonant soft x-ray scattering," *Physical Review Letters*, vol. 96, 2006.

[44] M. Hepting, *Introduction: Transition Metal Oxides and Their Heterostructures.* Springer, 2017.

[45] S. Wilkins, S. D. Matteo, T. Beale, Y. Joly, C. Mazzoli, P. Hatton, P. Bencok, F. Yakhou, and V. Brabers, "Critical reexamination of resonant soft x-ray bragg forbidden reflections in magnetite," *Physical Review B*, vol. 79, 2009.

[46] I. Leonov, A. Yaresko, V. Antonov, M. Korotin, and V. Anisimov, "Charge and orbital order in fe3o4," *Physical Review Letters*, vol. 93, 2004.

[47] J. Suntivich, W. T. Hong, Y.-L. Lee, J. M. Rondinelli, W. Yang, J. B. Goodenough, B. Dabrowski, J. W. Freeland, and Y. Shao-Horn, "Estimating hybridization of transition metal and oxygen states in perovskites from o k-edge x-ray absorption spectroscopy," *Journal of Physical Chemistry C*, vol. 118, 2014.

[48] W. Eerenstein, T. Palstra, T. Hibma, and S. Celotto, "Origin of the increased resistivity in epitaxial fe3o4 films," *Physical Review B*, vol. 66, 2002.

[49] L. Cipelletti, L. Ramos, S. Manley, E. Pitard, D. Weitz, E. Pashkovski, and M. Johansson, "Universal non-diffusive slow dynamics in aging soft matter," *Faraday Discussions*, vol. 123, 2003.

[50] R. Bandyopadhyay, D. Liang, H. Yardimci, D. Sessoms, M. Borthwick, S. Mochrie, J. Harden, and R. Leheny, "Evolution of particle-scale dynamics in an aging clay suspension," *Physical Review Letters*, vol. 93, 2004.

[51] S. Chen, H. Guo, K. Seu, K. Dumesnil, S. Roy, and S. Sinha, "Jamming behavior of domains in a spiral antiferromagnetic system," *Physical Review Letters*, vol. 110, 2013.

[52] J. Lorenzo, C. Mazzoli, N. Jaouen, C. Detlefs, D. Mannix, S. Grenier, Y. Joly, and C. Marin, "Charge and orbital correlations at and above the verwey phase transition in magnetite," *Physical Review Letters*, vol. 101, 2008.

[53] K. Thomas, J. Hill, S. Grenier, Y. Kim, P. Abbamonte, L. Venema, A. Rusydi, Y. Tomioka, Y. Tokura, D. McMorrow, G. Sawatzky, and M. van Veenendaal, "Soft x-ray resonant diffraction study of magnetic and orbital correlations in a manganite near half doping," *Physical Review Letters*, vol. 92, 2004.

[54] J. Turner, K. Thomas, J. Hill, M. Pfelfer, K. Chesnel, Y. Tomioka, Y. Tokura, and D. Kevan, "Orbital domain dynamics in a doped manganite," *New Journal of Physics*, vol. 10, 2008.

[55] J. Hill, C. Nelson, M. Zimmermann, Y. Kim, D. Gibbs, D. Casa, B. Keimer, Y. Murakami, C. Venkataraman, T. Gog, Y. Tomioka, Y. Tokura, V. Kiryukhin, T. Koo, and S. Cheong, "Orbital correlations in doped manganites," *Applied Physics A: Materials Science and Processing*, vol. 73, 2001.

[56] Y. Tokura and N. Nagaosa, "Orbital physics in transition-metal oxides," *Science*, vol. 288, 2000.

[57] G. Khaliullin, P. Horsch, and A. Olés, "Spin order due to orbital fluctuations: Cubic vanadates," *Physical Review Letters*, vol. 86, 2001.

[58] J. J. Wen, H. Huang, S. J. Lee, H. Jang, J. Knight, Y. S. Lee, M. Fujita, K. M. Suzuki, S. Asano, S. A. Kivelson, C. C. Kao, and J. S. Lee, "Observation of two types of charge-density-wave orders in superconducting la2-xsrxcuo4," *Nature Communications*, vol. 10, 2019.

[59] P. Babkevich, P. G. Freeman, M. Enderle, D. Prabhakaran, and A. T. Boothroyd, "Direct evidence for charge stripes in a layered cobalt oxide," *Nature Communications*, vol. 7, 2016.

[60] M. Kang, J. Pelliciari, A. Frano, N. Breznay, E. Schierle, E. Weschke, R. Sutarto, F. He, P. Shafer, E. Arenholz, M. Chen, K. Zhang, A. Ruiz, Z. Hao, S. Lewin, J. Analytis, Y. Krockenberger, H. Yamamoto, T. Das, and R. Comin, "Evolution of charge order topology across a magnetic phase transition in cuprate superconductors," *Nature Physics*, vol. 15, 2019.

[61] E. Fawcett, "Spin-density-wave antiferromagnetism in chromium," *Rev. Mod. Phys.*, vol. 60, pp. 209–283, 1988.

[62] L. M. Corliss, J. M. Hastings, and R. J. Weiss, "Antiphase antiferromagnetic structure of chromium," *Phys. Rev. Lett.*, vol. 3, 1959.

[63] A. Singer, M. J. Marsh, S. H. Dietze, V. Uhlíř, Y. Li, D. A. Walko, E. M. Dufresne, G. Srajer, M. P. Cosgriff, P. G. Evans, E. E. Fullerton, and O. G. Shpyrko, "Condensation of collective charge ordering in chromium," *Phys. Rev. B*, vol. 91, p. 115134, 2015.

[64] A. Singer, S. Patel, V. Uhlir, R. Kukreja, A. Ulvestad, E. Dufresne, A. Sandy, E. Fullerton, and O. Shpyrko, "Phase coexistence and pinning of charge density waves by interfaces in chromium," *Physical Review B*, vol. 94, 2016.

[65] A. Singer, S. K. K. Patel, R. Kukreja, V. Uhlíř, J. Wingert, S. Festersen, D. Zhu, J. M. Glownia, H. T. Lemke, S. Nelson, M. Kozina, K. Rossnagel, M. Bauer, B. M. Murphy, O. M. Magnussen, E. E. Fullerton, and O. G. Shpyrko, "Photoinduced enhancement of the charge density wave amplitude," *Phys. Rev. Lett.*, vol. 117, p. 056401, 2016.

[66] J. Wingert, A. Singer, S. K. K. Patel, R. Kukreja, M. J. Verstraete, A. H. Romero, V. Uhlíř, S. Festersen, D. Zhu, J. M. Glownia, H. T. Lemke, S. Nelson, M. Kozina, K. Rossnagel, B. M. Murphy, O. M. Magnussen, E. E. Fullerton, and O. G. Shpyrko, "Direct time-domain determination of electron-phonon coupling strengths in chromium," *Phys. Rev. B*, vol. 102, p. 041101, 2020.

[67] H. Zabel, "Magnetism of chromium at surfaces, at interfaces and in thin films," *Journal of Physics: Condensed Matter*, vol. 11, no. 48, pp. 9303–9346, 1999.

[68] H. Dery, P. Dalal, L. Cywinski, and L. Sham, "Spin-based logic in semiconductors for reconfigurable large-scale circuits," *Nature*, vol. 447, 2007.

[69] L. W. Martin, S. P. Crane, Y.-H. Chu, M. B. Holcomb, M. Gajek, M. Huijben, C.-H. Yang, N. Balke, and R. Ramesh, "Multiferroics and magnetoelectrics: thin films and nanostructures," *Journal of Physics: Condensed Matter*, vol. 20, no. 43, 2008.

[70] W. Eerenstein, N. Mathur, and J. Scott, "Multiferroics and magnetoelectric materials," *Nature*, vol. 442, no. 7104, 2006.

[71] J. G. van Bennekom, L. Winnubst, W. Nijdam, M. Wessling, and R. G. Lammertink", "A novel method for the fabrication of freestanding pzt features on substrates," *Journal of the European Ceramic Society*, vol. 29, no. 15, 2009.

[72] S. R. Bakaul, J. Kim, S. Hong, M. J. Cherukara, T. Zhou, L. Stan, C. R. Serrao, S. Salahuddin, A. K. Petford-Long, D. D. Fong, and M. V. Holt, "Ferroelectric domain wall motion in freestanding single-crystal complex oxide thin film," *Advanced Materials*, vol. 32, no. 4, p. 1907036, 2020.

[73] D. M. Marincel, S. Jesse, A. Belianinov, M. B. Okatan, S. V. Kalinin, T. N. Jackson, C. A. Randall, and S. Trolier-McKinstry, "A-site stoichiometry and piezoelectric response in thin film pbzr1 xtixo3," *Journal of Applied Physics*, vol. 117, no. 20, p. 204104, 2015.

[74] Y. Takamura, R. V. Chopdekar, A. Scholl, A. Doran, J. A. Liddle, B. Harteneck, and Y. Suzuki, "Tuning magnetic domain structure in nanoscale la0.7sr0.3mno3 islands," *Nano Letters*, vol. 6, no. 6, pp. 1287–1291, 2006.

[75] E. Folven, Y. Takamura, and J. Grepstad, "X-peem study of antiferromagnetic domain patterns in lafeo3 thin films and embedded nanostructures," *Journal of Electron Spectroscopy and Related Phenomena*, vol. 185, no. 10, pp. 381 – 388, 2012.

[76] T. Tsurumi, Y. Kumano, N. Ohashi, T. Takenaka, and O. Fukunaga, "90°domain reorientation and electric-field-induced strain of tetragonal lead zirconate titanate ceramics," *Japanese Journal of Applied Physics*, vol. 36, 1997.

[77] I. Kanno, H. Kotera, K. Wasa, T. Matsunaga, T. Kamada, and R. Takayama, "Crystallographic characterization of epitaxial pb(zr,ti)o3 films with different zr/ti ratio grown by radio-frequency-magnetron sputtering," *Journal of Applied Physics*, vol. 93, no. 7, pp. 4091–4096, 2003.

[78] T. W. Cornelius, C. Mocuta, S. Escoubas, A. Merabet, M. Texier, E. C. Lima, E. B. Araujo, A. L. Kholkin, and O. Thomas, "Piezoelectric response and electrical properties of pb(zr1-xtix)o3 thin films: The role of imprint and composition," *Journal of Applied Physics*, vol. 122, no. 16, p. 164104, 2017.

[79] R. dos Reis, H. Yang, C. Ophus, P. Ercius, G. Bizarri, D. Perrodin, T. Shalapska, E. Bourret, J. Ciston, and U. Dahmen, "Determination of the structural phase and octahedral rotation angle in halide perovskites," *Applied Physics Letters*, vol. 112, no. 7, p. 071901, 2018.

[80] K. A. Schönau, L. A. Schmitt, M. Knapp, H. Fuess, R.-A. Eichel, H. Kungl, and M. J. Hoffmann, "Nanodomain structure of $Pb[zr_{1-x}ti_x]o_3$ at its morphotropic phase boundary: Investigations from local to average structure," *Phys. Rev. B*, vol. 75, p. 184117, 2007.

[81] B. Noheda, J. A. Gonzalo, L. E. Cross, R. Guo, S.-E. Park, D. E. Cox, and G. Shirane, "Tetragonal-to-monoclinic phase transition in a ferroelectric perovskite: The structure of $pbzr_{0.52}ti_{0.48}o_3$," *Phys. Rev. B*, vol. 61, pp. 8687–8695, 2000.

[82] M. Hinterstein, J. Rouquette, J. Haines, P. Papet, M. Knapp, J. Glaum, and H. Fuess, "Structural description of the macroscopic piezo- and ferroelectric properties of lead zirconate titanate," *Phys. Rev. Lett.*, vol. 107, p. 077602, 2011.

[83] J. Martín, J. Nogués, K. Liu, J. Vicent, and I. Schuller, "Ordered magnetic nanostructures: fabrication and properties," *Journal of Magnetism and Magnetic Materials*, vol. 256, no. 1, pp. 449 – 501, 2003.

[84] C. Ross, "Patterned magnetic recording media," *Annual Review of Materials Research*, vol. 31, no. 1, pp. 203–235, 2001.

[85] S. S. P. Parkin, M. Hayashi, and L. Thomas, "Magnetic domain-wall racetrack memory," *Science*, vol. 320, no. 5873, pp. 190–194, 2008.

[86] R. Hertel, "Magnetic nanostructures: vortex states à la carte," *Nature nanotechnology*, vol. 8, no. 5, p. 318—320, 2013.

[87] B. Van Waeyenberge, A. Puzic, H. Stoll, K. W. Chou, T. Tyliszczak, R. Hertel, M. Fähnle, H. Brückl, K. Rott, G. Reiss, I. Neudecker, D. Weiss, C. H. Back, and G. Schütz, "Magnetic vortex core reversal by excitation with short bursts of an alternating field," *Nature*, vol. 444, no. 7118, pp. 461–464, 2006.

[88] A. Ramirez, "Colossal magnetoresistance," *Journal of Physics: Condensed Matter*, vol. 9, no. 39, pp. 8171–8199, 1997.

[89] M. S. Lee, T. A. Wynn, E. Folven, R. V. Chopdekar, A. Scholl, A. T. Young, S. T. Retterer, J. K. Grepstad, and Y. Takamura, "Tailoring spin textures in complex oxide micromagnets," *ACS Nano*, vol. 20, no. 9, pp. 8545–8551, 2016.

[90] M. V. Holt, S. O. Hruszkewycz, C. E. Murray, J. R. Holt, D. M. Paskiewicz, and P. H. Fuoss, "Strain imaging of nanoscale semiconductor heterostructures with x-ray bragg projection ptychography," *Phys. Rev. Lett.*, vol. 112, p. 165502, 2014.

[91] M. Sutton, S. Mochrie, T. Greytak, S. Nagler, L. Berman, G. Held, and G. Stephenson, "Observation of speckle by diffraction with coherent x-rays," *Nature*, vol. 352, 1991.

[92] A. Fluerasu, M. Sutton, and E. Dufresne, "X-ray intensity fluctuation spectroscopy studies on phase-ordering systems," *Physical Review Letters*, vol. 94, 2005.

[93] O. G. Shpyrko, "X-ray photon correlation spectroscopy," *Journal of Synchrotron Radiation*, vol. 21, no. 5, pp. 1057–1064, 2014.

[94] S. K. Sinha, Z. Jiang, and L. Lurio, "X-ray photon correlation spectroscopy studies of surfaces and thin films," *Advanced Materials*, vol. 26, no. 46, pp. 7764–7785, 2014.

[95] T. Madden, S. Niu, S. Narayanan, A. Sandy, J. Weizeorick, P. Denes, J. Joseph, V. Moeller-Chan, D. Doering, and P. McVittie, "Real-time mpi-based software for processing of xpcs data," *2014 IEEE Nuclear Science Symposium and Medical Imaging Conference, NSS/MIC 2014*, 2016.

[96] C. Ponchut, J. M. Rigal, J. Clément, E. Papillon, A. Homs, and S. Petitdemange, "MAXIPIX, a fast readout photon-counting x-ray area detector for synchrotron applications," *Journal of Instrumentation*, vol. 6, no. 01, pp. C01069–C01069, 2011.

[97] T. Hirano, T. Osaka, Y. Morioka, Y. Sano, Y. Inubushi, T. Togashi, I. Inoue, S. Matsuyama, K. Tono, A. Robert, J. Hastings, K. Yamauchi, and M. Yabashi, "Performance of a hard x-ray split-and-delay optical system with a wavefront division," *Journal of Synchrotron Radiatiation*, vol. 25, pp. 20–25, 2018.

[98] W. Roseker, S. O. Hruszkewycz, F. Lehmkühler, M. Walther, H. Schulte-Schrepping, S. Lee, T. Osaka, L. Strüder, R. Hartmann, M. Sikorski, S. Song, A. Robert, P. H. Fuoss, M. Sutton, G. B. Stephenson, and G. Grübel, "Towards ultrafast dynamics with split-pulse x-ray photon correlation spectroscopy at free electron laser sources," *Nature Communications*, vol. 9, p. 1704, 2018.

[99] W. Roseker, S. Lee, M. Walther, F. Lehmkühler, B. Hankiewicz, R. Rysov, S. Hruszkewycz, B. Stephenson, M. Sutton, P. Fuoss, M. Sikorski, A. Robert, S. Song, and G. Grübel, "Double-pulse speckle contrast correlations with near fourier transform limited free-electron laser light using hard x-ray split-and-delay," *Scientific Reports*, vol. 10, p. 5054, 2020.

[100] R. Rysov, W. Roseker, M. Walther, and G. Grübel, "Compact hard x-ray split-and-delay line for studying ultrafast dynamics at free-electron laser sources," *Journal of Synchrotron Radiation*, vol. 26, no. 4, pp. 1052–1057, 2019.

[101] S. O. Hruszkewycz, M. Sutton, P. H. Fuoss, B. Adams, S. Rosenkranz, K. F. Ludwig, W. Roseker, D. Fritz, M. Cammarata, D. Zhu, S. Lee, H. Lemke, C. Gutt, A. Robert, G. Grübel, and G. B. Stephenson, "High contrast x-ray speckle from atomic-scale order in liquids and glasses," *Physical Review Letters*, vol. 109, p. 185502, 2012.

[102] M. H. Seaberg, B. Holladay, J. C. T. Lee, M. Sikorski, A. H. Reid, S. A. Montoya, G. L. Dakovski, J. D. Koralek, G. Coslovich, S. Moeller, W. F. Schlotter, R. Streubel, S. D. Kevan, P. Fischer, E. E. Fullerton, J. L. Turner, F.-J. Decker, S. K. Sinha, S. Roy, and J. J. Turner, "Nanosecond x-ray photon correlation spectroscopy on magnetic skyrmions," *Physical Review Letters*, vol. 119, p. 067403, 2017.

[103] F. Perakis, G. Camisasca, T. J. Lane, A. Späh, K. Wikfeldt, J. Sellberg, F. Lehmkühler, H. Pathak, K. Kim, K. Amann-Winkel, S. Schreck, S. Song, T. Sato, A. Sikorski, M.and Eilert, H. McQueen, T.and Ogasawara, D. Nordlund, W. Roseker, S. Koralek, J.and Nelson, P. Hart, R. Alonso-Mori, Y. Feng, D. Zhu, A. Robert, G. Grübel, L. Pettersson, and A. Nilsson, "Nanosecond x-ray photon correlation spectroscopy on magnetic skyrmions," *Nature Communications*, vol. 9, p. 1917, 2018.

[104] M. Yabashi, H. Tanaka, K. Tono, and T. Ishikawa, "Status of the sacla facility," *Applied Sciences*, vol. 7, 2017.

[105] Y. Sun, M. Dunne, P. Fuoss, A. Robert, D. Zhu, T. Osaka, and M. Yabashi, M.and Sutton, "Realizing split-pulse x-ray photon correlation spectroscopy to measure ultrafast dynamics in complex matter," *Physical Review Research*, vol. 2, p. 023099, 2020.

[106] L. Li, D. Kwaśniewski, P.and Orsi, L. Wiegart, L. Cristofolini, C. Caronna, and A. Fluerasu, "Photon statistics and speckle visibility spectroscopy with partially coherent x-rays," *Journal of Synchrotron Radiation*, vol. 21, no. 6, pp. 1288–1295, 2014.

[107] J. Goodman, *Speckle Phenomena in Optics: Theory and Applications.* Roberts & Company, 2007.

[108] A. Federico, G. Kaufmann, G. Galizzi, H. Rabal, M. Trivi, and R. Arizaga, "Simulation of dynamic speckle sequences and its application to the analysis of transient processes," *Optics Communications*, vol. 206, pp. 493–499, 2006.